Characterisation Studies of Silicon Photomultipliers for the Detection of Fluorescence Light from Extensive Air Showers

von

Markus Lauscher

Masterarbeit in Physik

vorgelegt der
Fakultät für Mathematik, Informatik und Naturwissenschaften
der
Rheinisch-Westfälischen Technischen Hochschule Aachen

Vorgelegt im Januar 2012

angefertigt am

III. Physikalischen Institut A

Erstgutachter und Betreuer

Prof. Dr. Thomas Hebbeker
III. Physikalisches Institut A
RWTH Aachen

Zweitgutachter

Prof. Dr. Martin Erdmann
III. Physikalisches Institut A
RWTH Aachen

Contents

List of Figures

1. Introduction

For millennia photons of a relatively narrow wavelength range have been mankind's only messengers from the cosmos. With the advance of technology messengers besides visible light have become available, increasing our understanding of the cosmos and also the number of unanswered questions.

One of these messengers are cosmic rays which are highly energetic particles, with energies from the MeV range of up to several 10^{20} eV. These particles constantly bombard the Earth from all directions with the flux steeply falling with energy.

Even though the discovery of cosmic rays now dates back nearly one hundred years to Victor Hess and his famous balloon flights in 1912, they still remain a fascinating research topic. Especially cosmic rays with energies above 10^{18} eV, referred to as ultra-high-energy cosmic rays (UHECRs) still raise many questions. What are the sources, capable of accelerating particles to these energies? What is the acceleration mechanism? What is their composition? Can they tell us something about the position of their sources? Can they tell us something about the structure of the universe, like the structure of galactic and inter-galactic magnetic fields?

To answer these questions precise measurements of the properties of UHECRs are required. As the flux of UHECRs is very low, of the order of one particle per year and square-kilometre and lower, huge ground based detectors are required to study them. These detectors do not observe the primary cosmic ray particles directly, but rather the cascade of particles they initiate in the atmosphere, called extensive air showers.

One powerful technique to study these showers is fluorescence detection. Here telescopes measure the fluorescence light, produced by the nitrogen in the atmosphere which is excited by shower particles. This technique allows a calorimetric measurement of the shower energy and consequently the energy of the primary particle, as well as the reconstruction of the arrival direction and other parameters of interest.

Because the fluorescence light provides only a very weak signal, efficient light-detectors are required for this method. Current experiments, such as the Pierre Auger Observatory use photomultiplier tubes (PMTs) for this purpose.

Silicon photomultipliers (SiPMs) are a relatively new kind of semiconductor light-detectors, promising even higher detection efficiencies than PMTs and possibly offering other advantages in their usage as the light sensitive part of fluorescence detectors.

The goal of this thesis is to characterise the properties of SiPMs which are important for the detection of fluorescence light, most importantly the photon detection efficiency. Besides possible advantages SiPMs also offer some challenges in their usage such as correlated noise and a dependence of the operational behaviour on the temperature. These issues, together with possible solutions are also studied. The achieved results can then be used to assess the advantages and challenges arising from using SiPMs for the detection of fluorescence light from extensive air showers.

This thesis starts with a short introduction to cosmic rays in general in chapter 2, and their study with fluorescence detection in particular in chapter 3. An overview of the working principle of SiPMs, and the parameters of the characterised SiPMs is given in chapter 4.

Chapter 5 serves as the introduction to the measurement chapters. One measurement setup, used in this thesis is described there, together with some basic SiPM measurement results.

A challenge raised by the operation of SiPMs is the rather strong dependence of their operational behaviour on the temperature. A detailed measurement of this dependence and a working solution, compensating this effect, can be found in chapter 6.

An additional challenge presented by SiPMs is their rather high correlated noise which might lead to a reduced photon counting resolution and a detailed study of this phenomenon is presented in chapter 7.

Finally chapter 8 presents a measurement of the photon-detection efficiency of the characterised SiPMs in a wavelength range of interest for fluorescence detection.

2. Cosmic Rays

This chapters aims to give an introduction to cosmic rays and extensive air showers. Cosmic rays are highly energetic particles from the cosmos, permanently hitting and penetrating the atmosphere of the Earth. At the top of the atmosphere about 98% of the charged particles are ionized nuclei and about 2% electrons. Of the nuclei about 87% are protons, 12 % α-particles and 1% heavier nuclei [1]. The emphasis here is on ultra-high-energy cosmic rays (UHECRs), i.e. cosmic rays with an energy greater than 10^{18} eV. Observation of these UHECRs is made difficult by the fact, that the cosmic ray flux follows a steeply falling power law spectrum and the flux of UHECRs can consequently be as low as one particle per century and square-kilometre[1]. Because of this rate, direct, e.g. satellite or balloon observations are not useful and large, ground based observatories are required for the study of UHECRs. Upon impact with the atmosphere an UHECR particle initiates a cascade in the atmosphere by interaction with the air molecules, producing an extensive air shower, very much like in a hadronic calorimeter. This shower can then be studied by ground based experiments, allowing to gain information about the primary particle such as the energy and arrival direction. It should be noted, that the composition of UHECRs is still a matter of discussion, in contrast to the previous composition statements. These numbers come from direct measurements of the lower part of the cosmic ray energy spectrum, which constitutes the vast majority of the total cosmic ray flux [1]. Unless otherwise noted the following information in this chapter are based on the content of [2] and further details can be found there and included references.

2.1 Properties

The existence of cosmic rays was discovered in 1912 by V. Hess in a series of balloon flights, where he measured the ionisation rate as a function of the altitude. In contrast to the expectation at the time, he measured an increase[2] of the rate with altitude, indicating an origin of the ionizing radiation from space instead as from earth. Ever since, many experiments have measured the flux of cosmic rays in differing energy ranges. This is a great experimental challenge as the energy spectrum of cosmic rays reaches over a vast energy range from the MeV range to at least 10^{20} eV. Shown in figure 2.1 is the flux of cosmic rays as a function of the energy as measured by various experiments. Above energies E of about 10^{11} eV the flux follows a power

[1] At an energy of 10^{20} eV.

[2] Above a certain altitude.

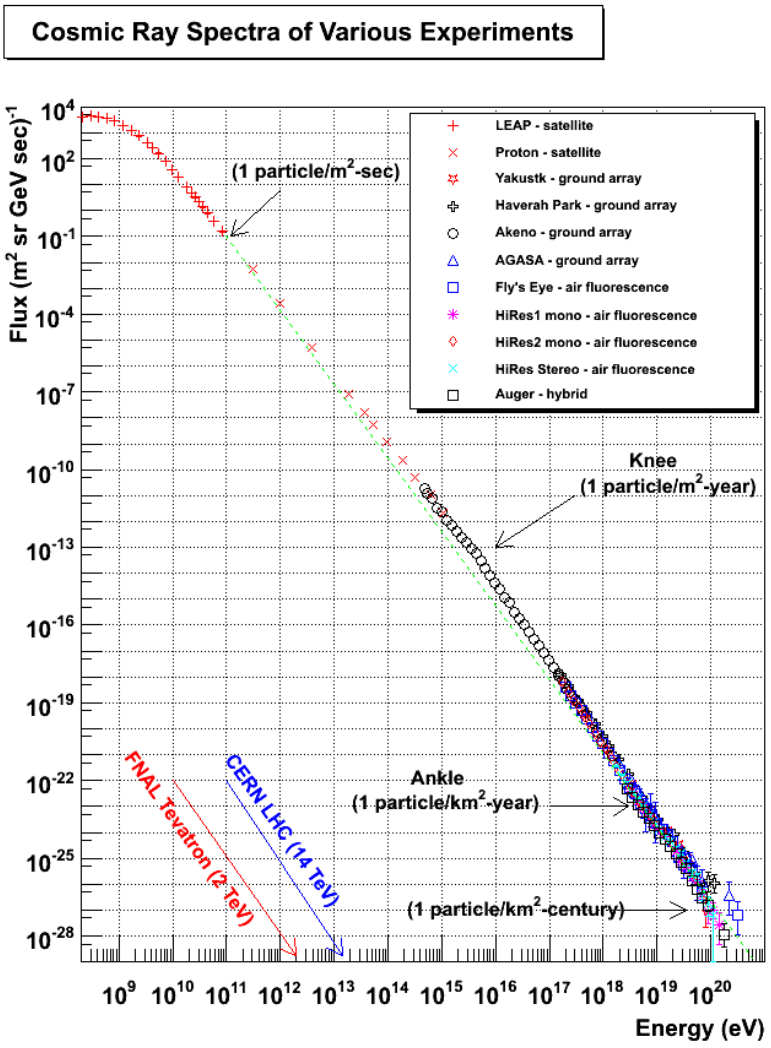

Figure 2.1: Cosmic ray energy spectrum as measured by various experiments. References for the included experiments can be found in [3]. The power law dependence of the flux is clearly recognisable.

law dependence i.e.

$$\frac{\mathrm{d}N}{\mathrm{d}E} \propto E^{\gamma}, \tag{2.1}$$

with the spectral index γ. This indicates a non-thermal but instead a stochastic acceleration process. A possible mechanism capable of generating such a power law spectrum is *diffusive, first order Fermi acceleration*, also called *diffusive shock acceleration*. In this model the accelerated particle passes repeatedly back and forth through shock fronts powered by supernovae explosions. In each passing cycle, the particle has an energy gain of $\Delta E \propto E$ and after each cycle there is a chance, that the particle is lost and does not pass the shock front again, producing a power law spectrum. Higher energetic particles are then simply particles which have remained longer in the shock region and thus had time to achieve higher energy. The maximum

achievable energy is determined by how long the particles remain in the source region. When their Larmor-radius

$$r_l = 1.08\,\mathrm{pc}\frac{E/\mathrm{PeV}}{Z \cdot B/\mu\mathrm{G}} \tag{2.2}$$

becomes larger than the extent of the source region, the particles will leave the source region. Here B is the magnetic field strength in the source region and Z is the particle charge. Putting the acceleration mechanism together with considerations of how long a particle of a certain energy can remain in a potential source region, the maximum achievable energy is given by

$$E_{\max} \approx 10^{18}\mathrm{eV} \cdot Z\beta_s \left(\frac{R}{\mathrm{kpc}}\right) \cdot \left(\frac{B}{\mu\mathrm{G}}\right). \tag{2.3}$$

Here R is the extent of the source region and β_s is the shock wave velocity in units of c. While this mechanism produces a power law spectrum, it should be noted that, especially for UHECRs, the exact acceleration mechanism and the sources are still largely unknown although many possible candidates, such as (in the case of UHECRs) active galactic nuclei and gamma-ray bursts exist.

The power law describing the flux is broken, i.e. the spectral index changes, resulting in a few interesting features. These can be better recognised by multiplying the steeply falling flux with the energy, e.g. $E^{2.5}$. This is shown in figure 2.2. Up to energies of $4 \cdot 10^{15}$ eV the index equals -2.7. The rate at the end of this range is about one particle per year and square-metre. Above this point the flux decreases even more steeply and the index drops to $\gamma \approx -3.1$. This feature is called the 'knee'. A further steepening, the 'second knee', occurs around $4 \cdot 10^{17}$ eV. Around $4 \cdot 10^{18}$ eV, at a rate of one particle per year and square-kilometre, the index changes again to -2.6. This feature is referred to as the 'ankle'. Above energies of $4 \cdot 10^{19}$ eV there is a strong suppression of the flux. Due to the interaction with the cosmic microwave background a cut-off energy of $6 \cdot 10^{19}$ eV for protons has been proposed. This is commonly referred to as the Greisen-Zatsepin-Kuzmin cut-off (GZK cut-off). Whether the observed drop-off is due to this cut-off or indicates the lack of sources, capable of accelerating particles to higher energies is still a debated question.
The ankle is usually interpreted to indicate the transitions from a flux dominated by galactic, to a flux dominated by extragalactic cosmic rays.
Different explanations exist for the cause of the knee. One popular theory assumes that galactic accelerators reach their energy limit at the knee. With equation (2.3) this would imply that lighter particles vanish from the galactic flux at lower energies than heavier particles, leading to a shift to a heavier composition.
Additionally the knee marks roughly the point where direct, e.g. balloon based, observations are no longer sensible due to the low rate. For higher energies large, ground based detection arrays are required, which gain information about the primary particle by studying the air shower it causes.

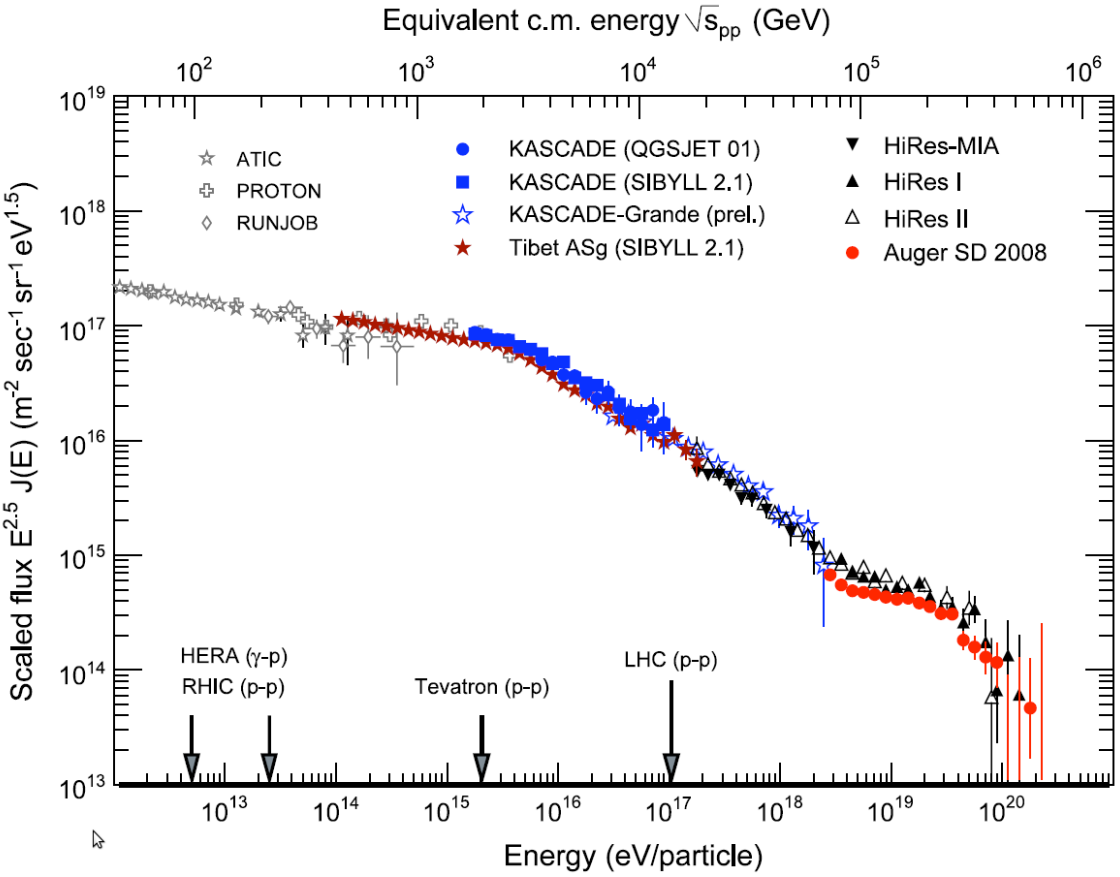

Figure 2.2: Scaled cosmic ray energy spectrum as measured by various experiments. The flux has been multiplied with $(\text{Energy})^{2.5}$. For a details on the experiments see [2] and included references.

2.2 Extensive Air Showers

Due to the very low flux of UHECRs large area, ground based detectors are required for their study. These detectors do not observe the primary particles directly but instead observe the extensive air showers induced by them.
An understanding of this process is required to gain information about the primary particle from the shower.
When the primary particle hits the atmosphere it usually undergoes an inelastic scattering with a nitrogen or oxygen molecule. In this first interaction a multitude of additional particles is created, which in turn can create new particles initiating a cascade. This is shown in figure 2.3.

The shower can be considered to consist of three components: an electromagnetic, a hadronic and a muonic/neutrino component [4]. A schematic of these components can be found in figure 2.3. When the primary particle is a hadron, the first collision will produce new hadrons, mainly nuclear fragments, neutral and charged pions ($\pi^{\pm}, \pi^0$) and kaons ($K^{\pm}, K^0_{S/L}$) [4]. These hadrons can then collide with further air

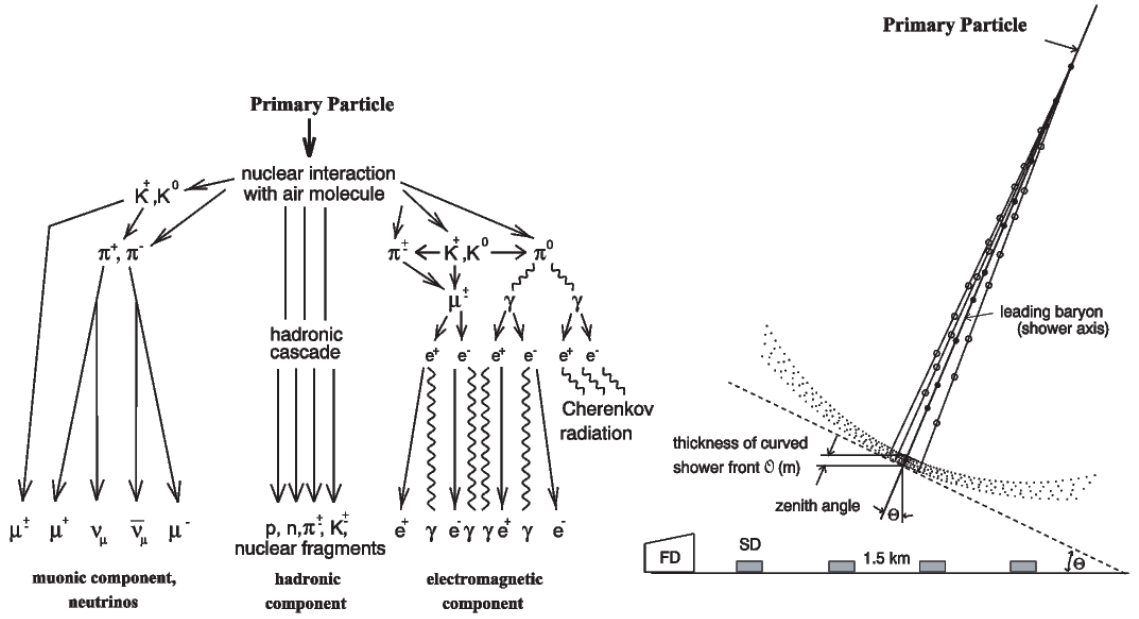

Figure 2.3: Schematic shower development. Left) Illustration of the components of the cascade. Right) Shape of the shower (not to scale). The leading particles form a disk with a thickness in the order of metres, while the lateral distributions can reach an extend in the order of kilometres. FD and SD are detector stations of a ground based observatory. Taken from [5].

molecules driving the hadronic component forward, or, depending on their lifetime and density of the atmosphere surrounding them, decay before interacting. For example the charged pions, with a lifetime of $\tau = 2.6 \cdot 10^{-8}\,\mathrm{s}$ [6], decay mainly via $\pi^{\pm} \longrightarrow \mu^{\pm} + \nu$. Especially at higher altitudes with a less dense atmosphere pions may decay before interacting, giving rise (together with the charged kaons) to the muonic component of the shower [4]. Due to the rather long muon lifetime of $\tau = 2.2 \cdot 10^{-6}\,\mathrm{s}$ and the very low neutrino cross-section this component largely decouples from the shower development.

The produced neutral pions have a very short lifetime of $\tau = 8.4 \cdot 10^{-17}\,\mathrm{s}$ and decay nearly instantly via $\pi^0 \longrightarrow \gamma + \gamma$ (98.8% of decays) or $\pi^0 \longrightarrow e^+e^- + \gamma$ (1.2% of decays) [6]. These produced photons, electrons and positrons give rise to the electromagnetic component[3]. In this cascade the photons produce electron-positron pairs by the interaction with a nucleus N via $\gamma + N \longrightarrow e^+e^- + N$ and the electrons/ positrons generate Bremsstrahlung[4] via $e^{\pm} + N \rightarrow e^{\pm} + \gamma + N$. The produced Bremsstrahlung photons can then again create electron-positron pairs and so on. The cascade begins to end when the energy of the electrons and positrons drops below a critical energy of $E_C \approx 90\,\mathrm{MeV}$ in air, where they start losing more energy via ionisation then through radiation [4].

The cascade itself moves with nearly the speed of light towards the ground. The

[3]These particles can also be the primaries, causing a purely electromagnetic shower.

[4]Bremsstrahlung is the dominant energy loss process for electrons during the cascade.

shower particles form a front, the shower disk, with a thickness of up to a few metres, while the lateral extent can reach several kilometres. The cascade ends when the involved particles have insufficient energy to drive the cascade further, or the cascade impacts on the ground.

One method to gain information about the primary particle is to study the distribution of the electrons/positrons and muons on the ground. By measuring the distribution of particles on the ground, together with the information about their arrival time, it is possible to reconstruct the energy of the primary particle, as well as the arrival direction. This method can be dated back to the late 1930s and to P. Auger, who used Wilson chambers and Geiger Müller tubes to study coincidences. He was able to find coincidences from counters separated up to 300 m and concluded that this was due to secondary particles generated by cosmic rays.
In this method, the reconstruction of the energy of the primary particle normally relies on shower simulations, introducing systematic uncertainties on the result.
Another method to gain information about the primary particle is to study the longitudinal shower profile. Here the electromagnetic component is very significant as it constitutes about 90% of the cascade components. A good approximation of the number of electrons/positrons N_e at a given atmospheric depth X is given by the Gaisser-Hillas function[5]

$$N_e(X) = N_{\max} \left(\frac{X - X_0}{X_{max}} \right)^{(X_{\max} - X)/\Lambda} \exp\left(\frac{X_{\max} - X}{\Lambda} \right). \tag{2.4}$$

Here $N_{\max}$ is the maximum number of particles in the shower and $X_{\max}$ the atmospheric depth of the shower maximum. X_0 is the position of the first interaction and Λ the absorption length. $N_{\max}$ is proportional to the energy of the primary particle and $X_{\max}$ is proportional to the logarithm of the primary energy.

If these parameters can be identified for a given shower, it is possible to reconstruct the energy of the primary particle. Additionally, because $X_{\max}$ also depends on the mass of the primary particle, one can gain information about the chemical composition of UHECRs.

To be able to determine these parameters, information about the longitudinal shower profile is needed. This information can be obtained by using imaging telescopes to study the fluorescence light emitted as consequence of the shower. This is described in the next chapter.

[5]For a fit with this function see figure 3.3 on page 12.

3. Fluorescence Detection of Extensive Air Showers

Fluorescence detection can be used to measure the longitudinal profile of extensive air showers directly for primary particle energies above about 10^{17} eV [2]. This technique allows for a calorimetric measurement of the shower energy with minimal reliance on shower models [7]. At first, this chapter gives a short description of the technique and the mechanisms behind it in general. This is followed by one example of a current experimental application, the fluorescence detector (FD) of the Pierre Auger Observatory. The chapter ends with the presentation of a prototype design for a possible future fluorescence telescope with SiPMs as the light sensitive detector component. The SiPM characterisation studies in this thesis have been performed to use the results and the developed methods in the construction of this prototype.

3.1 The Fluorescence Detection Technique

During the passage of the air shower through the atmosphere the charged component of the shower, i.e. mostly the electrons and positrons, excites the nitrogen molecules in the atmosphere. After a relaxation time in the order of 10 ns the nitrogen relaxes back into the ground state emitting fluorescence light. This light is emitted isotropically. Of relevance for the fluorescence emission are two transitions of electronic states of nitrogen, called 2P and 1N. Each of which can be excited in many vibrational and rotational states, resulting in fluorescence light that is a composition of many wavelength bands in a wavelength range between 300 and 400 nm (near ultraviolet) [2]. A measurement of the wavelength spectrum of nitrogen is shown in figure 3.1.

The general idea behind fluorescence detection is to measure this fluorescence light as a function of the slant depth X and by this, after reconstruction, finally the longitudinal shower profile[1] $\frac{dE}{dX}$ of the shower [8]. This can be done by imaging telescopes as shown in figure 3.2. These telescopes are usually (such as in e.g. [8, 9]) composed of many individual pixels, observing different solid angles in the total field of view of the telescope separately. After the measurement, the first step in the reconstruction is generally the determination of the axis of the observed shower. If only one telescope is used or has observed the specific shower, the timing information of the individual pixels has to be used to reconstruct the axis [8, 9]. In the case that two or

[1] The deposited energy E along the track X.

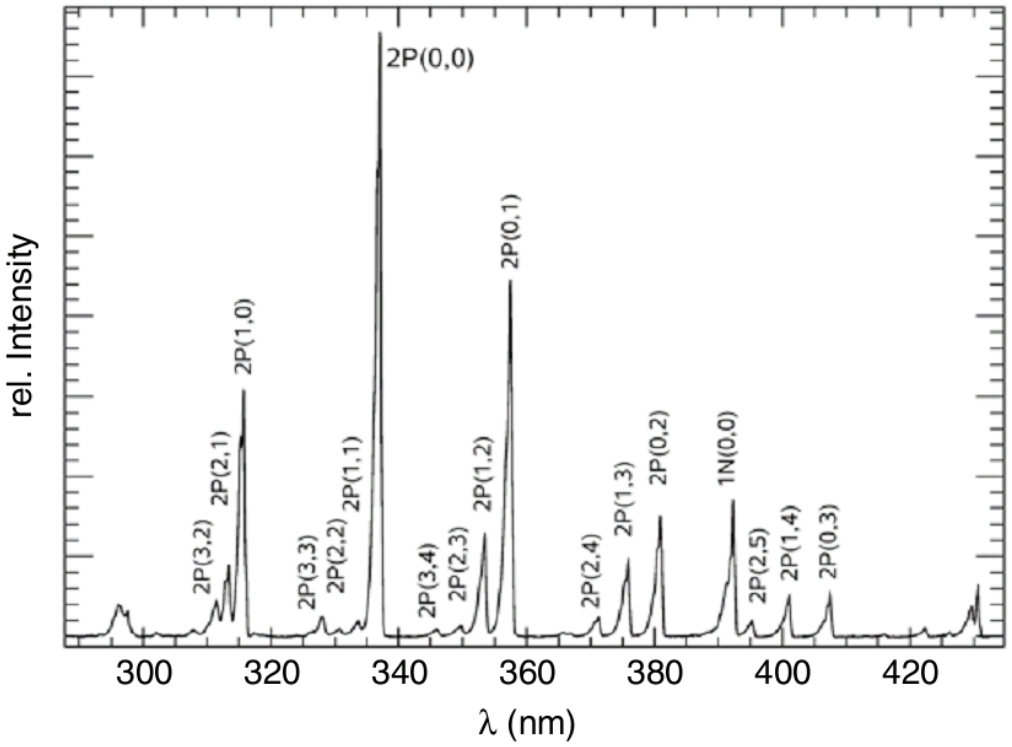

Figure 3.1: Fluorescence light spectrum of dry air as measured by the AIRFLY experiment with an electron beam of 3 MeV, a temperature of 20 °C and pressure of 800 hPa. The excited electronic states are 1P and 2P, the change of the vibration quantum number is denoted with (ν', ν''). Taken from [2].

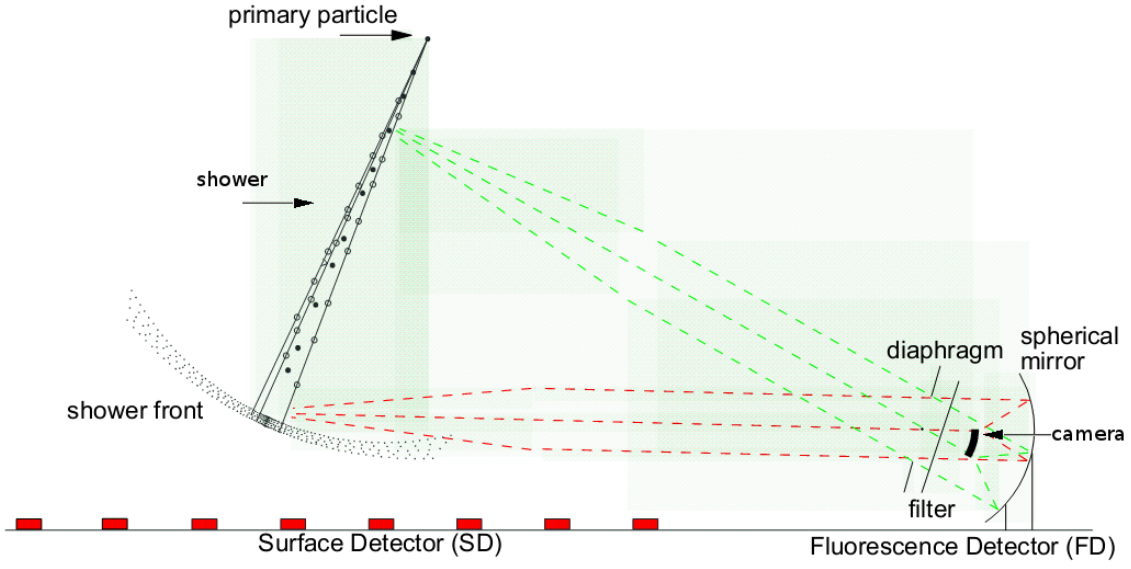

Figure 3.2: Schematic of the principle of fluorescence detection as implemented at the Pierre Auger Observatory. The fluorescence light emitted by the shower is observed by a ground based imaging telescope. Modified from [10].

more telescopes have observed the same shower, the axis can also be calculated from the intersection of the observed shower-detector planes by the individual telescopes.

Once the shower geometry is known, the light observed by the telescope can be reconstructed back to the number of registered fluorescence photons N_γ at a slant depth X along the path. These quantities are related to the quantity of interest, the total energy $\mathrm{d}E^{\mathrm{tot}}_{\mathrm{dep}}$ deposited in atmospheric layer of thickness $\mathrm{d}X$ by [7]

$$\frac{\mathrm{d}N_\gamma}{\mathrm{d}X} = \frac{\mathrm{d}E^{\mathrm{tot}}_{\mathrm{dep}}}{\mathrm{d}X} \int Y(\lambda, P, T, u) \cdot \tau_{\mathrm{atm}}(\lambda, X) \cdot \varepsilon(\lambda) \cdot \mathrm{d}\lambda \tag{3.1}$$

Here, Y is the fluorescence yield, i.e. the number of produced fluorescence photons per unit of energy deposited. The yield at a given wavelength λ depends on the atmospheric pressure P, temperature T and the humidity u.
The transport of the fluorescence light through the atmosphere is described by τ_{atm}, which includes all losses due to absorption, Rayleigh and Mie scattering [7]. The efficiency of the detector is given by ε.
This formula implicitly assumes, that the fluorescence yield is not dependent on the energy of the electrons/positrons which excite the nitrogen. This is approximately the case for the energies involved in air showers [2]. For the 337 nm fluorescence band the yield is (5.05 ± 0.71) photons/MeV of deposited energy in dry air, at a pressure of 1013 hPa and a temperature of 293 K [8].
With the knowledge[2] of τ_{atm} and ε, the reconstruction of the deposited energy along the shower track is possible. Once this is known a Gaisser-Hillas function (see equation (2.4)) can be fitted to the data. An example of this is shown in figure 3.3. This fit then yields the position of the shower maximum X_{max}. Because the Gaisser-Hillas function provides a complete description of the longitudinal profile, the complete deposited energy of the shower, which constitute about 90% of the total energy [2], can be calculated by integration over the fit.

This energy then needs to be corrected for contamination in the observed light, in particular Cherenkov light from the shower, and for the 'invisible energy' carried away by neutrinos and high energy muons. The latter is usually performed with the aid of shower simulations [8, 9].

To be able to observe the fluorescence light signal, fluorescence telescopes can only be operated during moonless nights.

In summary, the fluorescence detection technique allows for a calorimetric measurement of the energy of the primary particle, a measurement of the arrival direction and the position of maximum shower development X_{max}. The latter is of interest, as X_{max} is sensitive to the mass of the primary particle.

Because of the low flux of UHECRs, the detector must be able to observe even very distant showers to achieve reasonable statistics. Additionally fluorescence light is

[2] Obtained by, among other things, monitoring the environment conditions, a knowledge of the properties of the detector and consideration of the mechanisms involved in light absorption and scattering. This is an incomplete list and the process is highly non-trivial.

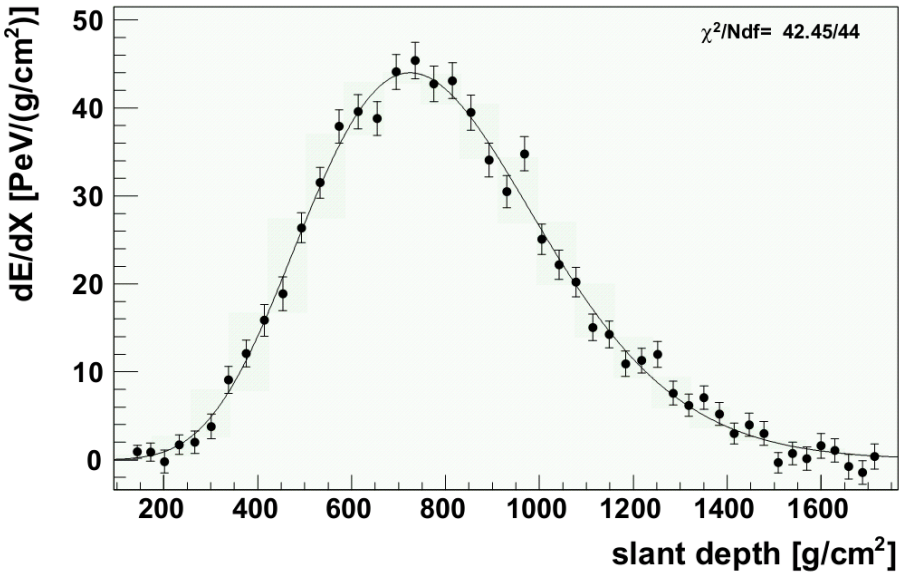

Figure 3.3: Energy deposit profile of an air shower, reconstructed from the light observed by one fluorescence telescope of the Pierre Auger Observatory. The reconstructed energy of the event is $(3.0 \pm 0.2) \cdot 10^{18}$ eV. Taken from [8].

emitted isotropically and consequently possesses a flux which drops quadratically with the distance. Both facts together stress the need for a very efficient light collection and detection system.

In the following, one existing fluorescence detector, the fluorescence detector of the Pierre Auger Observatory, and a design for a prototype of a fluorescence detector with SiPMs as the light sensitive component are presented.

3.2 The Fluorescence Detector of the Pierre Auger Observatory

The Pierre Auger Observatory is currently the largest experiment for the observation of ultra-high-energy cosmic rays. It is located in the Argentinian pampa near the city of Malargüe. The observatory is a hybrid detector consisting of a surface detector (SD) of water-Cherenkov detectors and a fluorescence detector (FD). The SD consists of 1600 detector stations, each filled with 12 tonnes of water, positioned in a triangular grid with 1500 m spacing. As described in the previous chapter, the surface detector uses the distribution of the electrons and muons on the ground to reconstruct the energy of the primary particle and the arrival direction. The resulting instrumented area of 3000 km^2 is overlooked by the fluorescence detector which consists of 24 fluorescence telescopes[3], housed in four telescope buildings, enclosing the array. A schematic view of the Auger Observatory is shown in figure 3.4. Each

[3]Not included are the 3 telescopes of the HEAT extension.

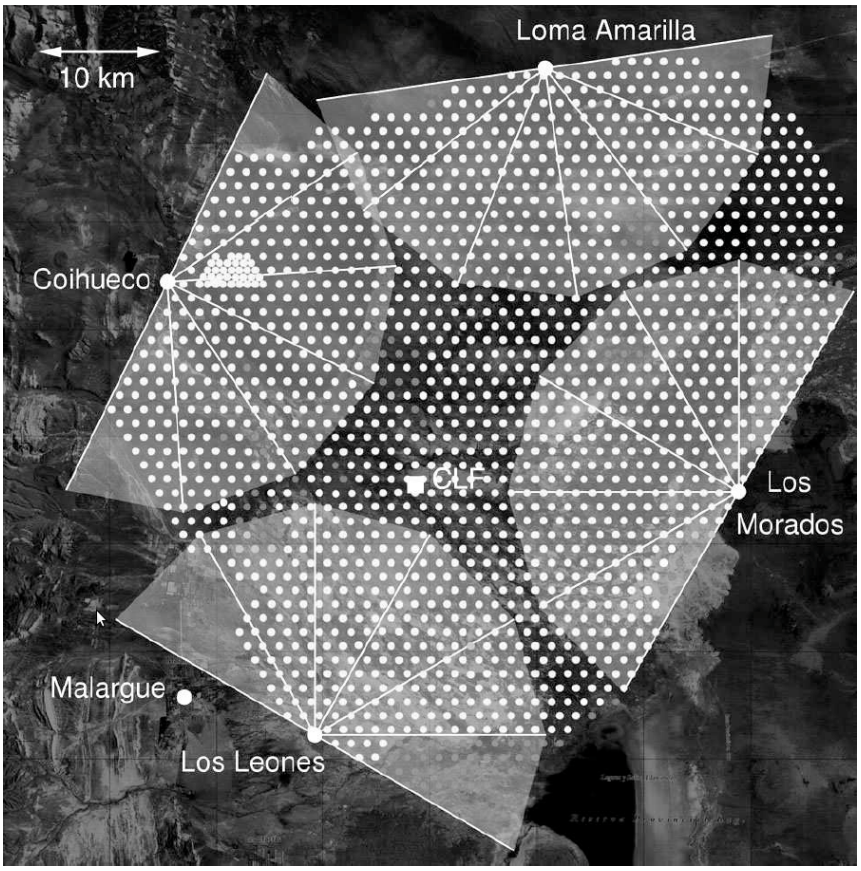

Figure 3.4: Layout of the Pierre Auger Observatory (March 2009). The dots represent the SD stations. The cluster of SD station near Coihueco is the infill array. The grey segments show the field of view of the 24 fluorescence telescopes. CLF is the Central Laser Facility. Not shown are the three HEAT telescopes near Coihueco. Taken from [8].

of the 24 FD telescopes has a field of view of 30° x 30°. Depicted in figure 3.5 is a schematic view of a single FD telescope. The aperture of the telescope has a diameter of 2.2 m and consists of an optical filter and a corrector ring. After the aperture the light is focussed on the spherical focal surface by a spherical mirror. The focal surface consists of 440 hexagonal camera pixels, each with a field of view of 1.5 °. Every pixel consists of one photomultiplier tube. The signal of each pixel is digitised by an analog to digital converter (ADC) with a sampling rate of 10 MHz (integration time of 100 ns). This time resolved signal is used for the reconstruction of first, the shower geometry and then secondly the longitudinal shower profile as described in the previous section. In the case of the Pierre Auger Observatory the accuracy of the reconstruction of the shower geometry is significantly enhanced in *hybrid events*, for which one or more SD detector stations provide additional information about the position of the shower on the ground. Likewise, the calorimetric measurement of the shower energy by FD can be used to calibrate the energy reconstruction of SD. With this configuration FD can observe events up to the highest energies, reaching

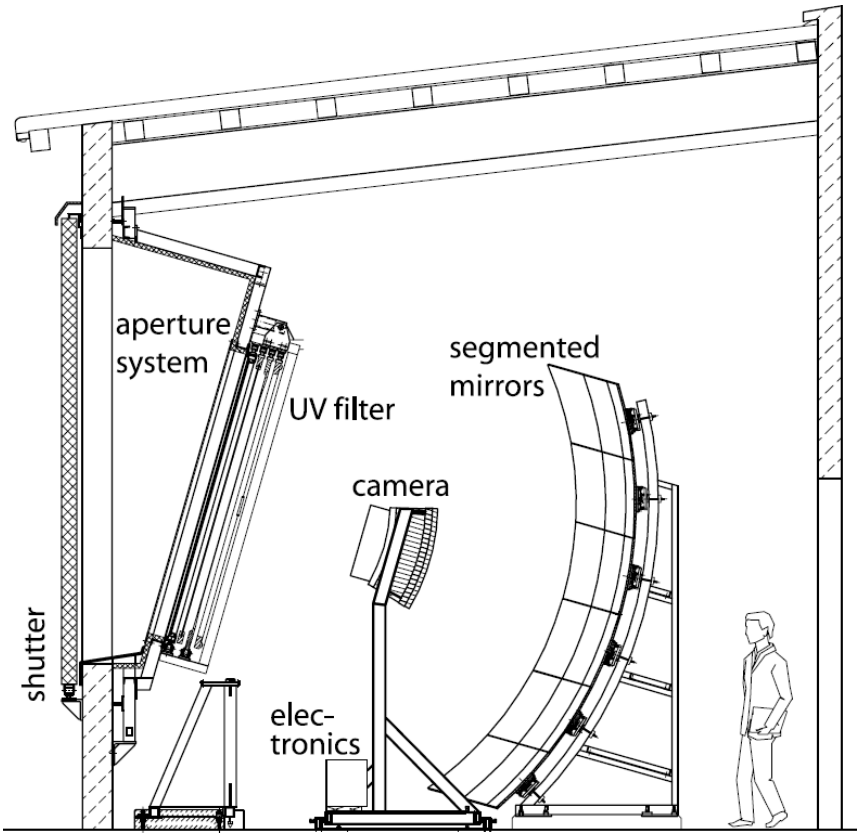

Figure 3.5: Schematic view of a fluorescence telescope of the Pierre Auger Observatory. Taken from [8].

a triggering efficiency of 100% for energies above 10^{19} eV over the entire array of the surface detector. Since showers can only be observed on moonless nights the duty cycle is around 13%.
The information in this section has been based on [8].

3.3 FAMOUS

To test the feasibility of SiPMs as the light sensitive component of a fluorescence telescope, the construction of a prototype fluorescence telescope will be undertaken at III. Phys. Inst. A, RWTH Aachen University [11]. The name of the prototype is FAMOUS[4]. The optical design has been developed in [12] and is shown in figure 3.6. A Fresnel lens of 0.511 m diameter and focal length, made of UV-transparent PMMA[5] is used to focus the incoming light on the focal plane. The focal plane consists of 64 SiPM pixels, each with a field of view of 1.5 °. Because the sensitive area of SiPMs is rather small Winston cones[6] are used to concentrate the light on the

[4]First Auger Multi pixel photon counter camera for the Observation of Ultra-high-energy cosmic ray Showers

[5]Polymethyl-methacrylate, a transparent thermoplastic (Plexiglas).

[6]Winston cones are very efficient light concentrators [13].

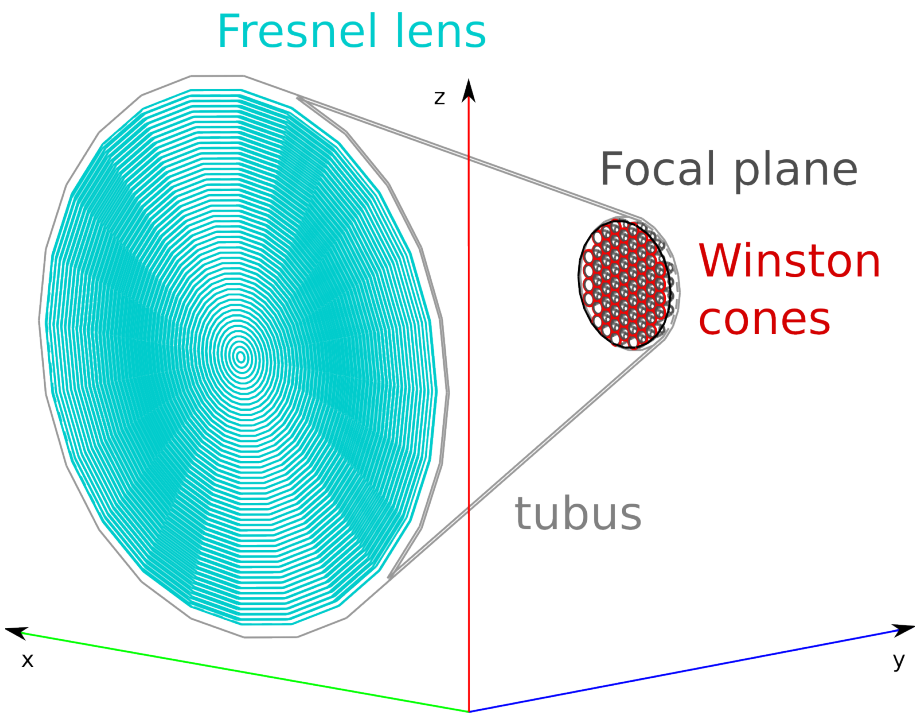

Figure 3.6: Optical design of the FAMOUS prototype. The actual number of grooves of the Fresnel lens has been reduced by a factor ten in this image. In this design the SiPMs are located at the exit of the Winston cones. The diameter is equal to the focal length of 0.511 m. The total field of view is 12 ° and each of the 64 SiPM pixels has a field of view of 1.5 °. Taken from [12].

SiPMs behind the cones. This has the additional benefit of improving the signal to thermal noise ratio. The entrance radius of the cones is 6.7 mm and the exit radius is 3 mm. The planned SiPM type is a two by two array of a 3x3 mm^2 active area SiPM type. Two different 3x3 mm^2 SiPM types are presented in the next chapter and characterised in this thesis. Besides the optical design and characterisation of the used SiPMs, a knowledge of the background, caused by the night sky is necessary for the operation of a fluorescence telescope. Measurements of the local night sky brightness have been performed in [11], indicating this will be the dominant background source.
Simulations of the expected performance of the telescope have been performed, showing that the design is able to observe air showers [12]. Additionally star tracking and laser shots are can be performed to gain experience in and testing the performance of using SiPMs as fluorescence light detectors. The prototype is currently in the early stages of construction and is expected to be completed in 2012.

At this point one should note that SiPMs can not only be used for fluorescence detection of extensive air showers. They can also be used to detect the Cherenkov light induced by the shower particles. The FACT collaboration has constructed a Cherenkov telescope based on SiPMs [14]. The camera of the telescope possesses 1440

pixels, each made of one SiPM[7] and a solid Winston cone. First shower recordings are available from the telescope[8].

[7] The 3x3 mm^2, 50 µm cell pitch type, also studied in this work (see next chapter).
[8] Available at http://fact.ethz.ch/first/, visited 08.12.11.

4. Introduction to Silicon Photomultipliers

After the previous chapter outlined the need for light sensors with a high photon detection efficiency and capability to detect very low photon fluxes, this chapter gives an overview of the light sensors studied for this purpose in this thesis, namely silicon photomultipliers (SiPMs). Because SiPMs are semiconductor devices the chapter begins with a short, basic introduction to semiconductors. This is followed by a description of the working principle of SiPMs, and ends with an overview over typical SiPM properties in general and the details of the studied SiPM types in particular.

4.1 Semiconductor Basics

In free atoms the electrons bound to the nucleus occupy discrete energy states. If a large number N of atoms are brought together their energy states begin to split, since no two fermions may occupy the same state, as described by the Pauli principle. When the atoms are close enough, the energy states are N times degenerate and, for $N \to \infty$ they form bands, rather than discrete states. These bands broaden, merge and split again with even closer spacing [15]. In the case of silicon an example of this can be found in figure 4.1. The marked distance of 5.43 Å is the lattice spacing of crystalline silicon, which crystallises in a diamond cubic crystal structure [16] and is the used material in SiPMs.
The spacing between the bands may not be occupied by electrons creating a 'forbidden zone', while the energy bands themselves can be occupied. The band with the highest energy, still filled completely at a temperature of absolute zero is called the valence band and the band above it is the conduction band. The energy difference between the highest energy of the valence band E_V and the lowest energy of the conduction band E_C is the band gap E_g. It defines the properties of the material with regards to conductivity [15]. As the temperature increases, the electrons bound in the valence band may gain enough energy to cross over into the conduction band. In materials with a large energy gap ($E_g > 3\,\mathrm{eV}$ [17]) this generally does not happen, even at room temperature. Because the electrons in the valence band are still bound to their individual nucleus, no free charge carriers are available and the material is called an insulator. In contrast, materials where the conduction band and the valence band overlap, or the conduction band is partially filled, many electrons are located in the conduction band. Here they may be regarded as free charge

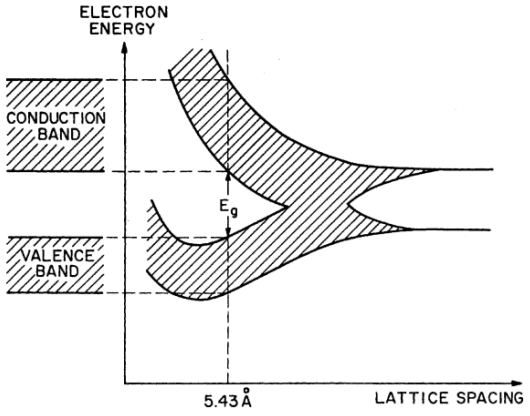

Figure 4.1: Band separation in silicon as a function of the atom distance. Marked distance is the lattice spacing of crystalline silicon. Taken from [15].

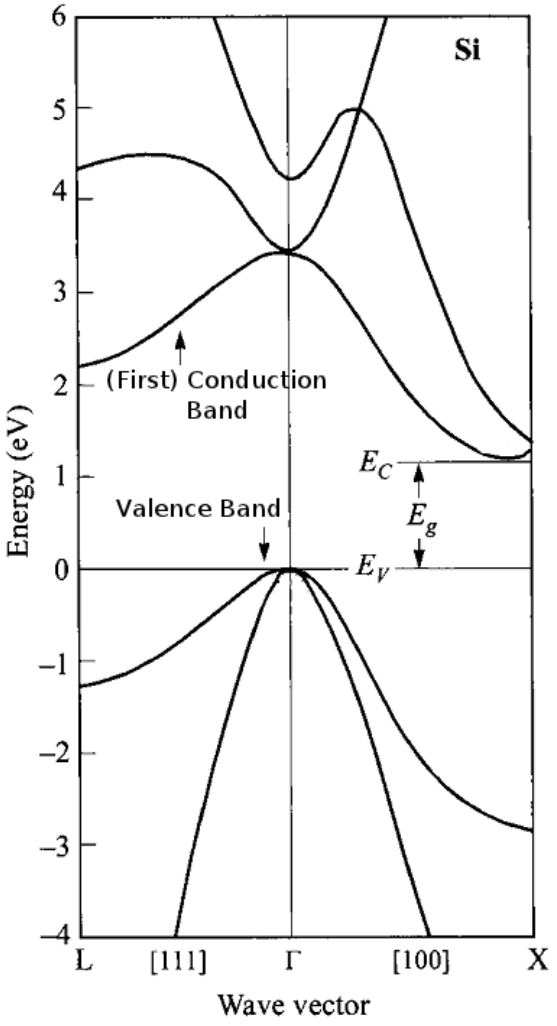

Figure 4.2: Band structure in silicon as a function of the position the reciprocal lattice. The minima of the valence and conduction band do not overlap, making silicon an indirect semiconductor. Adapted from [16].

carriers, with a reduced mass replacing their actual mass, and the material is called a conductor [17].
A semiconductor, such as silicon, lies in between these two cases. Here the band gap is smaller than for an insulator, and a small fraction of electrons occupy the valence band, causing an intrinsic conductivity, which is small in comparison to conductors. Silicon has a band gap of 1.14 eV at room temperature and its band structure can be found in figure 4.2. As shown there, the minimum distance between the two bands is located at different positions in the reciprocal lattice. This makes silicon an indirect semiconductor and more energy than the band gap is required, to excite an electron

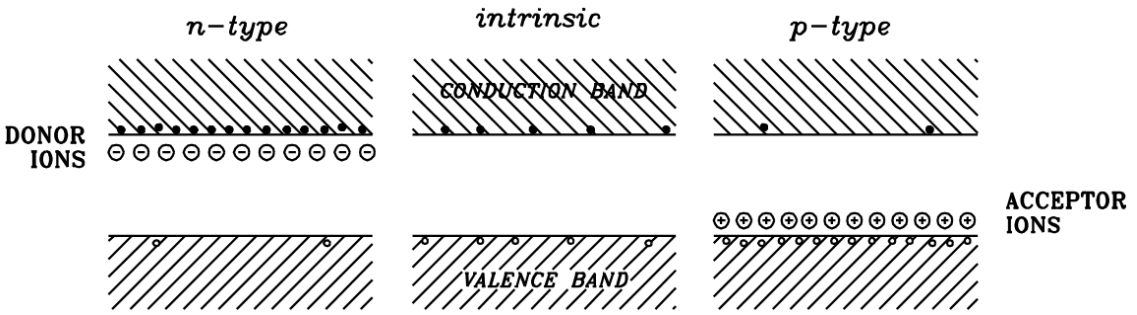

Figure 4.3: Middle) Intrinsic semiconductor with intrinsic carrier density in the valence band. Left/Right) n/p-doped semiconductor. The doping creates easily ionizable donors/acceptors near the conduction/valence band increasing the intrinsic conductivity. Taken from [15].

to the conduction band, as additional momentum has to be transferred to the crystal lattice [15]. Every time an electron is excited to the conduction band, a hole is left in the valence band. Like the negatively charged electron in the conduction band, the hole may be regarded as a positive charge carrier, which can move freely in the valence band, again with a reduced mass. Since the hole is created together with the excitation of the electron this process is also referred to as the creation of an electron-hole pair or eh-pair for short [15].

A very important aspect of semiconductors is, that they can be doped, which increases their intrinsic conductivity. In pure, crystalline silicon, each silicon atom shares four valence electrons with its neighbours in four covalent bonds [16]. By substituting some of the silicon atoms with e.g. phosphorous atoms, with 5 valence electrons of which one is nearly-free, an additional energy state close to the conduction band is created (see figure 4.3). At room temperature most of the electrons from these donors will be located in the conduction band, leaving behind ionized donors. A semiconductor doped this way is referred to as a n-type semiconductor. In analogy, by substituting silicon atoms with atoms with 3 valence electrons, e.g. boron, an additional energy state close to the valence band is created. The acceptor levels easily take up electrons from the conduction band, creating a hole. This kind of semiconductor is called p-doped. The band diagrams of an intrinsic, p- and n-doped semiconductor can be found in figure 4.3.

4.2 p-n Junction

A p-n junction is the base for many semiconductor devices and detectors including SiPMs. It is created when a p- and an n-doped semiconductor are brought into contact as is illustrated in figure 4.4. In the n-region, the concentration of electrons is higher, making them the majority charge carriers, and the holes the minority charge carriers. The same is true vice versa for the p-region. Due to the difference in concentration, electrons diffuse into the p-region and holes into the n-region. This

results in an excess negative charge in the part of the p-region connected to the n-region and vice versa, due to the remaining ionized donors and acceptors. This in turn creates an electrical field over the junction, which causes a reverse drift current of electrons and holes. The electrical field also quickly sweeps any free charge carriers out of the transition region, creating a layer nearly empty of free charge carriers, called the depletion layer or space charge region, since it is still filled with the ionized donors and acceptors [15].
In thermal equilibrium diffusion and drift current cancel each other out and the net current is zero. The resulting potential difference across the junction is called the built-in potential V_{bi} and the energy levels between the n- and the p-layer are shifted by $q \cdot V_{\mathrm{bi}}$ as shown in figure 4.4 a), with q being the elementary charge. Also shown in this image is the depletion layer, consisting of the locally fixed, ionized donors and acceptors.

Under the assumption, that the change from the neutral regions on both sides to the depletion layer is abrupt, the properties of the p-n junction are explored in more detail. First the spatial extend in the n-region d_n and in the p-region d_p, can be derived from the density of donors N_D and acceptors N_A and requiring, that the net charge over the total junction is zero. This results in the relation

$$N_A \cdot d_p = N_D \cdot d_n, \tag{4.1}$$

i.e the lower the relative concentration on one side, the longer the extend of the depletion layer in this side. In the coordinate system given in figure 4.4 b), where the transition from the p- to the n-region is at $x = 0$, the electrical field E and the potential difference V are given by [16],

$$E(x) = -\frac{q \cdot N_A}{\varepsilon_s}(x + d_p) \tag{4.2}$$

$$V(x) = \frac{q \cdot N_A}{2\varepsilon_s}(x + d_p)^2 \tag{4.3}$$

in the depleted p-region and

$$E(x) = -\frac{q \cdot N_D}{\varepsilon_s}(d_n - x) \tag{4.4}$$

$$V(x) = \frac{q \cdot N_A}{2\varepsilon_s} d_p^2 + \frac{q \cdot N_D}{2\varepsilon_s}\left(d_n - \frac{x}{2}\right) x \tag{4.5}$$

in the depleted n-region. Here ε_s represents the permittivity in silicon. The electrical field is zero outside of the depletion layer. An illustration of these quantities is shown in figure 4.4 b).
In this approximation, the field grows linearly towards the centre of the junction and reaches its maximum value

$$|E_m| = \frac{q \cdot N_A \cdot d_p}{\varepsilon_s} = \frac{q \cdot N_D \cdot d_n}{\varepsilon_s} = \sqrt{\frac{2q}{\varepsilon_s} \cdot \frac{N_A N_D}{N_A + N_D} \cdot V_{\mathrm{bi}}} \tag{4.6}$$

at the centre [15]. The total width of the depletion zone d is given by

$$d = \sqrt{\frac{2\varepsilon_s}{q} \cdot \frac{N_A + N_D}{N_A N_D} \cdot V_{\mathrm{bi}}}. \tag{4.7}$$

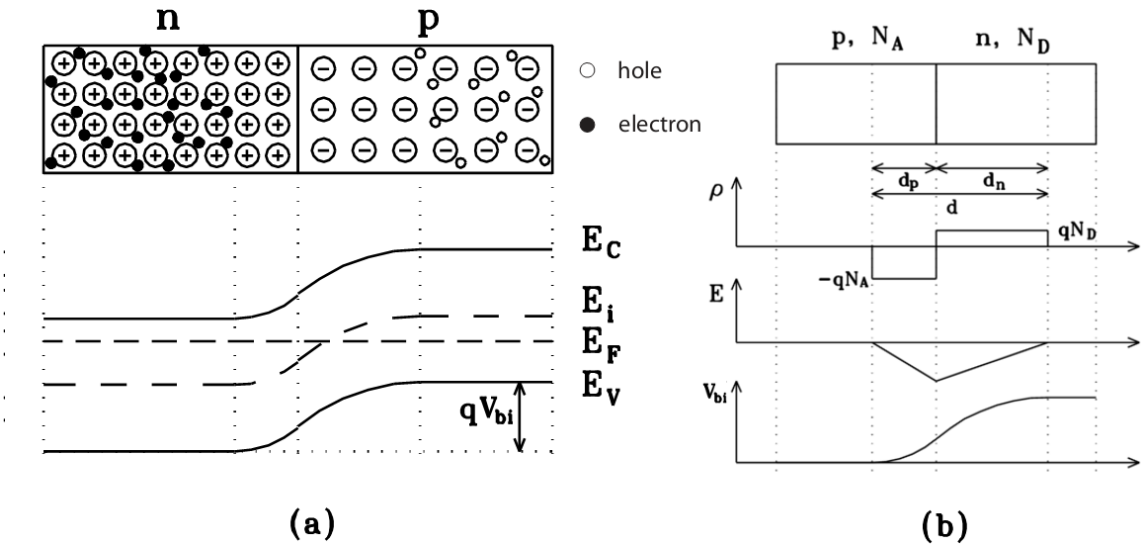

Figure 4.4: a) p-n junction in thermal equilibrium. E_F is the Fermi energy and E_i the Fermi level for intrinsic semiconductors. b) Charge density ρ, electrical field E and built-in potential V_{bi} across a p-n junction in the abrupt approximation. Taken from [15].

As can be seen, both the maximum electric field and the width of the deletion region are proportional to $\sqrt{V_{\text{bi}}}$.

A p-n junction already permits the detection of light. An incoming photon of sufficient energy can generate a eh-pair upon absorption in the silicon. If this pair is created in the depletion region it will be separated by the electrical field[1] and a (theoretically) measurable photo-current is generated when both sides are connected with external leads over an ampere-meter[2] [15]. For the detection of single photons however, the current is far too low in practical application. As fluorescence detection requires the detection of very few photons an intrinsic amplification is required for the detection at the single photon level.

4.3 Avalanche Photodiodes and Geiger-Mode Avalanche Photodiodes

The internal amplification mentioned in the previous section can be achieved by applying an external voltage V to the p-n junction. In the case a reverse bias voltage, i.e. $V < 0$, is applied, the width of the depletion zone and the strength of the electrical field increase. This can be described with the substitution of $V_{\text{bi}} \to V_{\text{bi}} - V$ in formulae (4.6) and (4.7) [15]. In the case of an abrupt, one-sided p-n junction,

[1] As opposed to the undepleted region, where the generated charge carriers will quickly recombine.

[2] This principle is employed by a PIN diode, which is described and used as part of the measurements contained in chapter 8.

where one side has a much higher doping than the other side these equations simplify to

$$|E_m| = \sqrt{\frac{2qN}{\varepsilon_s} \cdot (V_{\mathrm{bi}} - V)} \tag{4.8}$$

$$d = \sqrt{\frac{2\varepsilon_s}{qN} \cdot (V_{\mathrm{bi}} - V)}. \tag{4.9}$$

In the case that the doping concentration on the n side is much higher, i.e. $N_D \gg N_A$, this is indicated by referring to this junction as a p-n$^+$ junction and N=N_A and vice versa [15]. With the charge contained in the depletion layer and the variation of the width of the depletion layer by a change in the external voltage, a capacitance per unit area of

$$C_D = \frac{\varepsilon_s}{d} = \sqrt{\frac{q\varepsilon_s N}{2} \cdot \frac{1}{(V_{\mathrm{bi}} - V)}} \tag{4.10}$$

can be assigned to the depletion zone [15].

With the increase in the strength of the electrical field, the charge carriers in the depletion region will experience a greater acceleration than with the built-in field alone. For example, the electron of a created eh-pair[3] at the end of the depletion region in the p-layer, will drift towards the junction. During the drift the electron will be repeatedly accelerated by the field and de-accelerated by collisions with the lattice. As the strength of the field increases towards the junction (see previous section) the electron may gain enough energy to create an additional electron-hole-pair in a collision through impact ionization. The newly created carriers then get accelerated themselves and can generate new carriers as well, creating an avalanche. With the field-dependent ionisation-coefficients α_n and α_p the change in the concentration of electrons d_n and holes d_p in the region $\mathrm{d}x$ can by written as [15]

$$\mathrm{d}_p = \mathrm{d}_n = \alpha_n n(x)\mathrm{d}x + \alpha_p p(x)\mathrm{d}x. \tag{4.11}$$

A measurement of the ionisation-coefficients for electrons and holes can be found in figure 4.5 for silicon, germanium and SiC. As can be seen, the ionisation coefficient is higher for electrons than for holes in silicon. This has the consequence that there is a range of possible reverse bias voltages where electrons gain enough energy for impact ionisation, but holes do not. In this case such a junction is referred to as an avalanche photodiode. Because holes do not contribute to the avalanche, the avalanche in such a diode develops only in one direction, as shown in figure 4.7 and ends, when the electrons leave the high field region. With this arrangement an intrinsic gain is achieved, and smaller light fluxes can be detected. For example in PIN diodes, which are based on p-n junctions with no or very low reverse biases applied and no internal gain, the minimum, practically detectable photon signal at a given time, is in the order of a few hundred photons. In contrast avalanche photodiodes can detect a few tens of photons. The avalanche process provides typical gains between 50 and 200 [18]. While this already represents an increase in the sensitivity with regards to light detection, the sensitivity is still insufficient for the detection of

[3] E.g. through thermal excitation or an absorbed photon of sufficient energy in the silicon.

single photons. This can be achieved by operating the diode at voltages above the so called breakdown voltage. Above this voltage electrons *and* holes gain enough energy to create secondary eh-pairs. Now the avalanche diverges (see figure 4.7) and needs to be stopped externally to end. This can be done by placing the, now called Geiger-mode avalanche photodiode (GAPD), in series with a high-ohmic resistor, the quenching resistor [18]. The current produced during the avalanche causes a voltage drop over the resistor and this reduces the voltage over the diode until it falls below the breakdown voltage and the avalanche is ended. In this configuration the GAPD produces the same signal, regardless of the number of generated eh-pairs at a given time, i.e. it is a binary device and the proportionality to the incoming light flux is lost.
The achievable gains are between 10^5 and 10^7 and the minimum detectable signal is one photo-electron i.e. single photon detection is possible [18]. It should be noted that the mere generation of an electron-hole-pair by an absorbed photon is not a sufficient condition to create an avalanche. Shown in figure 4.6 is the probability, that, from a generated eh-pair either the electron or the hole triggers an avalanche as a function of the position in the depletion region. As can be seen, due to the different ionisation-coefficients, the probability that an electron initiates an avalanche is always higher in silicon. But also the position plays a role. The highest probability for an electron/hole to initiate an avalanche is achieved when they are created at the end of the depleted p/n region. In contrast the probability for an electron/hole initiated avalanche is rather low when it is created in the region where it is the majority charge carrier, as there is no drift towards the high field region. Because the absorption coefficient of light in silicon is strongly wavelength dependent, the size of the p and n regions have to be finely tuned to the photon wavelength range in which high sensitivity is desired. This issue is discussed in more detail in the introduction to chapter 8.
After the avalanche is initiated, the signal, i.e. the charge Q generated is independent of the number of primary eh-pairs and given by [18]

$$A \propto Q = C_{\text{cell}} \cdot (V_{\text{Bias}} - V_{\text{B}}) = C_{\text{cell}} \cdot V_{\text{OV}}. \tag{4.12}$$

Here C_{cell} is the capacitance of the diode, V_{OV} the voltage the diode is biased (with V_{Bias}) above its breakdown voltage V_{B}, and A the amplitude of the signal. V_{OV} is referred to as the over-voltage.

4.4 Silicon Photomultipliers

To restore the proportionality of the output signal to the primary photon flux one GAPD is insufficient. A silicon photomultiplier is created by connecting many small GAPDs with their individual quenching resistors in parallel on a single wafer. A microscope picture of one of the SiPM types characterised in this thesis shown in figure 4.8 and a schematic shown in figure 4.9 illustrate the basic SiPM structure. Usually the individual GAPDs of an SiPM are referred to as cell or pixel, here the

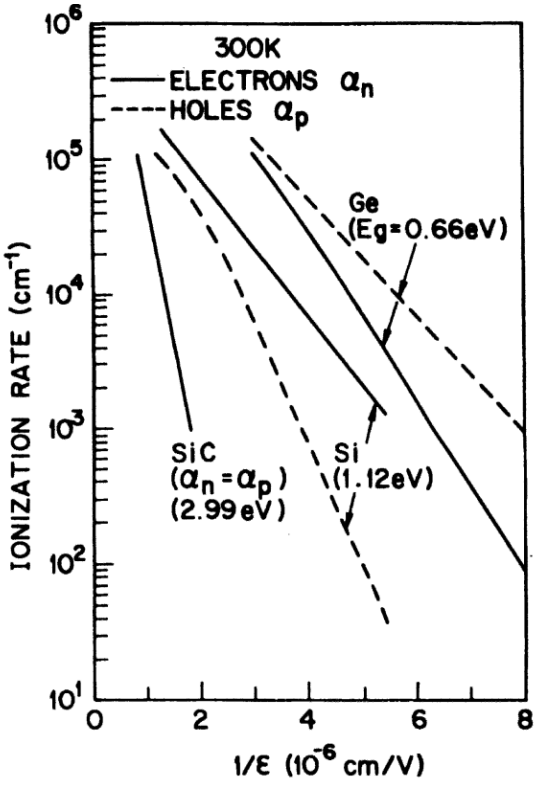

Figure 4.5: Measured ionisation coefficients of electrons and holes in silicon, germanium and SiC. Taken from [15].

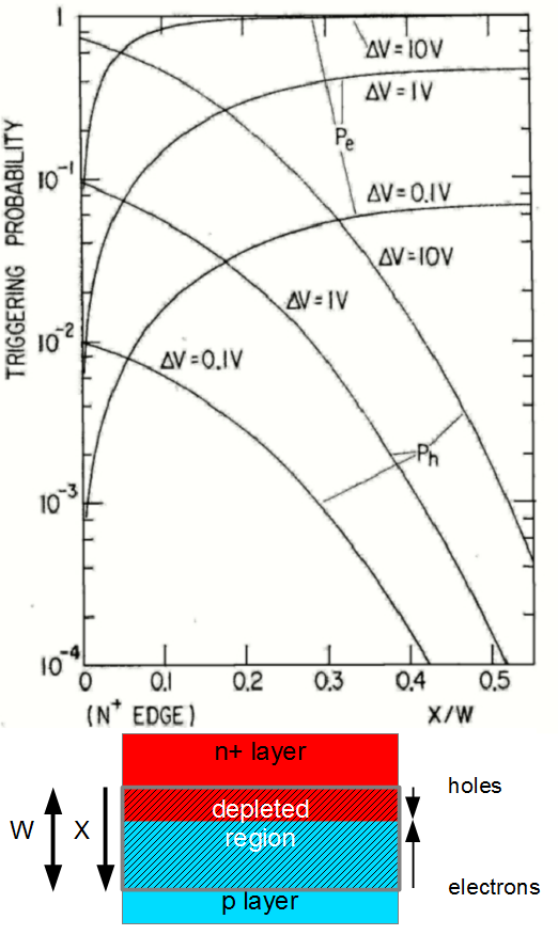

Figure 4.6: Above) Avalanche trigger probability of electrons P_e and holes P_h in a silicon n^+-p junction for different positions of carrier generation and overvoltages ΔV. The position in the deletion layer is given by X and the width of the depletion layer by W. Taken from [19]. Below) Explanation of the coordinate system and drift direction of electrons and holes.

term cell is used. Because the cells are read out over a common resistor and are connected in parallel, the signal of n firing, fully charged cells is given by n-times the single cell signal as given by equation (4.12). A typical example of (amplified) SiPM signals is shown in figure 5.3 on page 35. One can see a quick rise of the signal from the avalanche and a slow return to baseline caused by the recharge of the fired cell(s). The different bands in the image correspond to a different number of fired cells and are clearly separated. Hence SiPMs are also referred to as 'photon counting devices'.

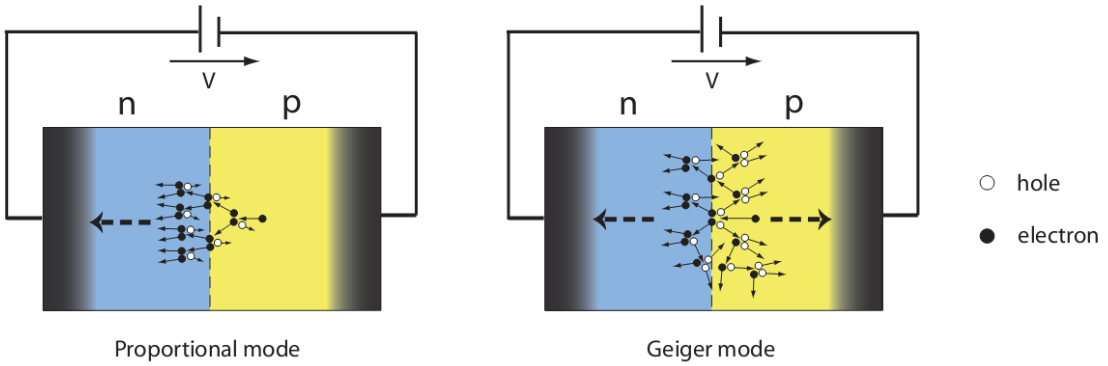

Figure 4.7: Avalanche development in proportional (left) and in Geiger-mode (right). In proportional mode the APD is biased below breakdown and the avalanche develops only into one direction and ends intrinsically. In Geiger-mode the avalanche diverges and needs to be quenched externally. Taken from [20].

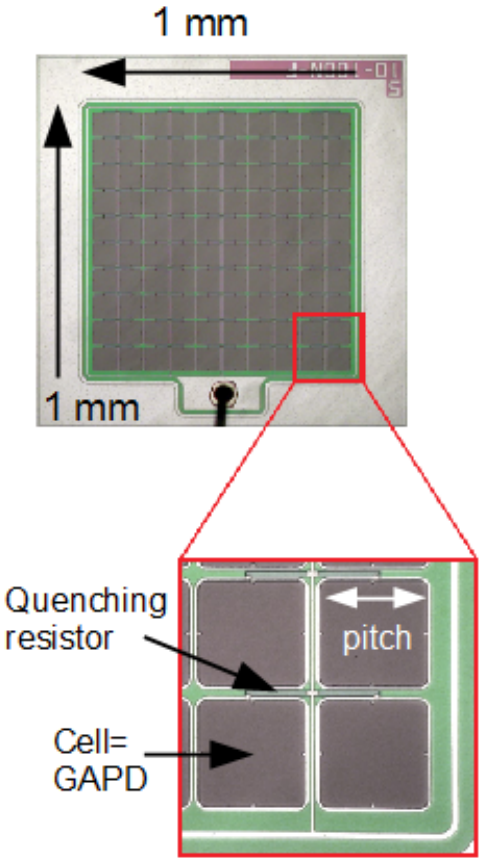

Figure 4.8: Microscope image of an SiPM with 100 cells. ($1\text{x}1\,\text{mm}^2, 100$ µm cell pitch). Taken from [21].

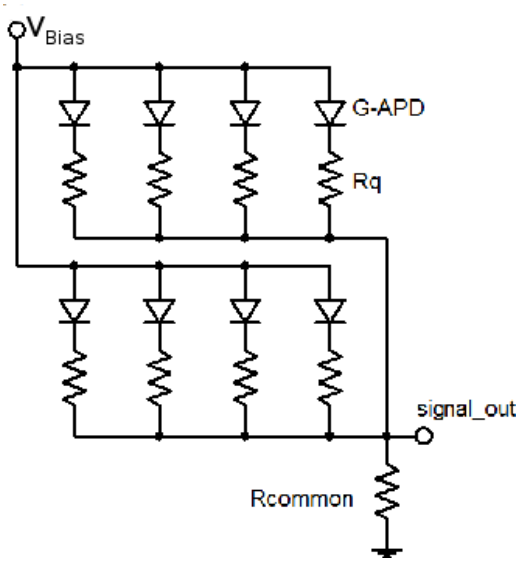

Figure 4.9: Basic layout of an SiPM. Many GAPDs and their quenching resistors Rq are connected in series and read out via a common load Rcommon.

With this arrangement the proportionality of the signal to the photon flux is restored as long as the flux is small in comparison to the number of cells.

4.4.1 Properties

In the following an (incomplete) overview of typical SiPM properties, advantages and possible challenges arising from their usage is given.

Dimensions

Of the SiPMs, which are currently commercially available, active detection areas range from 1x1 to 3x3 mm^2 . The usual cell pitch sizes range from 25 to 100 µm. Also available are arrays of individual SiPMs, which minimize the dead space between the individual SiPMs [22],[23].

Dark Rate

An SiPM cell cannot only fire due to the detection of light, i.e. an eh-pair generated by an absorbed photon, but also due to electron hole pairs generated by thermal excitation. Because of this, SiPMs have a relatively high dark count rate from a few hundred kHz to one MHz per mm^2 of active detection area at room temperature. The thermal generation rate of eh-pairs is expected to be an exponential function of the temperature and to be reduced by a factor 2 for every 8 °C drop in temperature [18].
In addition to the random thermal noise SiPMs also possess two forms of correlated noise, one instantaneous and one delayed, where the firing of one cell can cause other cell(s) to fire. Because this correlated noise may have a negative impact on the photon counting resolution, a detailed measurement of this phenomenon has been performed in this thesis, which, together with a more detailed introduction, can be found in chapter 7.

Both the thermal and the correlated noise contribute to the dark count rate. This rate has been measured explicitly as a function of the temperature and the results can be found in [24].

Temperature Dependence of the Breakdown Voltage

In addition to the dependence of the dark count rate on the temperature, also the breakdown voltage depends on the temperature. At a constant bias voltage this influences the over-voltage, which is the voltage, usually only a few volts, the SiPM is operated above the breakdown voltage. Because nearly all important SiPM properties, e.g. the gain and the PDE, strongly depend on the over-voltage an understanding of this change with temperature and a way to keep the over-voltage constant is required. For this, the dependence of the breakdown voltage on the temperature has been measured and a method of automatically keeping the over-voltage constant has been explored. This is described in chapter 6.

Photon Detection Efficiency

The key characteristic, determining whether SiPMs are suitable for the detection of fluorescence light is their photon detection efficiency (PDE). Manufacturer specifications reach up to 74%, however these values are, according to the manufacturer, overestimated due to the effects of correlated noise mentioned previously [22]. A measurement of the PDE without these effects has been performed for this thesis, and the results can be found in chapter 8.

Dynamic Range

As mentioned previously, a linear response of the SiPM signal is only to be expected for a number of photons, which is much smaller than the number of cells. If this is not the case, the signal saturates. An approximation of the signal A as the response to N_p simultaneously incoming photons is given by

$$A \approx N_{\text{firedcells}} = N_{\text{total}} \cdot \left(1 - e^{-\frac{\text{PDE} \cdot N_p}{N_{\text{total}}}}\right). \tag{4.13}$$

Here $N_{\text{firedcells}}$ is the number of fired cells, PDE the photon detection efficiency and N_{total} the total number of fired cells [18].

Recovery Time

After one discharge, a cell needs time to recharge. If the cell fires again before it is fully recharged, the produced signal will be of reduced amplitude. The recovery behaviour of SiPMs was studied in [25]. An exponential recovery behaviour was observed with recovery time constants in the order of a few tens of nanoseconds.

4.4.1.1 Miscellaneous Advantages

Other advantages, commonly associated with the usage of SiPMs are their insensitivity to magnetic fields (in contrast to PMTs), their low bias voltages (in the order of tens of volts instead of kV for PMTs), their robustness and potential of low-cost mass-production [18].

4.4.2 Characterised SiPMs

In total four different SiPM types are characterised in this thesis. All four types were manufactured by Hamamatsu Photonics and were selected because they represent the UV/blue sensitive SiPMs with the highest fill factor and consequently have the potential for a high PDE, which are currently commercially available. The tested types are from the S10362 series, and come in two different cell pitch sizes, each with two different active areas. The largest available pitch size is 100 µm, with a fill factor of 78.5% [22]. The next largest available fill factor is 50 µm, with a fill factor of 61.5 % [22]. Both pitch sizes have two variants with different active areas, one with 1x1 mm^2 and the other with 3x3 mm^2. An image of two SiPMs with a different active area is shown in figure 4.10, and listed in table 4.1 is a summary of the key characteristics of all tested SiPMs as given by the manufacturer.

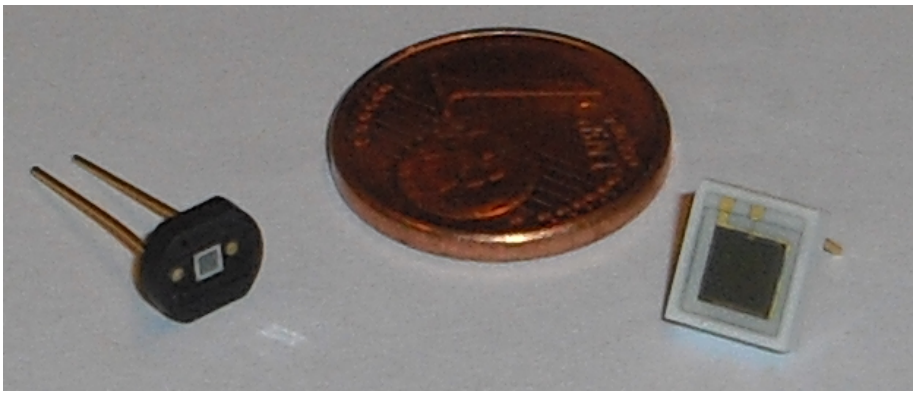

Figure 4.10: Image of characterised SiPMs. On the left is the 1x1 mm^2, and on the right the 3x3 mm^2 type.

Table 4.1: SiPM specifications of the manufacturer for the characterised types [22]. Values are for a temperature of 25 °C, and the manufacturer (Hamamatsu Photonics) recommended bias voltage at this temperature. PDE includes effects of crosstalk and after-pulsing

Type: S10362	-11-100C	-33-100C	-11-050C	-33-050C
Active area	1x1 mm^2	3x3 mm^2	1x1 mm^2	3x3 mm^2
Fill factor	78.5 %	78.5 %	61.5 %	61.5 %
Cell size	100x100 μm^2	100x100 μm^2	50x50 μm^2	50x50 μm^2
Peak sensitivity at	440 nm	440 nm	440 nm	440 nm
PDE at peak sens.	65%	n.a.	50%	n.a.
Bias voltage range	70± 10 V	70± 10 V	70± 10 V	70± 10 V
Typ. dark count rate	0.6 Mhz	8.0 Mhz	0.4 Mhz	6.0 Mhz
Gain	$2.4{\cdot}10^6$	$2.4{\cdot}10^6$	$7.5{\cdot}10^5$	$7.5{\cdot}10^5$
Cells	100	900	400	3600

As can be seen, the dark noise rate is smaller for a smaller pitch size at the same nominal area. This may be understood by the smaller active area[4]. The recommended bias voltage describes only the general bias voltage range. The concrete recommended bias voltage varies up to one to two volts between different SiPMs, because the breakdown voltage varies from SiPM to SiPM. All types have the highest PDE at the same wavelength of 440 nm. The highest quoted PDE is 65% at this wavelength. This however, includes effects of crosstalk and after-pulsing. A measurement without these effects has been performed and can be found in chapter 8.

[4]Caused by the difference in the fill factors.

5. Cooling Chamber Measurement Setup and Basic Results

This chapter aims to give an introduction to one of the two used measurement setups in this thesis and to give a basic overview about what data is collected from the SiPMs for later analysis and how. More specifically, the measurement setup common to the following two chapters (chapters 6 and 7) is described. In the measurements described there, the SiPMs are located inside a cooling chamber, allowing to take measurements over a long period of time under a stable and adjustable temperature. Two main measurement instruments are used to collected the data from the SiPM. The first instrument is a charge-to-digital converter (QDC) which integrates the charge, originated by the firing of one or more SiPM cells. This provides information whether any SiPMs have fired during the integration time and how many cells have fired. A flash analog-to-digital-converter (FADC) is used to collect traces of SiPM signals, allowing for a time-resolved information about the firing of the SiPM cells.

5.1 Measurement Setup

The analysis method used in the study of the correlated noise in chapter 7 requires that no light reaches the SiPM. Hence all measurements in the next two chapters are carried out with the SiPMs located in darkness and with the measured SiPM signals being due to thermal and resulting correlated noise. A schematic of the base setup is shown in figure 5.1. The SiPM is connected to the amplifier board and both are put inside a light-tight box inside the cooling chamber. The amplifier board is connected to two power sources, one[1] providing the $\pm 5\,\mathrm{V}$ operating voltage for the amplifier and the other[2] the bias voltage for the SiPM.
The signal is first multiplied by a linear fan-in/fan-out[3] and fed into a QDC[4], a constant-fraction-discriminator[5] (CFD) which serves as the gate generator for the QDC, and into a FADC[6]. The CFD, QDC and FADC are connected to the internal VMEbus of the crate. Access to this bus is provided by a Wiener VM-USB module [29].
The measurement is controlled by a self written C++ program (together with the

[1] Lambda ZUP-10-20
[2] Keithley Sourcemeter 2400, [26]
[3] Phillips Scientific 744
[4] CAEN V965, [27]
[5] CAEN V812
[6] CAEN V1729, [28]

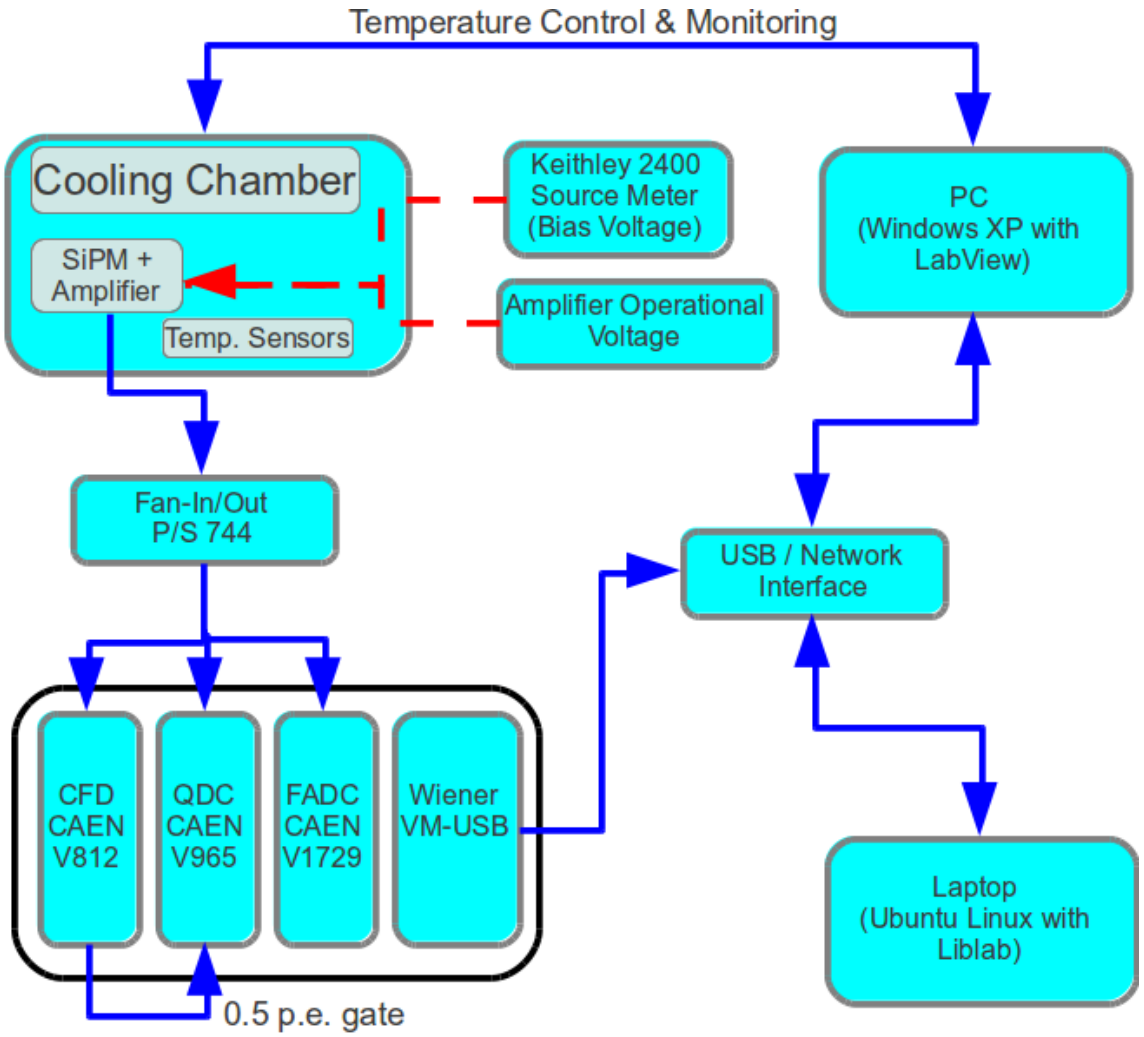

Figure 5.1: Experimental setup. Data and signal cables are marked in blue (solid), power supply cables in red (dashed). CFD, QDC and FADC are connected to the internal VMEbus of the crate which is accessible via the VM-USB module. See text for details.

work in [24]). The device library 'LibLAB' [30] is used to access and control all measurement devices with the exception of the cooling chamber. In the following part the relevant measurement components are described in detail.

Cooling Chamber

Originally the cooling chamber 'COOLI' was developed in the course of a diploma thesis at III. Phys. Inst. B, RWTH Aachen University with the purpose of testing silicon strip detector modules for the CMS-detector [31]. The chamber is essentially a temperature isolated box with Peltier-elements at the top and the bottom, either heating or cooling the inside, with the excess heat being dissipated to the local cooling water system. Two sensors are located within the chamber, monitoring the

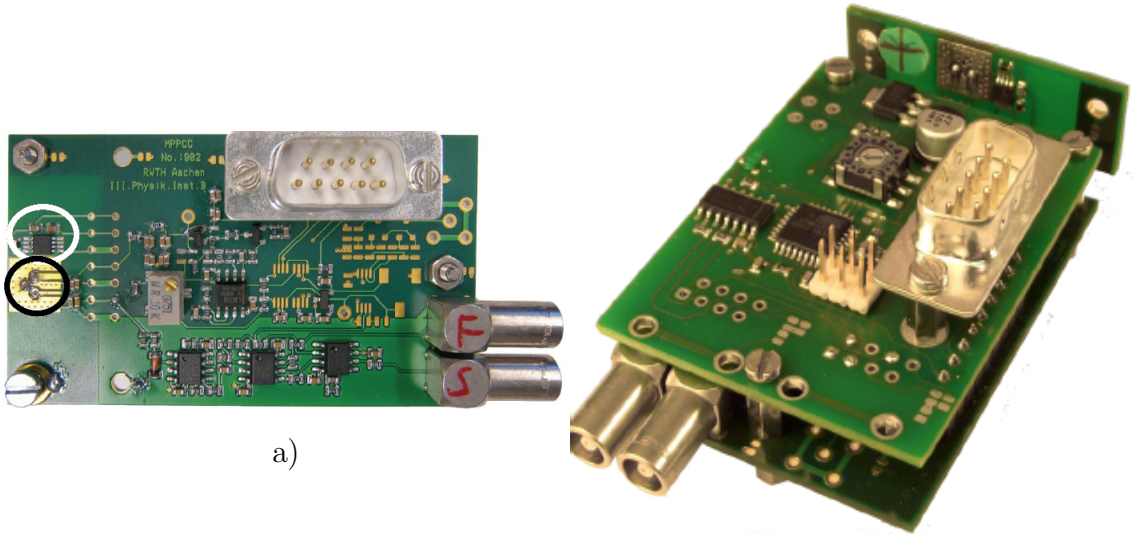

a) b)

Figure 5.2: Used amplifier boards designed by F. Beißel et al. Both a) and b) have the same base board, b) is extended by an additional board with a micro-controller on top of the first. The micro-controlled version allows for remote operation/monitoring of the bias voltage and temperature as well as automatic adjustment of the bias voltage to compensate temperature changes.
a) White (upper) circle: Temperature sensor, black (lower) circle: SiPM connector

temperature and also the humidity and are connected to the One-Wire bus of the chamber, as is the temperature sensor of the amplifier board. The chamber can be monitored and controlled via a LabView[7] program. It allows to set a certain temperature and the chamber then automatically cools down/heats up until the desired temperature is reached. Once the temperature has settled it can usually be held constant within $0.2 - 0.5\,°C$. The maximum temperature of the chamber is around $30\,°C$. The lower reachable limit depends on the humidity and surrounding temperature. Below approximately $0\,°C$ the humidity rises sharply and the chamber takes increasingly longer to reach a desired temperature and the temperature is not kept as stable over a longer period of time as it is at higher temperatures. Therefore temperatures below $0\,°C$ are only used if necessary.
Via a TCP/UDP interface of the LabView program the chamber can also be controlled remotely.

Amplifier Board

The used, charge sensitive, transimpedance amplifier board was designed and manufactured at III. Phys. Inst. B, RWTH Aachen University by F. Beißel et al. As the design is continuously extended, different versions of the amplifier exist. The

[7] National Instruments, http://sine.ni.com/

two used boards are shown in figure 5.2. The board shown in sub-figure a) has two outputs, one integrating, intended for energy, and one non-integrating, fast output intended for timing measurements. For all subsequent measurements the fast output, with a transimpedance of approximately 2.94 V/mA [32] is used. The board also has an integrated temperature sensor[8], placed next to the SiPM connection point. The sensor has a resolution of 0.06 °C and a stated absolute accuracy of 0.5 °C. An absolute temperature calibration, for the particular used board, has been performed in [24] and the correction

$$T_{Real} = T_{\text{Board}} - (2.52 \pm 0.5)\,^{\circ}\text{C} \tag{5.1}$$

is applied to all temperature readings in chapters 6 and 7. Normally the board has a potentiometer to control the exact SiPM bias voltage. For purposes of automated measurement this has been bridged and the voltage supplied by the Source Meter is the same as the bias voltage. An example of an SiPM signal amplified with this board can be seen in figure 5.3.

The board shown in figure 5.2 b) features the same base board as a). However the base board is extended by an additional board with an integrated micro-controller fixed on top of the first. With this modification the board is accessible over USB (integrated in the Sub-D plug) and the current temperature can be read, as well as the bias voltage read and set. The resolution for reading/setting the bias voltage is 5 mV [32]. The board can also automatically adjust the bias voltage to compensate for temperature changes. For this the micro-controller requires the progression coefficient β from equation (6.2) and a reference bias voltage. The board used in this thesis can set the progression coefficient as a multiple of 20 mV/K with newer versions decreasing this to 5 mV/K [32].
Unless otherwise specified, the version without the micro-controller is used in the following two chapters and the other version is used in chapter 8.

Keithley Source Meter 2400

The Keithley Source Meter is used to provide the bias voltage to the SiPM and is controlled remotely via its RS-232 interface. Within the used measurement range of 200 V the voltage can be set with a resolution of 5 mV and an accuracy of $\pm(0.02\%\ \text{rdg.}[9] + 24\,\text{mV})$. The applied voltage can be measured with a resolution of 1 mV and an accuracy of $\pm(0.015\%\ \text{rdg.} + 10\,\text{mV})$ [26].

QDC: CAEN V965

The CAEN V965 is a 16 channel, dual range charge-to-digital converter with current integrating negative inputs. Usually the measurement is controlled via an external gate (see figure 5.3). When the gate, which should precede the SiPM signal by 15 ns is open, the QDC integrates the charge on all channels separately by charging one

[8] Maxim DS18B20, [33]
[9] Percentage of reading (measured value).

capacitor per channel. Afterwards the signal is converted to a voltage which in turn is digitized in parallel by two analog to digital converters (ADCs). One ADC is preceded by a x8 gain stage, allowing for a measurement range from 0 to 100 pC with a resolution of 25 fC, while the other ADC stage is preceded by a x1 gain stage, allowing for a measurement range from 0 to 800 pC with a resolution of 200 fC [27].

As the amplified, deposited charge by the firing from one cell of the SiPM is usually in the order of a few tens of pC the broader measurement range with the lower resolution is used. Since the signal applied to the QDC must not exceed +15 mV, the SiPM signal is never feed directly into the QDC, but only after a linear fan-in/fan-out with a negative offset of $50 - 200$ mV applied to the signal. An example of a charge spectrum measured with the QDC is shown in figure 5.5.

FADC: CAEN V1729

The CAEN V1729 is a 4 channel FADC. It has a bandwidth of 300 MHz and a measurement range from -0.5 V to 0.5 V with a 12 bit resolution, equivalent to a resolution of 250 µV. Internally the FADC has an analog, circular memory of 2560 samples per channel of which 2520 are valid after reconstruction of the stored trace. Sampling can be performed with either 1 GHz or 2 GHz, resulting in a trace length of either 2520 ns or 1260 ns [28].
For all measurements in this thesis the 1 GHz sampling mode was used as it is sufficient for the amplified signal and collects longer traces, which is important for chapter 7.

Upon arrival of a trigger signal the continuous overwriting of the memory is stopped and the signal is digitized and reassembled. Unfortunately the FADC possesses a bug which causes the trace to be reassembled incorrectly, with the actual starting point randomly distributed in the reconstructed trace. A workaround for this was found. With the workaround the actual start of the trace is placed to a defined point at the end of the spectrum, provided the internal random trigger is used, shortening the usable trace length to 2300 ns. Because of this all FADC measurements in this thesis are randomly triggered.

LibLAB

Besides the control of the cooling chamber all other remotely controlled devices are accessed through their individual modules in the device library 'LibLAB'. The LibLAB library is developed locally at III. Phys. Inst. A and III. Phys. Inst. B, and aims to provide access to common laboratory hardware through a common, object-oriented C++ interface [30].

5.2 Measurement Procedure

Before the actual measurement cycle (see figure 5.4) can begin, some prerequisite measurements have to be performed. First the SiPM and the amplifier board are put inside the cooling chamber and the desired temperature is set to 25 °C where the

recommended bias voltage of the manufacturer is valid. After the temperature has been reached, a suitable bias voltage range around the recommended bias voltage is selected for scanning in the following measurements. The lower limit is set in a way, so that the SiPM signal is clearly distinguishable from the amplifier noise. The upper end of the bias voltage range is set just below the bias voltage at which the SiPM behaviour becomes erratic[10]. For the 100 µm cell pitch types this usually translates to an over-voltage range of $0.5 - 1.8\,\mathrm{V}$ and for the 50 µm types to a range of $0.9 - 2.6\,\mathrm{V}$.

After the range has been selected, the current breakdown voltage of the SiPM is roughly measured by using two bias voltages U_1 and U_2, where the amplitude of the signal of one firing cell (also referred to as the 1 photo electron (1 p.e.) signal), relative to the baseline, is of double amplitude at U_2 than at U_1. From this the breakdown voltage is given by (compare equation (4.12) on page 23))

$$V_\mathrm{B} = 2 \cdot U_1 - U_2. \tag{5.2}$$

With this knowledge, it is possible to measure one reference amplitude of the 1 p.e. signal A_ref at a now known reference over-voltage $V_\mathrm{OV\text{-}ref}$. From this the amplitude A_1 of the 1 p.e. signal can be calculated for any over-voltage (see equation (4.12)) with

$$A_1 = A_\mathrm{ref} \cdot \frac{V_\mathrm{OV\text{-}1}}{V_\mathrm{OV\text{-}ref}}. \tag{5.3}$$

Using this the CFD threshold can be set to a level corresponding to half of the 1 p.e. signal at each new bias voltage during the automated measurement.
The SiPM signal with the QDC gate from the CFD is shown in figure 5.3. The gate is chosen as small as possible with 15 ns required start-up time for the QDC before the actual signal and 15 ns of signal capture. These last 15 ns already catch a large amount[11] of the SiPM signal but the probability of the signal being contaminated by the firing of another cell (by thermal noise) or an after-pulse from the same cell is drastically reduced. This should provide a clean signal for the gain measurement of the next chapter as well as for the crosstalk measurement described in chapter 7.

With the choice of the bias voltage range at a known temperature and the measurement of a reference 1 p.e. amplitude, the automated measurement to determine the temperature dependence (see figure 5.4 for a flowchart) can start with the following measurement cycle:

For each new temperature the new bias voltage range is calculated using the progression factor β from equation (6.2). If the individual SiPM has not been characterised before, the manufactures reference value of $\beta = 56\,\mathrm{mV/K}$ [22] is used, otherwise the

[10] Continuous self-firing, overshooting of the amplifier baseline due the high signal rate (issue of the amplifier, not of the SiPM). This leads to a distortion of the pedestal and making QDC spectra hard/impossible to analyse due to the partial/complete overlap of the peaks in the spectrum

[11] Roughly half of the SiPM signal.

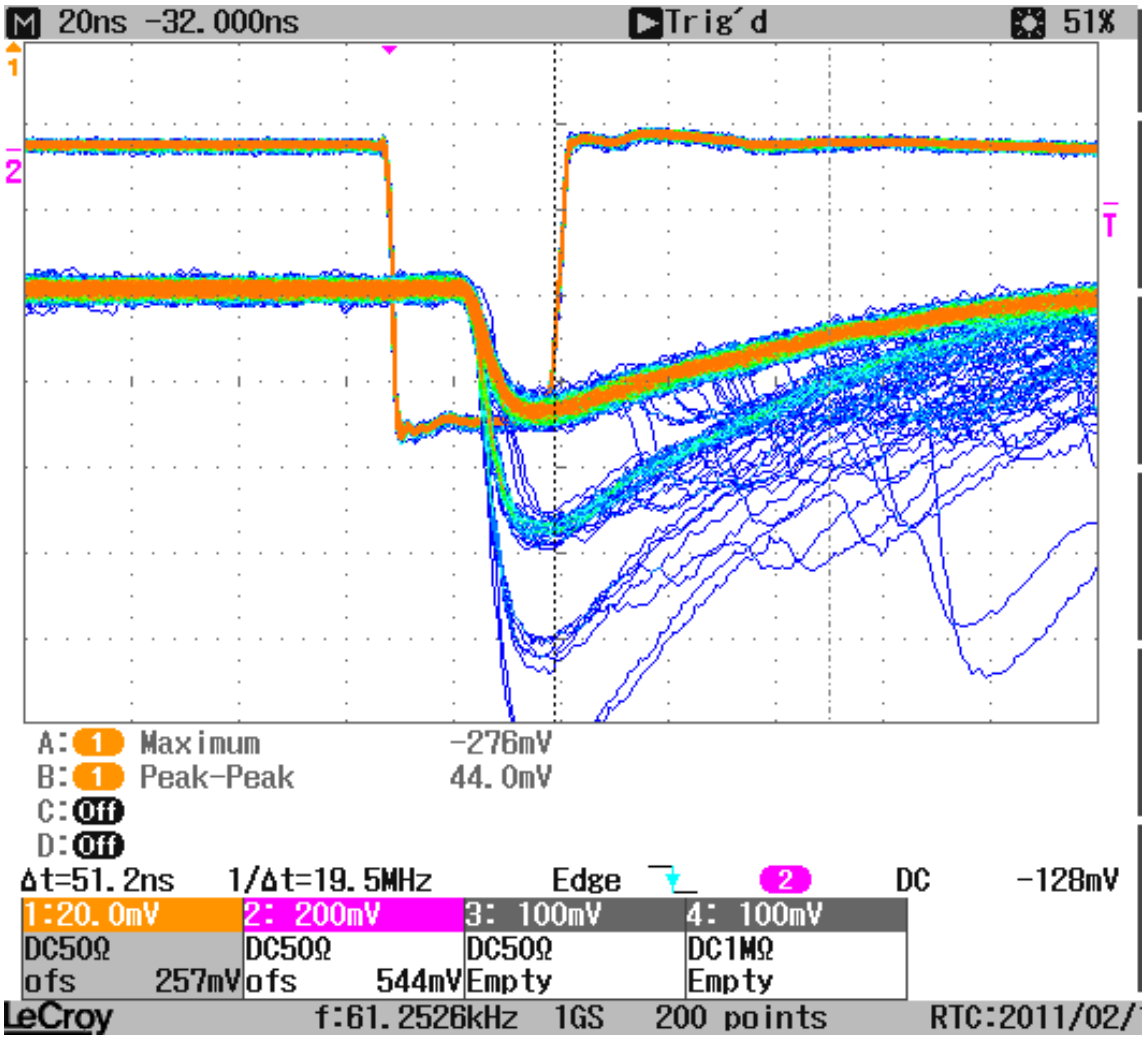

Figure 5.3: Amplified SiPM (1x1 mm^2, 100 µm cell pitch) signal (channel 1) in darkness and CFD signal which gates the QDC (channel 2). The short gate provides resistance to contamination by additional thermal noise and/or after-pulses. Horizontal axis: time (1 division $\doteq$ 20 ns), vertical axis: voltage (1 division $\doteq$ 20 or 200 mV).

measured value is chosen. With the new bias voltage range calculated, the measurements for each bias voltage are performed. First the current 1 p.e. signal amplitude is calculated from equation (5.3) and the CFD threshold set to half of this amplitude. Since the used CFD corrects for a possible DC-offset, only the signal amplitude is required and no correction has to be made to account for the non-zero baseline of the SiPM signal.
Afterwards 100,000 QDC values are measured and 100,000 FADC traces (only used in chapter 7) are acquired and the information is saved in ROOT [34] files. The QDC measurement is performed relatively quickly, lasting about five minutes, while the FADC measurement takes one to two hours. During the measurement the temperature from the temperature sensor on the SiPM amplifier board, as well as the applied

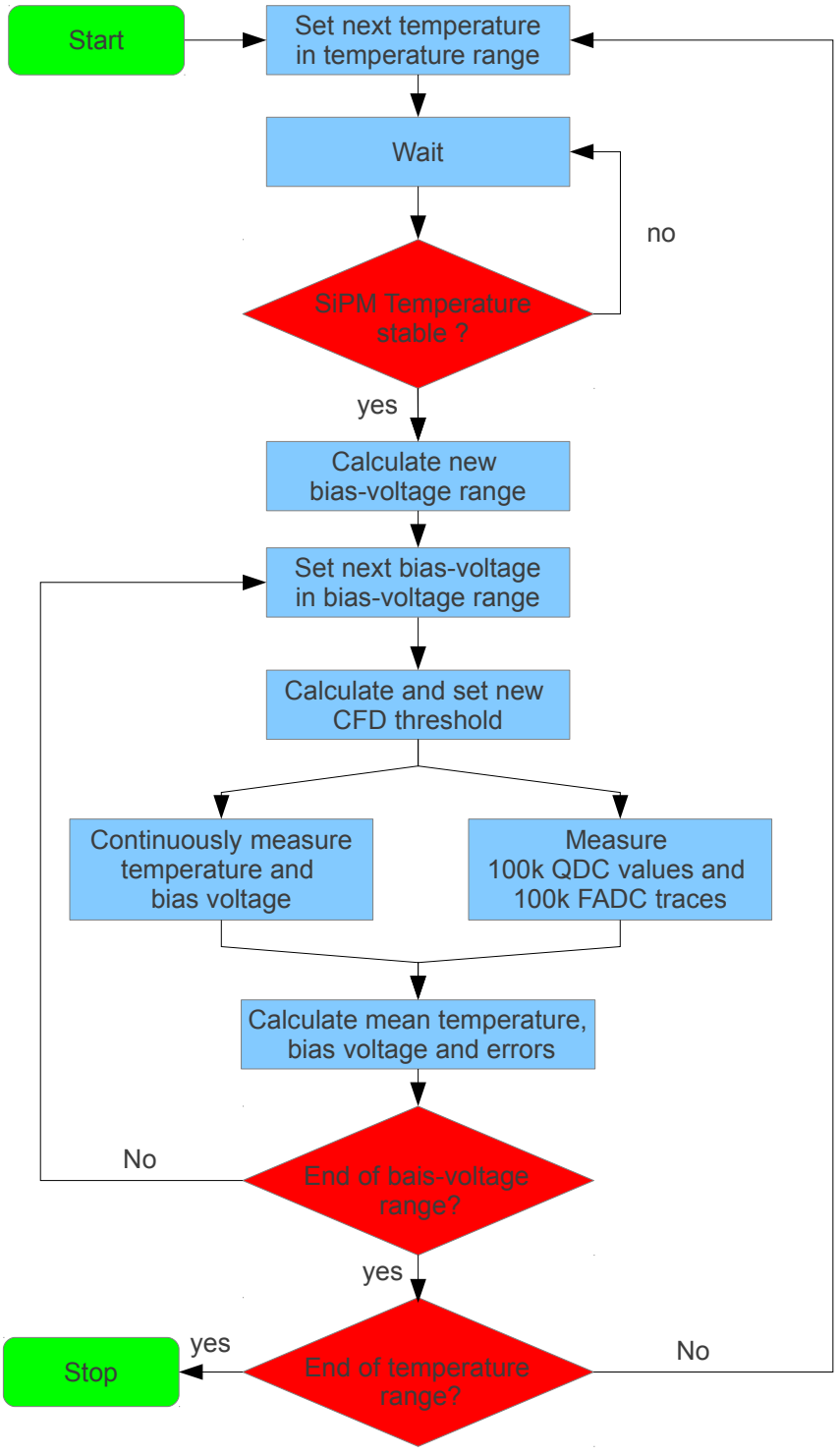

Figure 5.4: General flowchart of SiPM measurements in cooling-chamber.

bias voltage are measured and at the end, their mean values and corresponding uncertainties are calculated and the information appended to the output file. When the bias voltage range is exhausted a new temperature is set and, after the new temperature is reached and stable, the cycle is repeated until all temperatures are completed.

With these settings a measurement at a given temperature takes about two hours to complete, including the cooling down or warming up.

5.3 Basic Measurement Results

An example of a SiPM charge distribution, collected by the QDC is shown in figure 5.5. As demonstrated by the oscilloscope image shown in figure 5.3 the signals from the firing of a different number of cells are well separated. This directly translates into the 'finger-like' peak structure in the charge distribution in figure 5.5. Because the measurement was triggered by the firing of at least one cell, the first peak corresponds to the firing from one cell, the second to the firing of two cells and so on. Since the measurement was performed in darkness, with the measurement interval being small in comparison the the dark noise rate, the one cell peak or 1 p.e. peak is the dominant peak in the spectrum. The other peaks are either due to (rare) thermal coincidences or correlated noise from the original thermal noise pulses. More detail on this can be found in chapter 7.
The distance between the peaks is proportional to the gain, which in turn depends on the over-voltage. This fact is used to determine the dependence of the breakdown voltage on the temperature in the next chapter. The information collected by the QDC already allows the determination of how often a given number of cells have fired during the measurement interval.
A time-resolved information however is not available from the QDC. This information is provided by the FADC traces. An example of such a trace is shown in figure 5.6. Again, the trace shown in this figure was recorded in darkness. The second peak, which has roughly double the amplitude of the other peaks is due to the simultaneous firing of two cells. This is very likely due to optical crosstalk which is the instantaneous component of the correlated noise. Also observable is that some signals seem to follow shortly after a previous pulse. This may be due to the random thermal noise or due to the delayed component of the correlated noise, namely after-pulsing. More detail on this and a measurement of the probabilities of optical crosstalk and after-pulsing can be found in chapter 7.

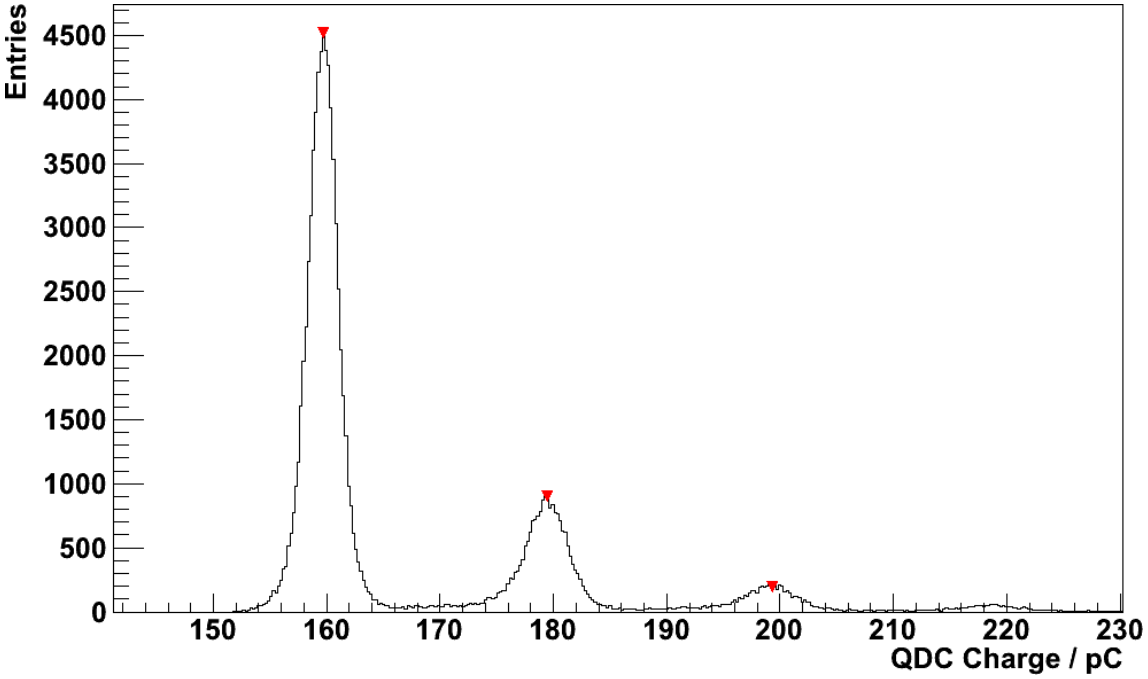

Figure 5.5: Example of a charge spectrum of amplified SiPM signals. The SiPM is located in darkness and within the cooling chamber. The QDC trigger threshold is set to the 0.5 p.e. level. Because of this, the first peak corresponds to one firing cell i.e. this spectrum contains no pedestal.

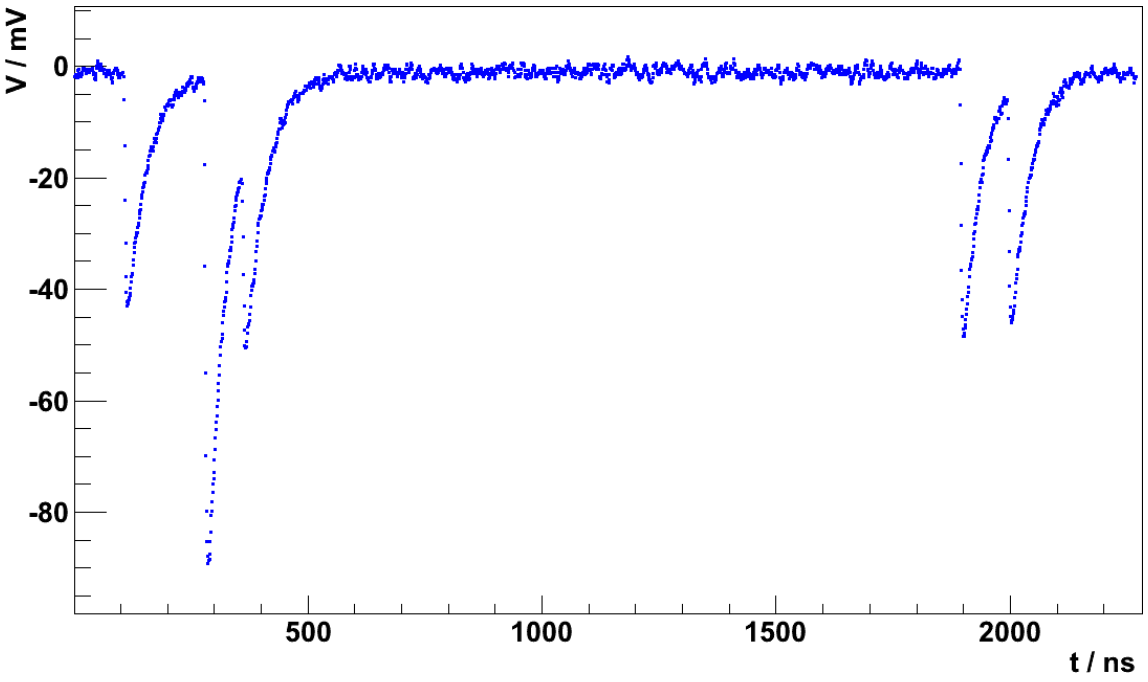

Figure 5.6: Example of a measured FADC trace with multiple SiPM events.

6. Temperature dependence of the breakdown voltage

For the characterisations in the next chapters as well as for practical applications it is necessary to understand how to operate the SiPMs in a stable way. The challenge arising here is that the breakdown voltage V_B of the SiPM is depends on the temperature and is expected to rise with the temperature [35].
Since the over-voltage V_{OV} is given by (V_{Bias} -V_B), the over-voltage changes with the temperature as well, as long as the bias voltage V_{Bias} is not adjusted accordingly.

As the over-voltage is usually in the range of a few volts for the studied types (see section 5.2) and as many SiPM characteristics, e.g. the gain, the thermal noise rate, and the photon detection efficiency (PDE), have a strong dependence on the over-voltage, even small absolute changes in the over-voltage can result in large relative changes in SiPM operation and therefore the over-voltage has to be kept constant in many applications.

One possible way to achieve this would be to keep the temperature of the SiPM constant, however this may not be preferable or possible in many applications.

This results in a need to adjust the bias voltage to compensate changes in the breakdown voltage if the temperature is not stable during the operation of the SiPM. The aim of this chapter is, first, to measure how the breakdown voltage changes with temperature and second, to test a method of automated adjustment of the bias voltage, integrated in the used amplifier board.

6.1 Theoretical Background

As stated previously, the breakdown voltage of an SiPM is not stable but is expected to increase with a rise in the temperature.
This can be qualitatively understood by considering that, under high field conditions, the charge carriers passing through the depletion layer start losing part of their energy to optical phonons via scattering [16]. As the phonon occupation increases with temperature, the carriers lose more energy to the crystal lattice along a given distance. This means, that a higher bias voltage has to be applied for the charge carriers to gain enough energy to create and sustain an avalanche.
The breakdown voltage is expected to be linearly dependent on the temperature [36] and can be expressed as

$$V_B = V_{B0} \left[1 + \beta' \left(T - T_0\right)\right]. \tag{6.1}$$

Here V_{B0} is the breakdown voltage at a reference temperature T_0 and β' is the linear growth constant. Equation (6.1) can be rewritten as

$$V_B = V_B(T = 0°C) + \beta \cdot T \tag{6.2}$$

$V_B(T = 0°C)$ is the breakdown voltage at 0 °C and β now directly expresses the change in the over-voltage with the temperature.
The Celsius scale is chosen for convenience and illustration reasons, however the progression factor β is still expressed in units of mV/K.

6.2 Measurement of the Temperature Dependence

6.2.1 Measurement Principle

Using a cooling-chamber the breakdown voltage of the SiPM can be measured over a wide temperature range, and the progression factor β can then be extracted from the data. The breakdown voltage of a specific temperature can be determined by measuring the gain[1] of the SiPM for a number of different bias voltages using a charge-to-digital converter (QDC). Since the gain is proportional to the over-voltage (see equation (4.12)) the breakdown voltage can be determined by extrapolating the gain, as a function of the bias voltage, down to zero.

6.2.1.1 Measurement Setup and Procedure

The general measurement setup and procedure are described in chapter 5 (the previous chapter). In contrast to the general measurement procedure laid out there, only a QDC measurement is performed and no FADC traces are collected, as they are not needed for the analysis in this chapter and this speeds up the measurement process.

6.3 Analysis

6.3.1 Determination of the Gain from the QDC Data

The first step in the analysis is the determination of the deposited charge per fired cell ΔQ/cell for a given over-voltage from the measured QDC spectra. A typical example of such a spectrum can be seen in figure 6.1. The plotting of the histogram and the fit have been performed with the data analysis framework 'ROOT' [34] which is used throughout this thesis for these purposes. As the QDC measurement was triggered with the CFD threshold set to 0.5 p.e. signal level, the first peak in the spectrum corresponds to the amplified charge deposited in the QDC by one firing cell plus an offset due to the non-zero baseline of the SiPM signal and the internal pedestal current of the QDC. The second peak corresponds to two cells firing during the gate and so on. Since the measurement was conducted in a light-tight box it

[1] Or rather the charge ΔQ generated by one cell firing which is related to the gain G by $G = \frac{\Delta Q}{e}$ where e is the elementary charge

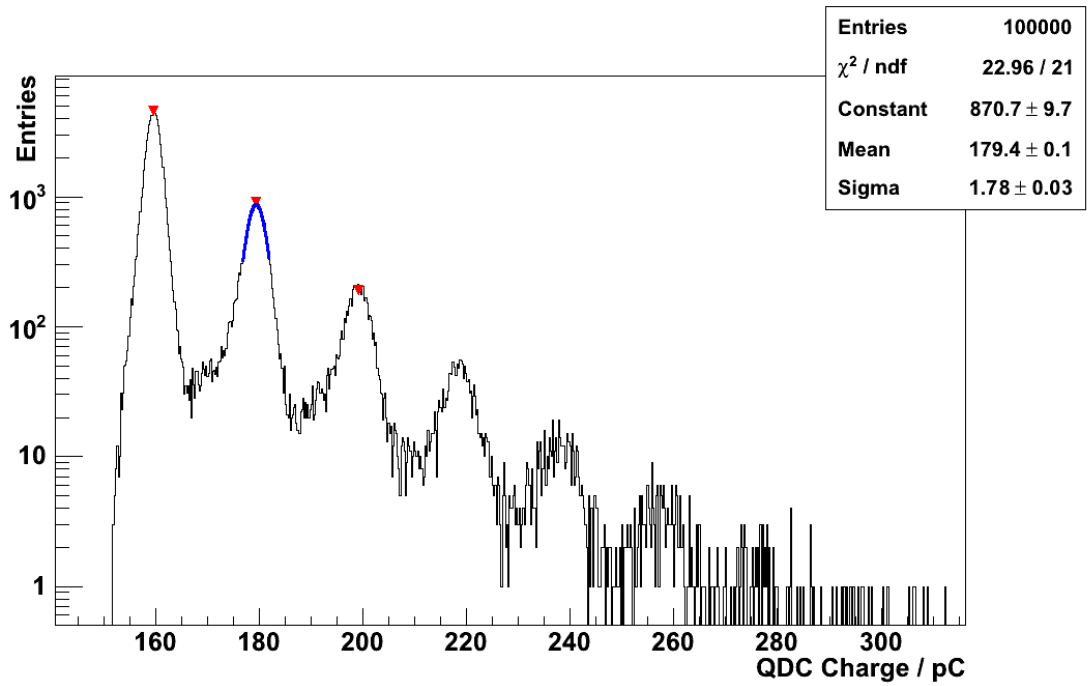

Figure 6.1: Charge spectrum of amplified SiPM signals. The SiPM is located in darkness and within the cooling chamber. The QDC trigger threshold is set to the 0.5 p.e. level. Because of this, the first peak corresponds to one firing cell i.e. this spectrum contains no pedestal. Blue: Gaussian fit applied to the 2nd (two cells firing simultaneously) peak to determine the peak position.
($1\text{x}1\,\text{mm}^2, 100\ \mu\text{m}$ cell pitch, T = $(25.14 \pm 0.03(\text{stat.}) \pm 0.50(\text{sys.}))°$ C,
$V_{\text{Bias}} = (71.21 \pm 0.02(\text{sys.}))$ V))

may seem unintuitive at first, that the firing of up to six cells happens in the 30 ns gate. This effect is due to optical crosstalk, which is covered in the next chapter.
The mean distance between two neighbouring peaks $Q_{\text{i+1}}$ and Q_{i} corresponds to the deposited charge per fired cell and the first two peaks are used to calculate this charge with

$$\Delta Q/\text{cell} = Q_2 - Q_1, \tag{6.3}$$

where the individual peak position was determined by the fit of a Gaussian to the upper half of the peak. The uncertainty σ_{Qi} of this position is given by

$$\sigma_{Qi} = \sigma_{\text{fit}} \oplus \frac{R_{\text{QDC}}}{\sqrt{12}}, \tag{6.4}$$

with σ_{fit} is the uncertainty of the χ^2-fit and R_{QDC} is the resolution of the QDC
If the complete and unamplified SiPM signal had been measured the intrinsic gain of the SiPM would be given by $\Delta Q/\text{cell}/e$ with e representing the elementary charge. Since this is not the case $\Delta Q/\text{cell}$ is used for the remaining analysis, since it is proportional to the intrinsic gain. The constant of proportionality itself is given by the product of the fraction of the captured signal, roughly half as shown in figure 5.3, and the amplification factor of the amplifier.

6.3.2 Determination of the Breakdown Voltage

When the deposited charge per firing cell is known for all bias voltages of a given temperature the breakdown voltage can be calculated.
The charge deposited per fired cells as a function of the bias voltage is shown in figure 6.2.

As is expected from equation (4.12) there is a linear relation. The breakdown voltage is accessible from this data by extrapolating the gain down to zero.
For this a function of the form

$$\Delta Q/\text{cell} = C' \cdot (V_{\text{Bias}} - V_{\text{B}}), \tag{6.5}$$

is fitted to the data, where V_B is the breakdown voltage and C' is the 'effective' capacity. For an unamplified SiPM C' would represent the sum of the single cell capacity (see section 4.3 on page 21) and any additional parasitic capacities.

6.4 Results - Temperature Dependence

Putting all previous analysis steps for all measured bias voltages and temperatures together, the temperature dependence of the breakdown voltage can be analysed. Shown in figure 6.3 is the breakdown voltage as a function of the temperature for both 100 µm types[2]. Again a linear behaviour over the complete temperature range is observed and a fit with equation (6.2) yields the progression factor
$\beta = (56.56 \pm 0.33)\,\text{mV/K}$ for the 1x1 mm^2 and $\beta = (56.36 \pm 0.58)\,\text{mV/K}$ for the 3x3 mm^2 type.
Both are in good agreement with the stated value of $\beta = 56\,\text{mV/K}$ from the manufacturer [22].
Of special interest is the breakdown voltage of $\text{V}_B(T = 0\,^\circ\text{C}) = (68.37 \pm 0.01)\,\text{V}$ for the SiPM with the serial number 1203 which is in very good agreement with the value of $\text{V}_B(T = 0\,^\circ\text{C}) = (68.36 \pm 0.02)\,\text{V}$ obtained in [24] for the very same SiPM. There the breakdown voltage was determined with a different method which used the dark current of the SiPM above and below the breakdown voltage. A change of the behaviour of the dark current from a linear to a quadratic dependence on the bias voltage was observed and the breakdown voltage determined as the bias voltage at which this change took place. Because the method presented here does not require the measurement of the dark current below the breakdown voltage this method might be preferable for practical purposes.

For the rest of this thesis the breakdown voltage is always calculated as shown in figure 6.2.

[2] A complete temperature characterisation has not been performed for the 50 µm types as they only became available at a later time, when access to the cooling chamber was limited. The manufacturer states the temperature coefficient to be the same, as for the characterised types.

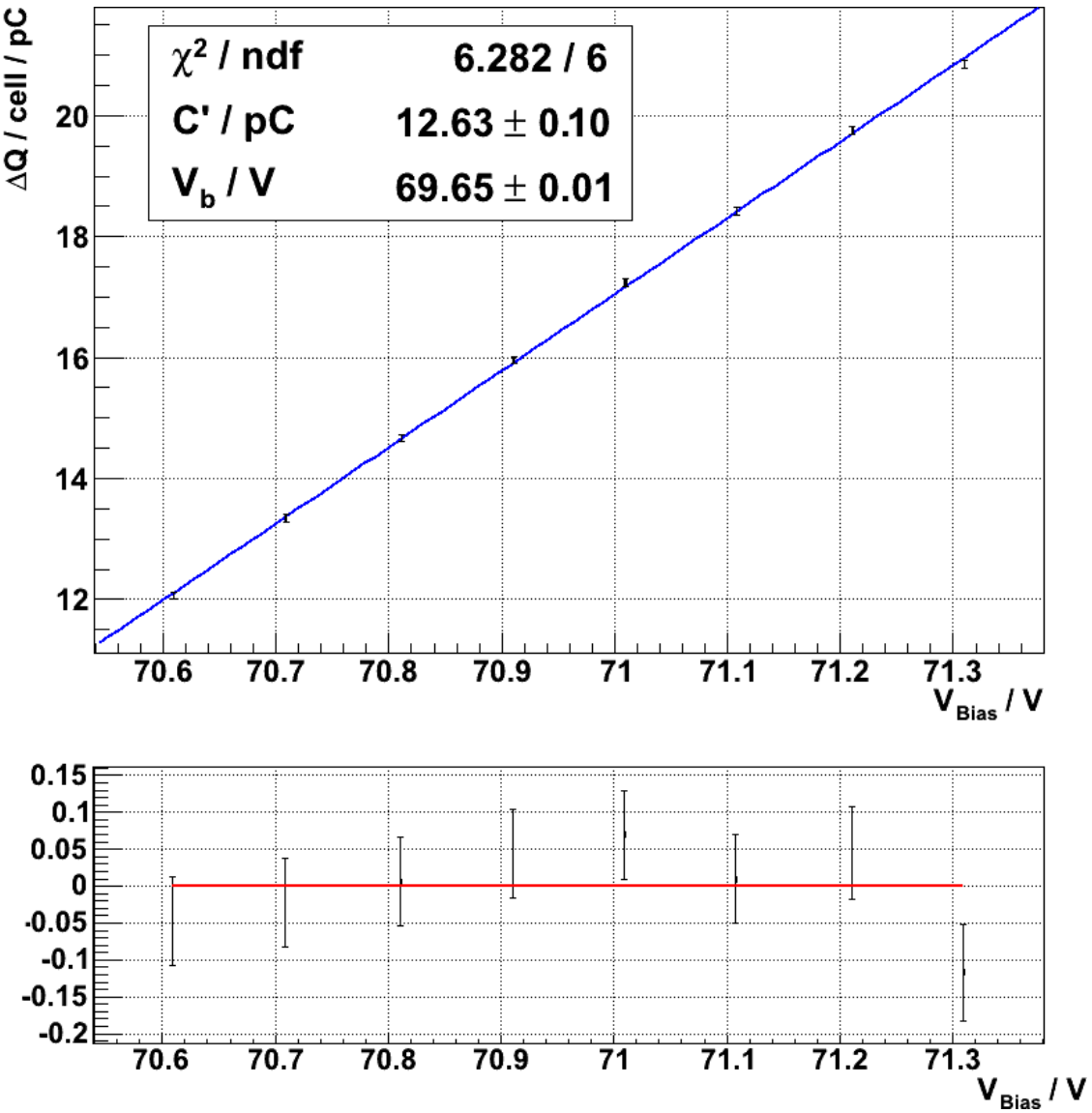

Figure 6.2: Deposited charge per fired cell over the bias voltage. The breakdown voltage V_b of the SiPM (1x1 mm^2, 100 µm cell pitch) can be determined by extrapolating the bias voltage V_{Bias} down to zero gain. Shown in the lower plot are the fit residuals.

6.5 Test of Automated Gain Stabilisation

From the results of the previous measurement it can be seen, that a relatively small change in the temperature of 2 °C results in a change of about 110 mV in the over-voltage. For a 100 µm cell pitch type operated at an over-voltage of 1.3 V[3] this would directly result in a change of the gain by 8.5%. Because of this, many applications will need to keep the over-voltage stable during operation. This can be achieved by keeping the temperature stable as in this chapter, however for practical purposes

[3]Which is roughly the over-voltage derived from the manufactures recommended bias voltage

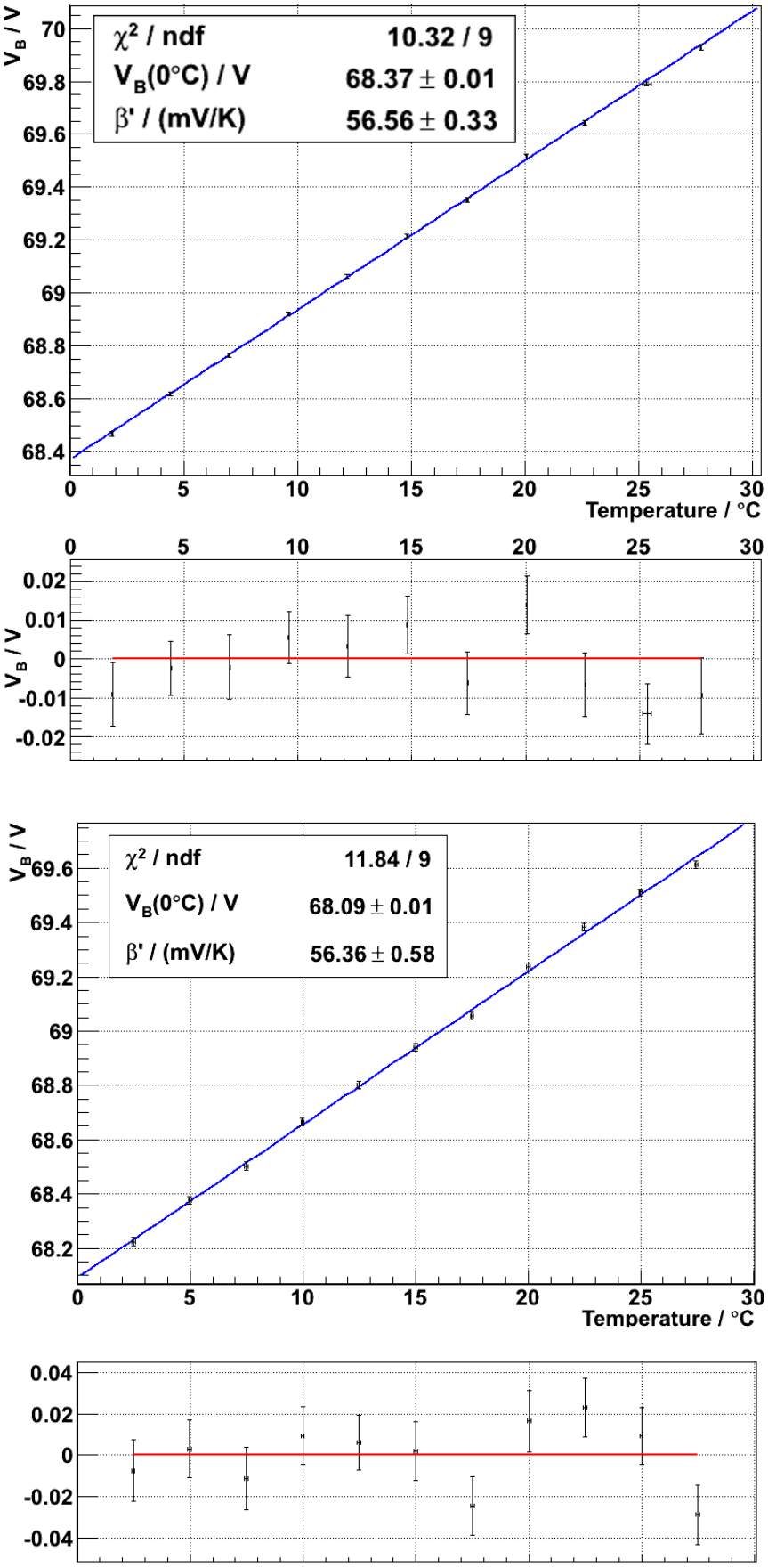

Figure 6.3: Temperature dependence of the breakdown voltage V_B. Above: 1x1 mm^2, 100 µm cell pitch, SN 1203 and fit residuals, below: 3x3 mm^2, 100 µm cell pitch, SN 512 and fit residuals. Systematic temperature uncertainty is 0.5 °C.

this might not be possible. Another possibility could be to adjust the bias voltage to account for temperature changes (with equation (6.2)). This has been implemented in newer versions of the amplifier board (see section 5.1 and figure 5.2 b)). To realise this, the base amplifier version is extended with a micro-controller. The micro-controller can monitor the temperature, with the temperature sensor on the board and adjust the bias voltage accordingly. A test of this setup is described in the following.

6.5.1 Measurement Setup and Procedure

The measurement setup and procedure is essentially the same as for the previous measurement. However, now the bias voltage is not adjusted automatically by the measurement program. Instead the bias voltage is only set to one value at the start of the measurement. The start is at the highest temperature and the set bias voltage is equivalent to an over-voltage of $(0.90 \pm 0.05)\,\mathrm{V}$ at this temperature. Two measurements are performed, one with the progression factor set to 0, i.e. no compensation of temperature changes, and one measurement with the progression factor set to $60\,\mathrm{mV/K}$. This is the closest to the actual value allowed by the accuracy of the board.
The rather low over-voltage is chosen to increase the effect of the expected overcompensation due to the difference between the progression factor used by the board and the actual, smaller value.

6.5.2 Results - Gain Stabilisation

The analysis is performed in the same way as in the previous section. The results from both measurements are shown in figure 6.4.

In the measurement with the progression factor set to 0, the gain rises sharply with the fall of the temperature, as is expected from the reduction in the breakdown voltage with temperature. To protect the QDC from the overshooting of the baseline caused by the increase in the over-voltage and subsequent signals with high frequency and amplitude, the measurement limited to temperatures above $15\,^{\circ}\mathrm{C}$.

In the measurement with the temperature compensation switched on, the gain remains relatively stable, however a slight overcorrection, leading to a reduction in the gain from higher to lower temperatures, can be seen.
With equation (5.3), an overcompensation of $4\,\mathrm{mV/K}$ over a range of $30\,^{\circ}\mathrm{C}$, and an SiPM operated at an over-voltage of $(0.90 \pm 0.05)\,\mathrm{V}$, a reduction from $(13.0 \pm 0.1)\,\mathrm{pC}$ down to $(11.3 \pm 0.1)\,\mathrm{pC}$ is expected.
This is in agreement with the observed $(11.0 \pm 0.1)\,\mathrm{pC}$, suggesting that the integrated compensation of the amplifier is functioning correctly within the limitations set by the degree of accuracy with which the progression factor β can be set.

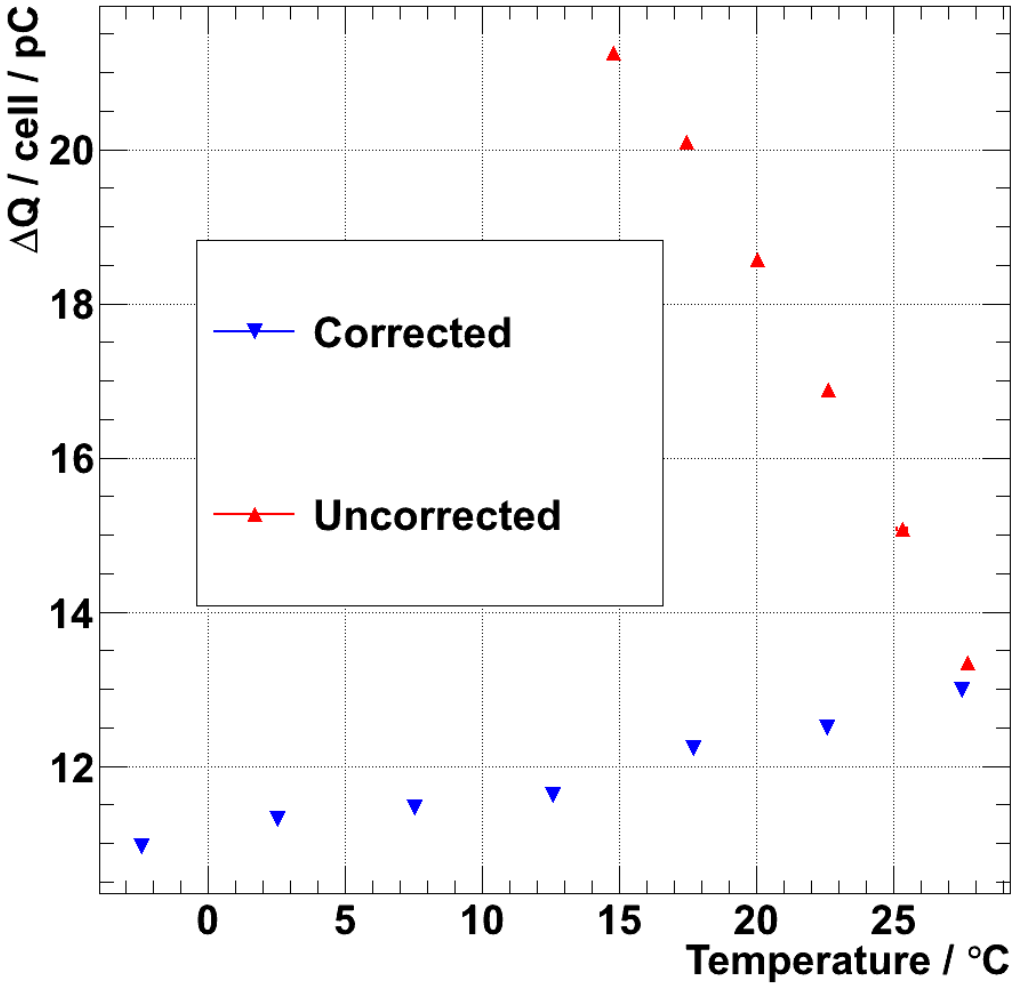

Figure 6.4: Gain stability with and without correction of the bias voltage for temperature changes by the extended version of the amplifier board. Systematic temperature uncertainty is 0.5 °C. (V_{OV}=(0.90 ± 0.05) V, 1x1 mm^2, 100 µm cell pitch)

6.6 Discussion and Summary

In this chapter the temperature dependence of the breakdown voltage for two different SiPM types was studied and found to be linearly dependent on the temperature over the measured temperature range. Both measurements gave a progression factor in good agreement with the specified value by the manufacturer of 56 mV/K.

As the normal over-voltage range of the studied SiPM lies between one and two volts it follows directly that a way of compensation for this change has to be used to achieve reliable measurements.
One method of achieving this is to automatically adjust the bias voltage with changes in the temperature. This has already been implemented in newer versions of the used

amplifier boards by the use of a micro-controller, and was found to be working within the limits allowed by the hardware. The limits were given by the accuracy with which the mentioned progression factor could be set. For many practical purposes this accuracy is nevertheless already good enough and more recent versions of the amplifier board allow setting the progression factor as a multiple of 5 mV/K [32] instead of the 20 mV/K for the amplifier in this measurement.

Another method is to keep the temperature constant. This can either be done by using a temperature controlled environment like the cooling chamber, used in this and the next chapter, or by keeping the measurements for a given over-voltage range short and determining the breakdown voltage for each range separately.
This method is used in chapter 8.

For practical purposes however this may not be possible, making the automated adjustment of the bias voltage the preferable method in such circumstances.

7. Correlated Noise

In addition to the random thermal noise[1] measured previously in a bachelor thesis [24] by J. Schumacher at III. Phys. Inst. A, RWTH Aachen University, SiPMs possess two kinds of correlated noise, where one cell firing can also cause other cells to fire [18].
This can happen either instantaneously or with a delay. The instantaneous component is believed to be due to light emitted during the avalanche process, whereas the delayed component is believed to be due to trapped charge carriers which are released at a later time [18].
The former process is known as 'optical crosstalk' and the latter as 'after-pulsing'.
A measurement of their respective probabilities is essential for photon detection with SiPMs since neglecting these effects in the analysis might lead to an overestimation of the detected photon flux. In addition the instantaneous component might lead to an earlier saturation of the SiPM for a given light flux as more cells are fired as otherwise would be. The measurement of their respective probabilities as a function of the over-voltage is described in the next two sections.

7.1 Optical Crosstalk

7.1.1 Theoretical background

The observation of photon emission during an avalanche breakdown process of a silicon p-n junction was made as early as 1955 [37]. A quantitative measurement of this effect showed an average of $2.9 \cdot 10^{-5}$ photons emitted with an energy higher than[2] 1.14 eV per carrier crossing the junction [38]. Different types (e.g. [39],[40],[38] and included references) exist to describe the light emission by one or a combination of multiple mechanisms including direct/indirect inter-band transition/recombination of electrons and holes, bremsstrahlung from electrons scattered at Coulombic centres and phonon assisted electron intra-band transitions.

Apparently there are still disagreements on the exact contributions of the different mechanisms at different wavelengths of the produced photons. Of more importance for this work however is the effect of the generated photons. The already cited photon yield above the band gap translates directly to an average of 3 to 30 produced photons per avalanche breakdown for an SiPM with an intrinsic gain of 10^5 to

[1] Or more accurately the dark noise, which, at the one cell noise level, is a combination of the random thermal noise and possible after-pulses of individual previous noise events.

[2] Approximately the band gap of silicon at room temperature [16].

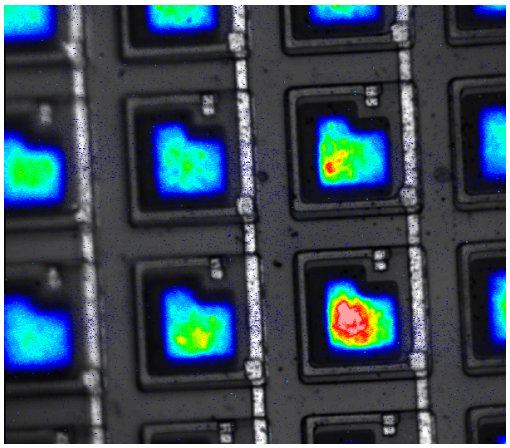

Figure 7.1: Light emitted from an SiPM. Image obtained by biasing an SiPM above breakdown in darkness and integrating the light flux coming from the SiPM over several seconds. The squares are cells of the SiPM. The colour-coded light intensity profile shows the region where the avalanche takes place. Adapted from [20].

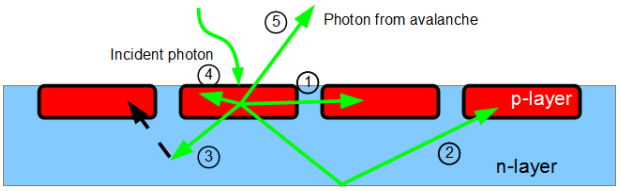

Figure 7.2: Crosstalk schematic. 1-5 are photons from the avalanche possibly causing crosstalk events.
1/2: Direct/by reflection at boundary absorption in new cell (crosstalk possible)
3: Absorption in low field region (crosstalk possible if created e-h pair (dashed, black line) drifts to a high field region)
4: Absorption in region of current avalanche (no crosstalk)
5: Emission of photon (no crosstalk)

10^6. A measurement of this effect can be seen in figure 7.1, where the light coming from an SiPM biased above breakdown in darkness was integrated over 300 seconds. From this image it can be seen that some of the produced light even leaves the SiPM which might cause problems if the SiPM is attached to a scintillator crystal and the exited light is reflected back to the SiPM. As for the light not leaving the SiPM, a portion of the created photons will be absorbed directly again in the initial cell. This is especially true for the short (blue and UV) wavelength photons, as the absorption length for them is short (see figure 8.1 on page 72).
The rest of the photons may exit the cell and get absorbed by neighbouring and remote cells or by 'dead' space. Dead space means here any non-depleted region e.g. the space between the cells, where it is unlikely that the electrons or holes reach a high field region, before they recombine.
If they are absorbed in an area where a new avalanche may be triggered, i.e. another cell, this can cause another cell to breakdown, resulting in an additional, simultaneous avalanche. A schematic of different possible scenarios is shown in figure 7.2.

7.1.2 Measurement of the Crosstalk Probability

7.1.2.1 Measurement Principle

Since the photon (or photons) causing the crosstalk event is emitted during the initial avalanche and reaches the cell in which the secondary avalanche is started

practically instantaneously, the resulting signal will show two or more cells firing at once. This can be seen from the voltage trace in figure 5.3 on page 35 which was taken in a light-tight box, where signals of up to 4 cells firing simultaneously can be seen. The shown magnitude cannot be due to thermal noise, because, as will be seen later in the analysis, thermal coincidences of two or more cells firing randomly together are far too rare for this.
The direct consequence is, assuming thermal noise and after-pulsing[3] are completely negligible, that all observed signals with a signal amplitude greater than the 1 cell (1 p.e.) level are due to crosstalk, as long as no light reaches the SiPM. Using a QDC and measuring charge spectra as shown in figure 6.1 on page 41 the crosstalk probability could then be calculated by counting all events above the 1 p.e. level as crosstalk events and dividing them by the total number of events.
This represents the actual crosstalk probability, provided that the effects of after-pulsing and thermal-noise can indeed be neglected. Otherwise the crosstalk probability, calculated this way, will be the sum of the 'true' crosstalk probability and of the random coincidences of thermal events during the QDC gate and after-pulses from the initial pulse, which also occur in the rest of the gate width.
After-pulsing can be eliminated by setting the QDC gate as shown in figure 5.3. Here the integration of the signal charge is stopped, as soon as the initial signal has reached its maximum amplitude. This corresponds to roughly 11-15 ns of integration time after the avalanche. As the SiPM cells need a few tens of nanoseconds to recharge [25] a possible after-pulse event should not be able to generate enough additional charge to classify the event as a two cell event from the QDC spectra. Instead the event would be placed somewhere between the corresponding peaks. With the used analysis method this would only increase the uncertainty of the probability but not the probability itself.
The assumption of negligible thermal noise can be tested. As measured in [24], the dark noise rate drops steeply with the temperature, reaching a reduction by about a factor 10 by cooling down from $(29.0 \pm 0.5)\,^{\circ}\mathrm{C}$ to $(2.3 \pm 0.5)\,^{\circ}\mathrm{C}$. The observed one-cell noise rate was 1.0-1.1 MHz at the higher, and 100-150 kHz at the lower temperature for the 100 µm cell pitch, 1x1 mm^2 type at an over-voltage of $(1.40 \pm 0.05)\,\mathrm{V}$.
Knowing this, the contamination of thermal-noise can be checked by evaluating the crosstalk probability for different temperatures. If there is no contamination of thermal noise the probability will remain constant with temperature. Otherwise the probability will decrease with the temperature, as the probability of random thermal coincidences decreases and may converge toward the true value[4], if the noise rate has been reduced far enough and the used measurement interval is short enough.

For the QDC, this measurement interval is given by the gate length of 30 ns. From the measured FADC traces a pulse height spectrum, similar to the charge spectrum of the QDC, can be constructed, also allowing the calculation of the crosstalk probability. Since the FADC analysis may allow to differentiate between consecutive events on a shorter time scale than the QDC, it is used in addition to the QDC measurement.

[3] See section 7.2.

[4] Under the assumption that optical crosstalk, at the same over-voltage, is independent of the temperature. That this assumption is correct can be seen later in the analysis in figure 7.5.

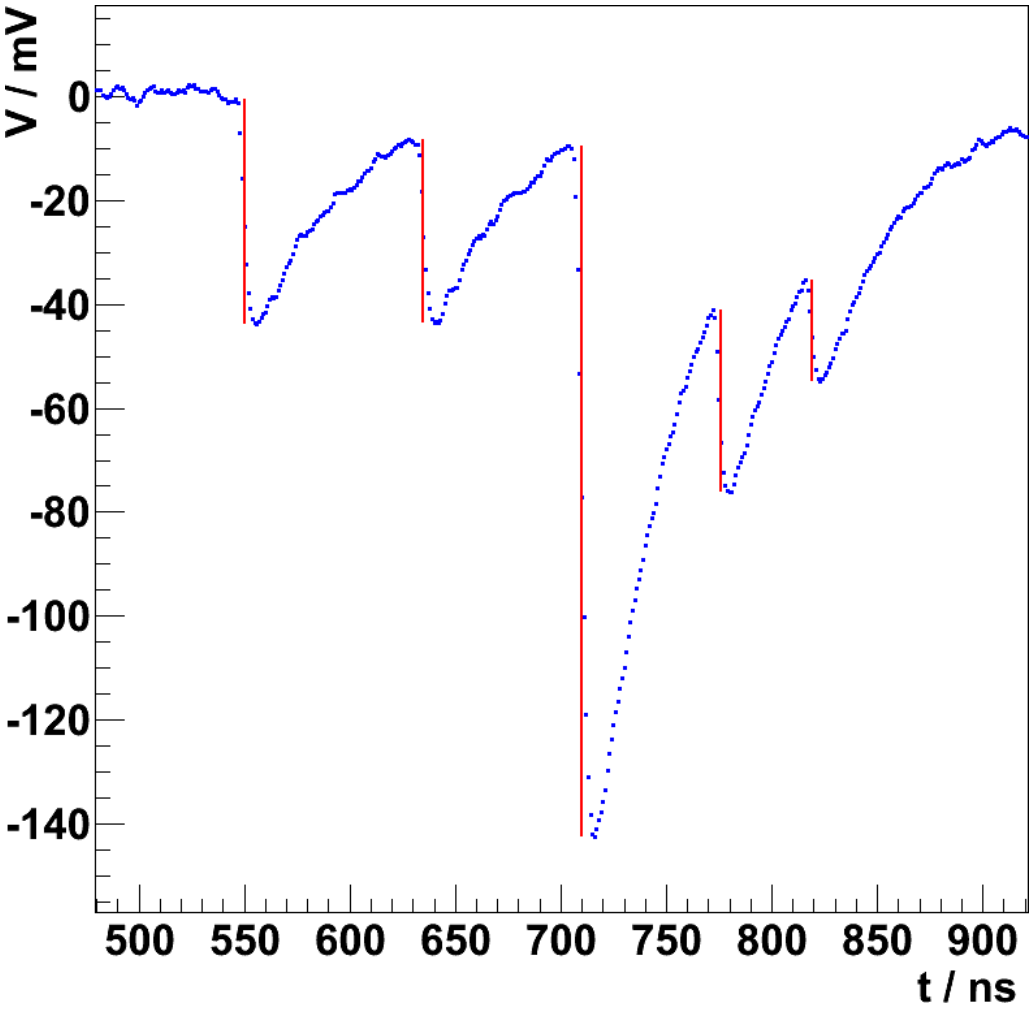

Figure 7.3: Measured FADC trace in darkness with multiple SiPM events. Red (vertical) lines represent the reconstructed peak amplitude and where the identified peak has reached 50% of its amplitude. A schematic of the analysis algorithm can be found in the appendix and a description in the text.
(1x1 mm^2, 100 µm cell pitch, T = (28.2 ± 0.1(stat.) ± 0.5(sys.))° C,
V_{OV}= (1.30 ± 0.02) V)

7.1.2.2 Measurement Setup and Procedure

As the measurement setup used in the previous chapter and described in chapter 5, yielded satisfactory results the same setup is used here. The measurement procedure is generally the same as in the previous chapter with the exception, that now FADC traces are acquired in addition to the QDC measurement.

7.1.3 Analysis

7.1.3.1 FADC trace analysis

Before a pulse height spectrum can be constructed from the FADC measurement data the FADC traces have to be analysed first. Part of a measured FADC trace is shown in figure 7.3. As the trace was recorded with the SiPM in darkness, all of the events are due to either thermal noise, optical crosstalk or after-pulsing. For example the largest peak in the middle is likely due to crosstalk and the signals with reduced height located on the tail may be after-pulse events. One can already see that a simple threshold scan is not sufficient for the analysis, as the pulses have a decay time much longer than their rise time, causing closely spaced pulses to pile up. A pulse height spectrum analysis based on a threshold scan would then be biased as the pile up would lead to the misidentification of peaks located in the tail of previous signals, identifying them as peaks with a higher amplitude than they actually possess.
For an unamplified SiPM signal the decaying edge of the pulse is caused by the recharge[5] of the fired cell(s) and can be described by an exponential function with the time constant of the function representing the cell recovery time [25].
This also holds true for an amplified signal, however the signal may also be modified due to possible bandwidth limitations of the amplifier.

In addition to the pile-up of signals, the analysis must also be able to distinguish between the noise of the amplification chain, and an actual SiPM signal. The most robust way of analysing the FADC traces explored uses the steep rise of the SiPM signal and is explained in the following.
For the analysis a time window of a defined length moves over the trace. If the signal is further away from the baseline at the point of the end of the window than at the point in the beginning, the latter is marked as the potential start of a signal. The analysis window then moves on in the trace and identifies the last point, where the signal is still further away from the baseline at the beginning of the window than at the end. As the signal rise is very steep this should always be the case during the complete signal rise time, until the point in the trace after which the pulse has ended and the signal slowly returns to the baseline. If this point is found, the maximum voltage distance between the time windows at the suspected start and end point is calculated, representing the amplitude of the potential peak. If the amplitude is above a certain threshold, the signal is identified as a new SiPM signal, with the previously calculated amplitude and the starting point set to the time, where the signal has reached 50% of its height. This information is then saved and the analysis resumes, starting from the end of the previous time window. A schematic of the analysis method can be found in the appendix.
The length of the time window itself is chosen as 3 ns. This is sufficient not to end the search of the signal prematurely due to noise and still allows for a fine separation between consecutive signals. The threshold used for deciding whether an actual SiPM signal has been observed, is determined by analysing a few traces with no SiPM signal. The threshold is then defined as two times the maximum

[5] The cell recharge may be modelled as the exponential recharge of a capacitor [25].

observed amplitude due to noise, making the method robust with regard to noise. This threshold is then used for the analysis of the traces. To test, whether setting this threshold misses some of the SiPM signals with small amplitude, i.e. is set too high, all traces are analysed with the threshold set to 1.5 of the maximum noise amplitude. All later analyses, such as the derivation of the crosstalk probability, then use both data sets and test whether there is a difference in the end results. This only happens at very low over-voltages with corresponding low signal amplitudes and the results from these over-voltages are subsequently excluded.

With the fall time of the amplified signal being about 10-15 ns (see figure 5.3) and the chosen analysis window of 3 ns the analysis method is expected to be able to distinguish between consecutive signals, provided they are separated by at least 13-18 ns, an improvement on the QDC with its 30 ns gate. A further improvement may be realised with an amplifier with a higher bandwidth.

An example of an FADC trace analysed with this method is shown in figure 7.3. An example of a larger trace can be found in the appendix.

7.1.3.2 QDC Charge and FADC Signal Amplitude Spectra Analysis

From the analysed FADC traces a pulse height spectrum can be constructed, similar to the QDC charge spectrum shown in figure 6.1 on page 41. For this, all found peak amplitudes are filled into a histogram, provided that no pulse has been observed in the previous 300 ns. This requirement is added to ensure, that only signals with full amplitude and not signals located on the tail of a previous signal, or signals with reduced amplitude due to recharging are added. This would worsen the separation between events with different numbers of cells firing. As the crosstalk probability of a fully charged cell is not expected to depend on any previous activity, this requirement is not expected to have any influence on the results.
An example of such a pulse height spectrum is shown in figure 7.4. Analog to the QDC spectrum in figure 6.1 the first peak corresponds to the firing of one cell at a given time. The second peak corresponds to two cells firing either simultaneously or at least the second cell firing within the signal fall time of the first and so on. As can be seen in the figure, a better separation between the individual peaks is achieved in comparison to the QDC spectra. In the case that thermal noise is negligible within the short measurement duration of the QDC and analysis window of the FADC, the crosstalk probability P_{Cross}, defined here as the probability that one firing cell causes one or more cells to fire with it, can be calculated from the spectra with

$$P_{\mathrm{Cross}} = \frac{N_{>1}}{N}. \tag{7.1}$$

Here N is the total number of events and $N_{>1}$ the number of events with more than one cell firing. The latter number is determined from the FADC and QDC spectra by counting all events above the 1.5 p.e. level as multi cell events. In figure 7.4 this is indicated by the first red line. As the peaks there are completely separated, a counting threshold of 1.5 p.e. identifies all events correctly. For the QDC and, depending on the over-voltage and the characterised SiPM some FADC spectra,

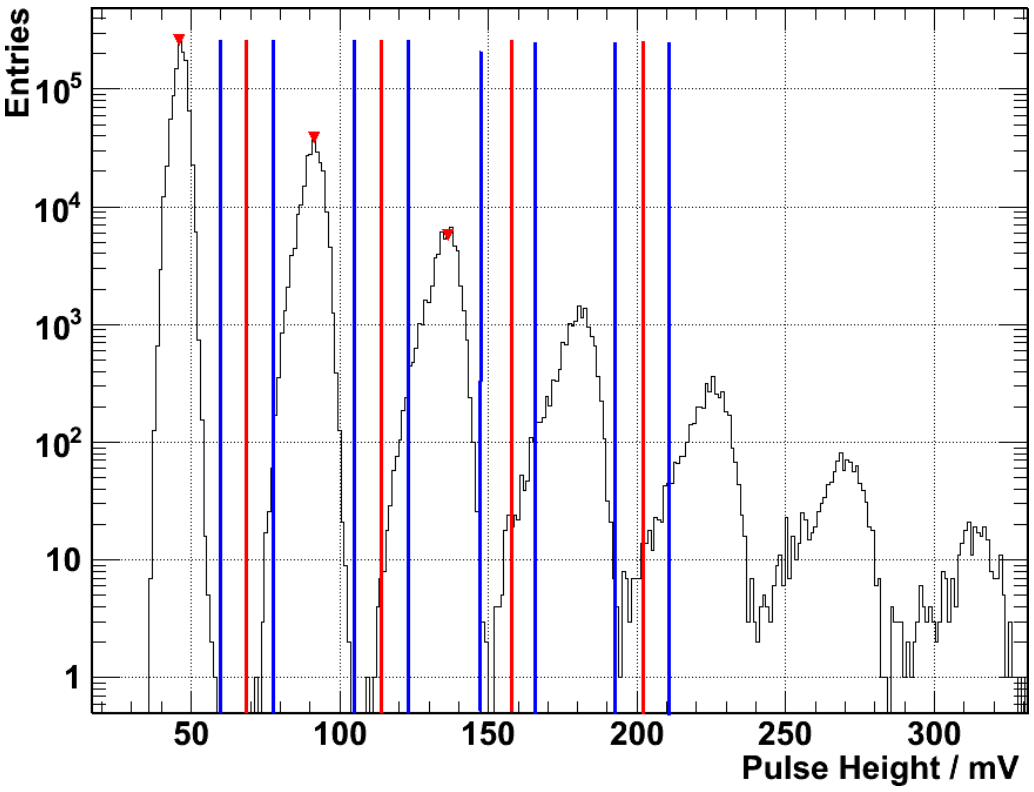

Figure 7.4: SiPM pulse height spectrum, measured in darkness. First peak is the 1 p.e. peak. Red (middle) lines mark 1.5 p.e., 2.5 p.e., 3.5 p.e. and 4.5 p.e. amplitudes, blue (left, right) are used to estimate the systematic uncertainty of the event counts. All events above the 1.5 p.e. level are either due to optical crosstalk or coinciding thermal noise events.
(1x1 mm^2, 100 µm cell pitch SiPM, T = (28.2 ± 0.1(stat.) ± 0.5(sys.))° C,
V_{OV}= (1.30 ± 0.02) V)

the peaks partially overlap (e.g. in figure 5.3). In these cases setting the counting threshold this way may misidentify some events. To estimate this systematic uncertainty the threshold is also set to 1.3 p.e. and 1.7 p.e., and the crosstalk probability is calculated with these thresholds (indicated by the blue lines in figure 7.4). The statistical uncertainty of the probability is given by the binomial error

$$\sigma_{P_{\text{Cross}}} = \frac{1}{N}\sqrt{Np\,(1-p)}, \tag{7.2}$$

with the estimate of p= $\frac{N_{>1}}{N}$.
For the QDC measurements the systematic uncertainty dominates the uncertainty of the result, while, depending on the SiPM type and over-voltage, either the statistical or the systematic uncertainty dominate the uncertainty of the result from the FADC measurement. For simplicity reasons both uncertainty contributions are linearly added for the rest of this section.

To determine whether the results obtained from equation (7.1) represent the actual crosstalk probability, or the crosstalk probability *and* an additional component from

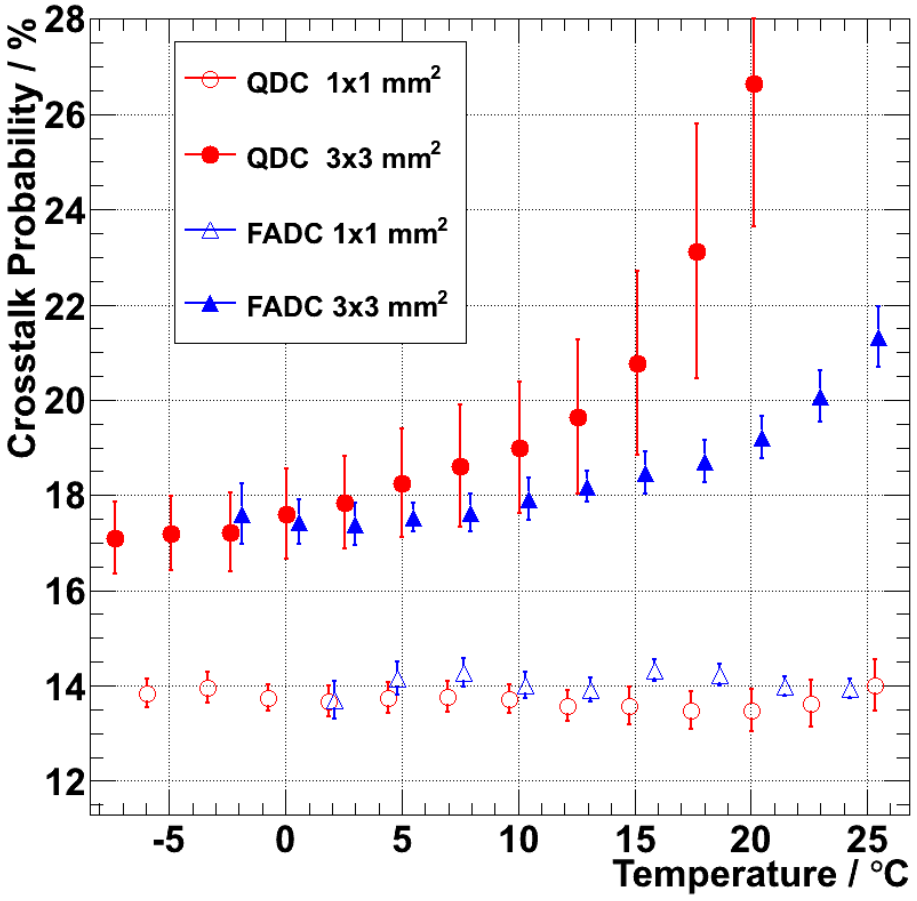

Figure 7.5: Crosstalk probability as a function of the temperature. The change with the temperature for the 3x3 mm^2 type indicates a contamination by thermal noise for the upper temperatures.
(100 µm cell pitch,V_{OV}= 1.0 V)

random coincidences of thermal noise events, the FADC and QDC spectra are evaluated for all measured temperatures. The results for a fixed over-voltage of 1.0 V of the 100 µm cell pitch types[6] is shown in figure 7.5. As can be seen the probability remains constant for the 1x1 mm^2 type indicating that the crosstalk probability obtained with this method is not overestimated due to thermal noise. For the 3x3 mm^2 type[7] a change with the temperature can be seen, showing an overestimation of the crosstalk probability for higher temperatures due to accidental coincidences with thermal noise events. The value converges and remains constant below 10 ° C and 0 ° C for the FADC measurement and QDC measurement, respectively. This again indicates that, below the stated temperatures, the probability obtained from equa-

[6]Obtained by linear interpolation between the two closest measured voltages.
[7]Which naturally has a higher noise rate than the smaller type.

tion (7.1) represents the actual crosstalk probability.
A feature of possible interest is, that the probability is higher for the 3x3 mm^2 type than for the 1x1 mm^2 type at a given over-voltage. A possible explanation for this could be that, because of the increased number of cells and thus active area, a given photon generated by the avalanche has a higher probability of hitting an active area and consequently causing a secondary avalanche.

As the results from the FADC measurement are in agreement with the QDC measurement but have a smaller uncertainty, and the FADC measurement does not require as much cooling, only the FADC is used in the final crosstalk analysis. For this a measurement with high statistics of one to two million FADC traces is performed at a temperature of (1.0 ± 0.5) °C for the 3x3 mm^2 types and at temperature of (25.5 ± 0.5) °C for the 1x1 mm^2 types.

7.1.4 Results - Crosstalk Probability

The results of the high statistic measurement for all studied SiPM types is shown in figure 7.6. Again the crosstalk probability is consistently higher for the types with the larger area for a given cell pitch and over-voltage, for the possible reasons discussed previously.
The crosstalk probability for a given SiPM type can be seen to rise with the over-voltage. This may be understood from the linear rise of the gain with the over-voltage (see figure 6.2 on page 43) resulting in the generation of more photons per avalanche, and the additional increase of the trigger probability with the over-voltage (see figure 4.6 on page 24).
For a given over-voltage the crosstalk probability is lower for the 50 µm types, consistent with their smaller active area and gain ([22], also see table 4.1 on page 28).

The missing information required to correct for optical crosstalk, is exactly how many additional cells fire due to optical crosstalk. So far all events above the one cell event level where considered equally as crosstalk events. However in a given crosstalk event either only one or multiple cells can fire for the firing of one initial cell. To calculate how many additional cells fire due to crosstalk, equation (7.1) is modified and instead of all events above the 1.5 p.e. level, only events belonging to a specific number of fired cells is used (see figure 7.4 for the used thresholds). Only events with up to three additional cells are considered as these constitute the vast majority of crosstalk events. Besides the additional threshold the remaining analysis is performed as already described.
The average number of additional firing cells due to crosstalk, can be found in figure 7.7 for all studied SiPMs, and the fraction of crosstalk events, where exactly one, two and three additional cells fire is shown in figure 7.8 for the 1x1 mm^2, 100 µm cell pitch SiPM[8]. As can be seen, the one cell events always constitute the majority of crosstalk events in the studied range, with their fraction falling and the share of multi-cell crosstalk events rising with the over-voltage. Since the crosstalk probability can

[8]The results for the other SiPM types can be found in the appendix.

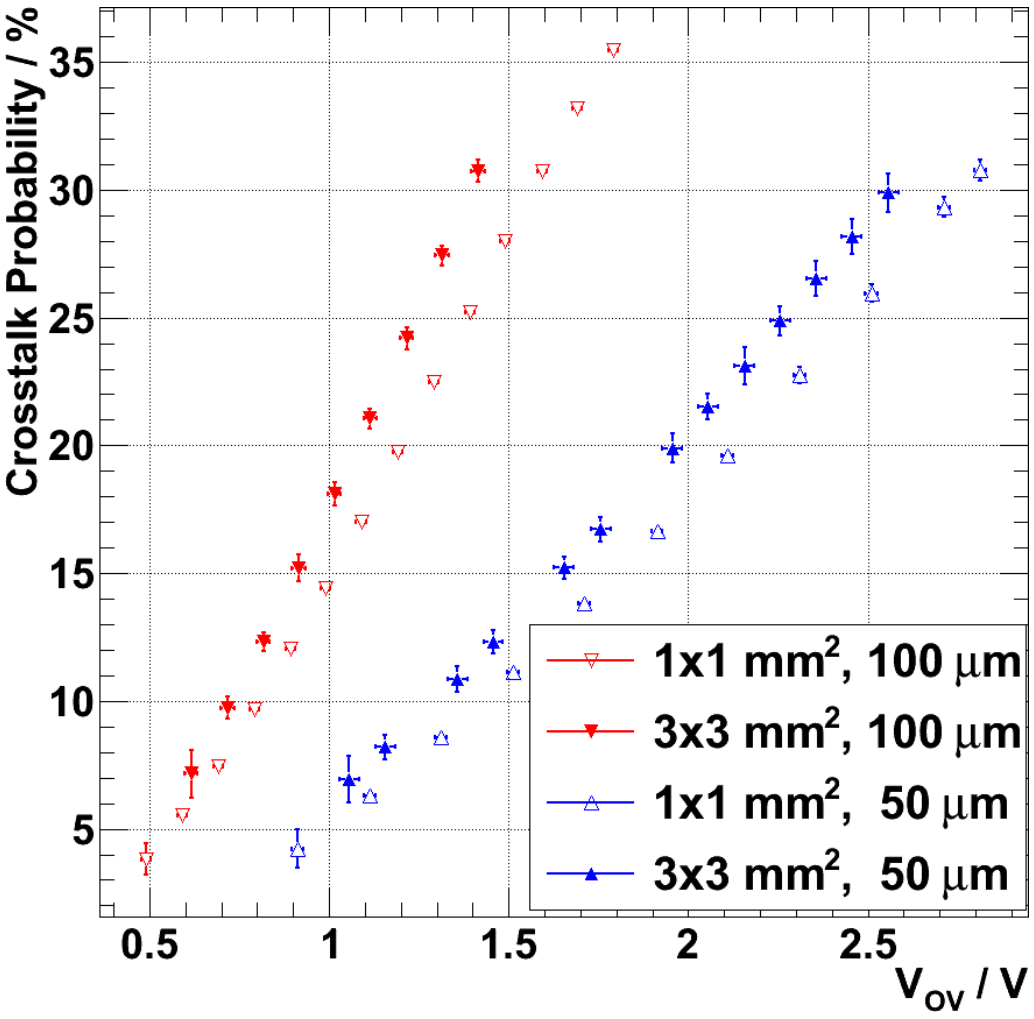

Figure 7.6: Crosstalk probability as function of the over-voltage for all studied SiPM types. The typical over-voltage lies in the 1.2-1.4 V range for the 100 µm cell pitch types and in the 1.9-2.2 V range for the 50 µm cell pitch types.

be expressed as a function of the over-voltage a correction for this effect could be performed on a statistical basis.

7.2 After-pulsing

7.2.1 Theoretical background

The delayed component of correlated noise in SiPM is believed to be due to the trapping of charge carriers at deep levels during the avalanche [18]. In contrast to the shallow donor and acceptor levels[9], which are close to either the conduction or valence band, deep levels are located further away from these energy levels, within the forbidden zone [15]. Like shallow levels, deep levels are caused by impurities or

[9]See Chapter 4.

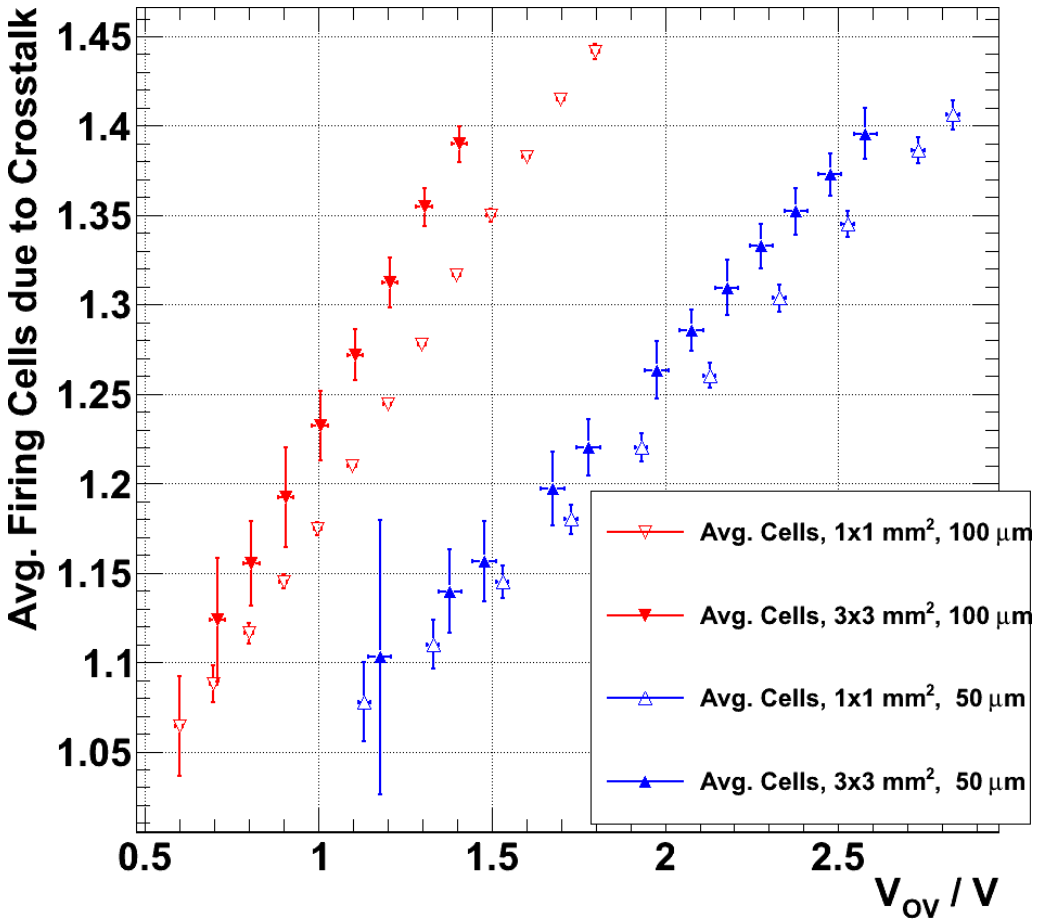

Figure 7.7: Average number of additional cells fired due to crosstalk as function of the over-voltage. The typical over-voltage lies in the 1.2-1.4 V range for the 100 µm cell pitch types and in the 1.9-2.2 V range for the 50 µm cell pitch types.

defects in the crystal. During the avalanche an electron or hole may pass close to a trap centre and become trapped, before it is released with a statistical time delay to the conduction or valence band [15].

A schematic of an electron, trapped in the depletion region is shown in figure 7.9. If the release occurs after the original avalanche has ended this can serve as the trigger for an additional avalanche. The release of the carriers and subsequently the depopulation of the occupied trap levels is expected to follow an exponential distribution with the characteristic trap life time depending on the energy level of the trap [41]. As different kinds of defects lead to different energy levels [16], multiple trap levels and corresponding life times may be present.

7.2.2 Measurement of the After-pulse Probability

7.2.2.1 Measurement Principle

In contrast to the crosstalk measurement, where, for a sufficiently cooled SiPM, any event with multiple cells firing simultaneously could be identified as a crosstalk

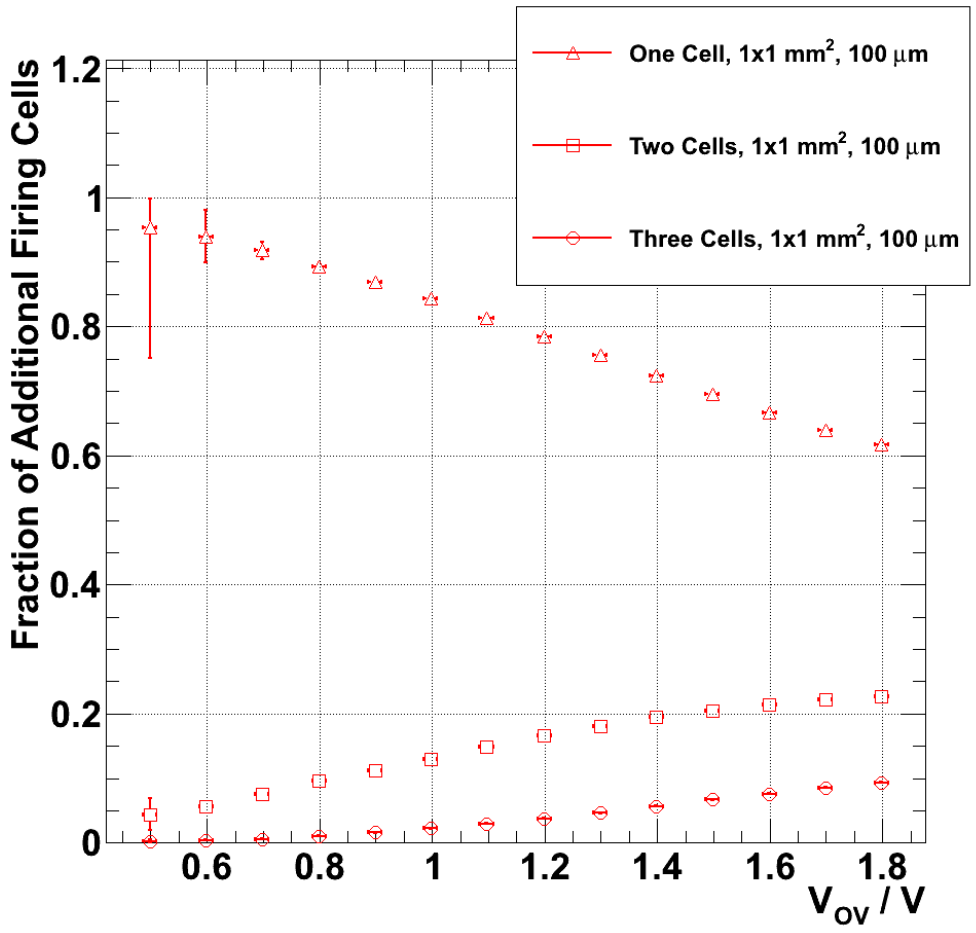

Figure 7.8: Fraction of crosstalk events where exactly one, two or three additional cells are fired due to optical crosstalk as a function of the over-voltage. The typical over-voltage lies in the 1.2-1.4 V range for the 100 µm cell pitch type.
(1x1 mm^2, 100 µm cell pitch SiPM, remaining plots can be found in the appendix)

event, the identification as an after-pulse event is not possible on a per event basis. As the identification on a per event basis is not possible the idea presented in [42] of distinguishing between thermal and after-pulse events on a statistical base is used here. Since both, the time difference between the initial pulse and its after-pulse, as well as the time differences between consecutive thermal noise pulses are expected to be exponentially distributed, their corresponding frequency may be extracted from the measured time difference between consecutive pulses by fitting a superposition of exponential functions to the distribution.
A requirement for this analysis method is that the after-pulsing time constant(s) and the mean time between the thermal noise pulses are sufficiently distinct. Previous measurements of different types of SiPMs reported either one after-pulsing time constant in the range of 80-200 ns or two different time constants, a 'fast' one in the range of 10-20 ns and a 'slow' one in the range of 80-200 ns [43],[44].

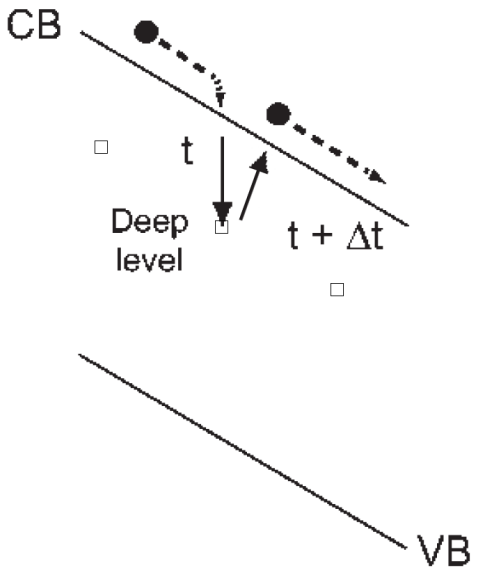

Figure 7.9: Trapping schematic. An electron is trapped at a deep level impurity (rectangle) at time t and released with a statistical delay Δt. Modified from [41] (VB: valence band, CB: conduction band)

Under the assumption, that this is is also true for the SiPMs at hand, it follows that the mean time between thermal noise events has to be larger than approximately 500 ns translating to a thermal noise rate below 2 MHz. Otherwise it would be very difficult or impossible to distinguish between the contributions from the slow after-pulses and the thermal noise pulses. For the 1x1 mm^2 SiPM this is the case, even at room temperature [24], but the 3x3 mm^2 types have to be cooled down until the dark noise rates are sufficiently low.

7.2.2.2 Measurement Setup and Procedure

The measurement setup and procedure are described in section 5.1 and 5.2 from pages 29 to 40.
Because the measurement conditions of the FADC traces from the crosstalk measurement in section 7.1.3.2 fulfil the requirement on the dark noise rate, they are also used here. For this measurement one to two million FADC traces were measured at a temperature of (1.0 $\pm$ 0.5) °C for the 3x3 mm^2 types and at a temperature of (25.5 $\pm$ 0.5) °C for the 1x1 mm^2 types.

7.2.3 Analysis

7.2.3.1 Time Distribution Between Pulses

From the analysed FADC traces (see section 7.1.3.1) a time distribution, like the one shown in figure 7.10, can be constructed. For this the FADC traces are analysed one by one and the first found signal in a given trace is considered a start signal provided

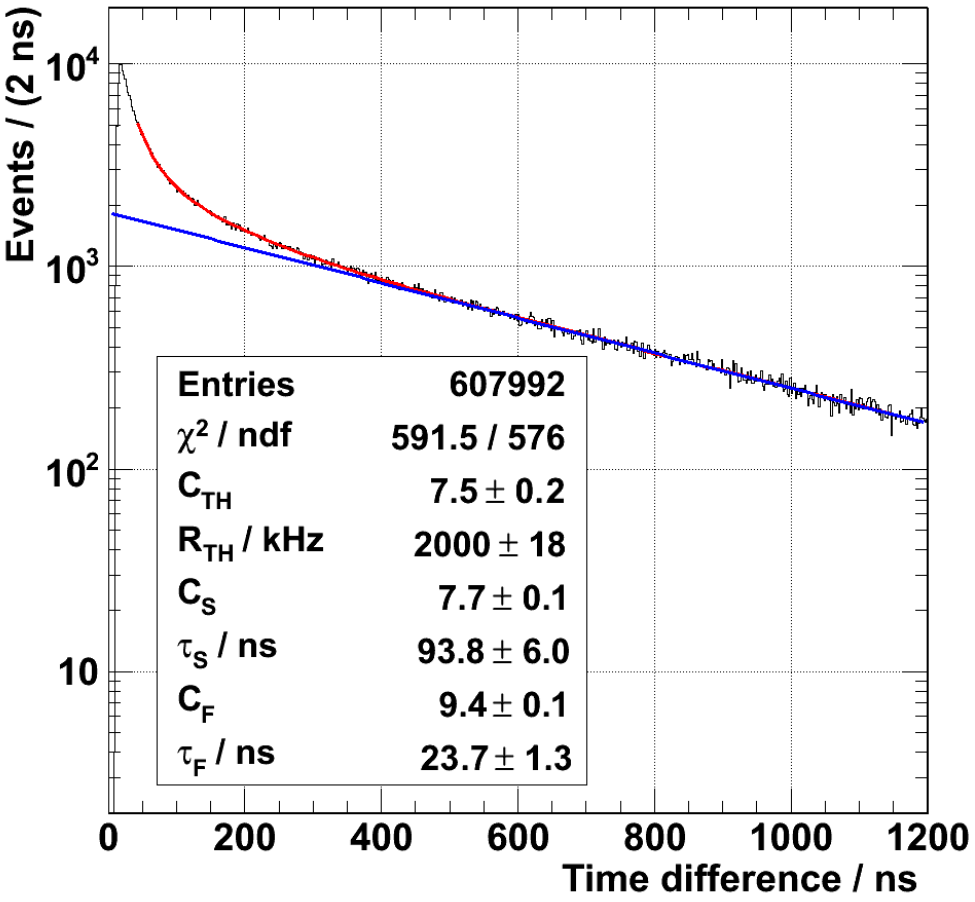

Figure 7.10: Distribution of the time difference between an initial 1 p.e. start pulse and the next pulse. The blue (straight) line represents the contribution of thermal noise pulses, the red (curved) line is a fit of three exponential functions to the data (see equation (7.4)). A zoom in the 0-400 ns region of this distribution can be found in the appendix.
(3x3 mm^2, 50 µm cell pitch, V_{OV}= (2.10 ± 0.04) V)

that, a) there was no signal 300 ns prior to the signal and b) the signal amplitude is less than the 1.5 p.e. amplitude. Otherwise the search continues until a suitable start signal has been found. If a start signal is found and if there is at least one signal remaining in the trace, the time difference between the start signal and the next signal is added to the time distribution histogram (e.g. the one shown in figure 7.10). Because the FADC has a finite trace length the last step is only taken if a longer, chosen maximum time difference could still have been contained in the trace. Otherwise the start pulse is discarded and the analysis continues with the next trace. The maximum time difference is chosen as 1200 ns, which is roughly half the trace length. Neglecting this step would lead to a bias towards smaller time differences because these can still be detected, while later after-pulses would fall outside of the

trace.
Similarly requirements a) and b) are necessary, otherwise the after-pulse probability would be overestimated since it is more likely to observe at least one after-pulse if multiple cells have fired either at once (b) or shortly one after the other (a). As the maximum measured trap lifetime (see below) is (150 ± 23) ns, the required quiet time of 300 ns should be sufficient not to measure a significant fraction of after-pulses which stem from signals before the start signal. For a measurement with a greater trace length, this threshold could be raised, but in this case this would reduce the number of usable time differences too far for this analysis.

7.2.3.2 Fit Procedure and Parameters

An example of a pulse time distribution resulting from the previous analysis is shown in figure 7.10.
A convenient way to understand this distribution is to analyse it from large to small time differences. For larger time differences the uncorrelated thermal noise is expected to dominate the distribution. As can be seen, an exponential function of the form (represented by the blue (straight) line in figure 7.10)

$$n_{\mathrm{th}} = e^{(C_{TH} - R_{TH} \cdot t)}/2\,\mathrm{ns}, \tag{7.3}$$

matches with the distribution from 600 ns to 1200 ns. Here $\mathrm{R_{TH}}$ represents, what for now is suspected to be, the thermal noise rate and $e^{C_{\mathrm{TH}}}/R_{\mathrm{TH}}/2\,\mathrm{ns}$ the total number of thermal noise events[10]. For smaller time differences a clear excess over the thermal noise contribution can be recognized, indicating the existence of after-pulsing in the SiPM.
In order to describe the data for smaller time differences from the observed maximum around 25 ns, the inclusion of two additional exponential functions is necessary. One function is sufficient to describe the distribution from 160 ns to 1200 ns and the second function is necessary for the correct description from 25 ns to 1200 ns. This may indicate the existence of two different trap levels with two different lifetimes. From now on the after-pulsing components with the smaller time difference τ_{F} is referred to as the 'fast' component, and the other, with the larger time difference τ_{S} as the 'slow' component.
The resulting fit function

$$n = (e^{(C_{TH} - R_{TH} \cdot t)} + e^{(C_S - \frac{t}{\tau_{\mathrm{S}}})} + e^{(C_{\mathrm{F}} - \frac{t}{\tau_{\mathrm{F}}})})/2\,\mathrm{ns}, \tag{7.4}$$

with the additional constants $\mathrm{C_S}$ and $\mathrm{C_F}$ describes the observed distributions very well from the maximum down to the largest time differences. An example of this is shown in figure 7.10 and a table of all fit parameters for all characterised SiPMs can be found in the appendix.
For very small time differences the distribution drops steeply due to the inability to resolve very closely following pulses in the FADC traces and due the significantly reduced peak height of after-pulses occurring very shortly after their original pulse.

[10] 2 ns is the used bin size.

Before the after-pulse probability can be calculated from the different components of the time distribution, it is necessary to test whether they have been identified correctly. For this the component identified as the thermal noise rate is plotted in figure 7.11 and the trap-lifetimes in figure 7.12[11]. In the first plot the rate can be seen to rise with the over-voltage. More specifically the thermal noise rate R can be described by a linear function of the form

$$R = r \cdot V_{\mathrm{OV}} \tag{7.5}$$

with the only free parameter r specifying the increase of the thermal noise rate with the over-voltage[12]. As the thermal generation rate of electron-hole pairs is constant for a given temperature (see section 4.4.1 on page 26), but the probability of any given electron-hole pair to generate an avalanche rises with the over-voltage, this component indeed represents the thermal noise rate.
Since trigger measurements with the oscilloscope only give the frequency of the dark noise, which includes the effect of after-pulsing, this method can be used to measure the pure thermal noise rate if this is desired and provided that the inverse of the thermal noise rate is larger than the slow after-pulsing time constant.
In contrast to the thermal noise rate, no significant change with the over-voltage is observable neither for the trap lifetimes nor the ratio

$$R_{\mathrm{F/S}} = \frac{e^{C_{\mathrm{F}}} \cdot \tau_{\mathrm{F}}}{e^{C_{\mathrm{S}}} \cdot \tau_{\mathrm{S}}} \tag{7.6}$$

of fast to slow after-pulses. A summary of the weighted means of the time constants and the ratios is shown in table 7.1. The ratio and approximately also the trap lifetimes are in agreement for the same cell pitch size, however, the lifetimes are significantly shorter for the smaller cell pitch and the ratio also differs. A clear reason for this could not be found. Additionally, although still within the statistical uncertainties, there is a slight upwards trend noticeable in the trap lifetime and a downward trend in the ratio of fast to slow after-pulses for the larger area types measured at a lower temperature. An increase of the trap lifetime may be expected as the trap de-excitation time increases with a fall in the temperature [18]. To see, whether this is the case would require measuring the same type at different temperatures which, for reasons already stated, is not possible for the used method and the used SiPMs.

7.2.4 Results - After-pulse Probability

With the after-pulsing and thermal noise contributions to the time distribution identified, the remaining question is, how to take the recovery behaviour[13] of the SiPM

[11] For one SiPM type, the remaining vales can be found in table of fit parameters in the appendix.
[12] A plot with this fit applied can be found in the appendix
[13] And consequently the drop off for very small time differences in figure 7.10

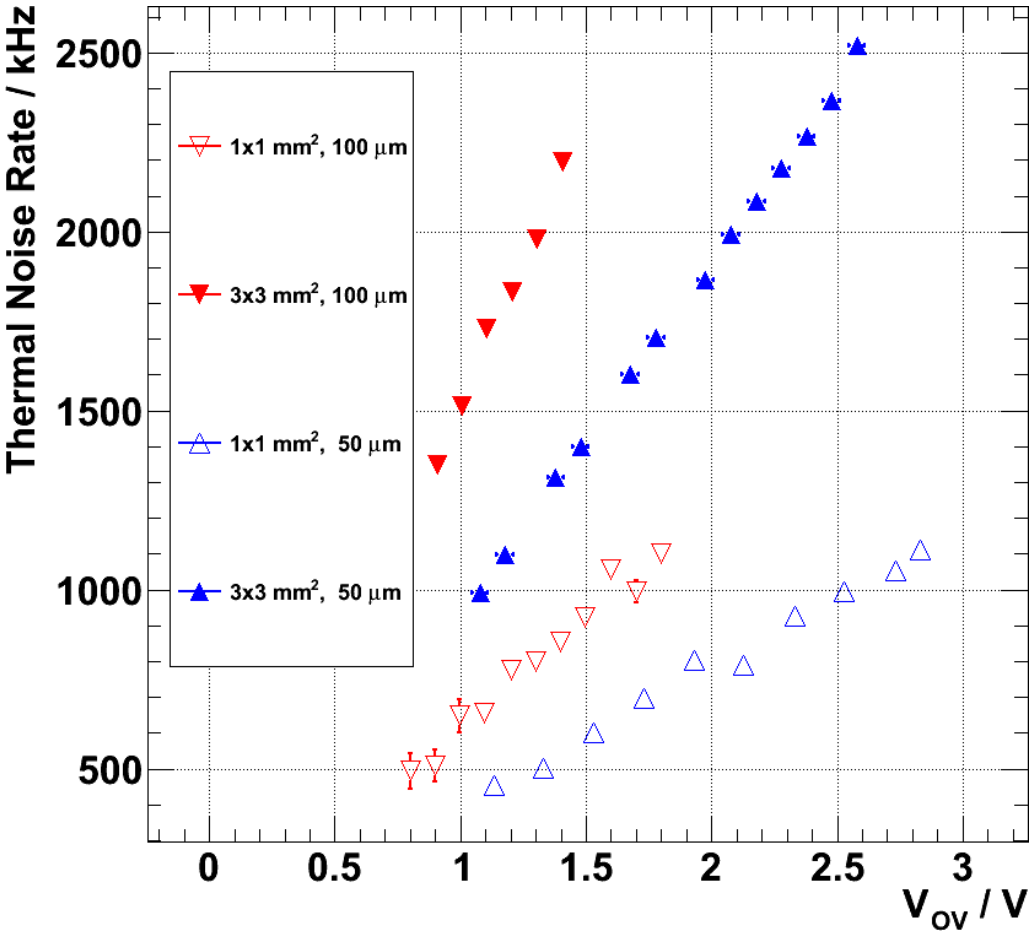

Figure 7.11: Thermal noise rate as a function of the over-voltage for different SiPM types.
(Different Temperatures for different types:
T(3x3 mm^2)=(1.0 ± 0.5) °C,T(1x1 mm^2)=(25.5 ± 0.5) °C)

.

Table 7.1: Weighted mean of after-pulse time constants and ratios of fast/slow after-pules

SiPM Type	Fast time constant	Slow time constant	Ratio fast/ slow after-pulses
1x1 mm^2, 100 µm	(43.5 ± 0.9) ns	(122.1 ± 4.5) ns	1.07 ± 0.10
3x3 mm^2, 100 µm	(44.6 ± 2.4) ns	(127.0 ± 10.3) ns	0.80 ± 0.11
1x1 mm^2, 50 µm	(20.5 ± 0.5) ns	(88.4 ± 2.6) ns	1.65 ± 0.15
3x3 mm^2, 50 µm	(22.4 ± 0.4) ns	(92.9 ± 1.9) ns	1.42 ± 0.14

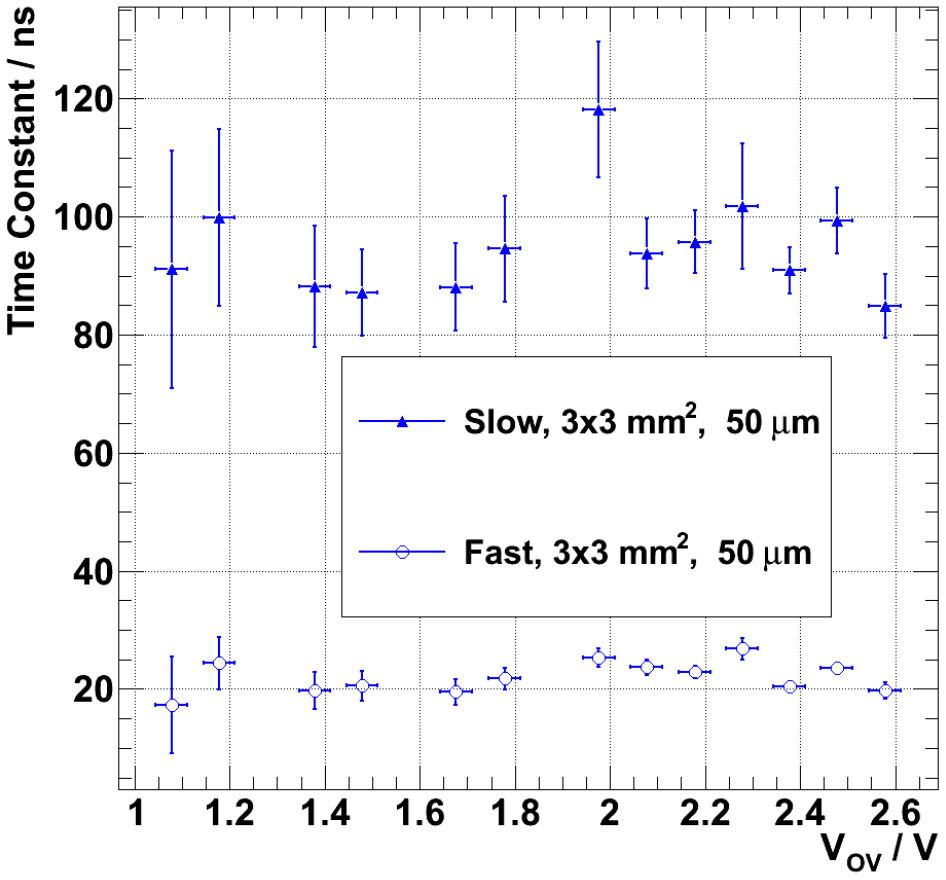

Figure 7.12: Fast and slow after-pulsing time constants as a function of the over-voltage for the 3x3 mm^2, 50 µm cell pitch SiPM type. The values of the remaining types can be found in the appendix.

into account. For an ideal SiPM without recovery the probability P_{AP} of a specific SiPM pulse having an after-pulse can be calculated from the measured data with

$$P_{\mathrm{AP}} = \frac{N_{\mathrm{ap}}}{N_{\mathrm{ap}} + N_{\mathrm{th}}} = \frac{\int_0^\infty \mathrm{dt} \cdot n_{\mathrm{ap}}}{\int_0^\infty \mathrm{dt} \cdot n_{\mathrm{ap}} + \int_0^\infty \mathrm{dt} \cdot n_{\mathrm{th}}}. \tag{7.7}$$

Here $\mathrm{N_{th}}$ represents the total number of thermal, $\mathrm{N_{ap}}$ the total number of after-pulsing events directly after the original pulse,
$n_{\mathrm{th}} := e^{(C_{TH} - R_{TH} \cdot t)}/2\,\mathrm{ns}$ and $n_{\mathrm{ap}} := (e^{(C_S - \frac{t}{\tau_S})} + e^{(C_F - \frac{t}{\tau_F})})/2\,\mathrm{ns}$. For the SiPMs at hand, this will overestimate the influence of after-pulses shortly after the original pulse, because they have a lower amplitude and consequently generate less charge per cell fired. Consequently using this probability as a correction factor for a given measurement will lead to an underestimation of the fired cells corrected for after-pulsing.
As described in [25] the cell recovery back to the original amplitude A_0 follows an

Table 7.2: Cell recovery time taken from Table 3.1 in [25], and additional uncertainty due to change of the recovery time with the over-voltage

SiPM Type	Cell recovery time	Additional uncertainty
1x1 mm^2, 100 µm	(41.1 ± 1.3) ns	± 4.0 ns
3x3 mm^2, 100 µm	(47.5 ± 0.1) ns	± 4.0 ns
1x1 mm^2, 50 µm	(13.8 ± 0.1) ns	± 2.5 ns
3x3 mm^2, 50 µm	(19.5 ± 0.1) ns	± 2.5 ns

exponential charge curve $A(t) = A_0 \cdot (1 - e^{t/\tau_\mathrm{r}})$ with the cell recovery time τ_r[14]. To take this recovery behaviour into account formula (7.7) is modified to

$$P_\mathrm{AP} = \frac{\int_0^\infty \mathrm{dt} \cdot (1 - e^{\frac{t}{\tau_\mathrm{r}}}) \cdot n_\mathrm{ap}}{\int_0^\infty \mathrm{dt} \cdot (1 - e^{\frac{t}{\tau_\mathrm{r}}}) \cdot n_\mathrm{ap} + \int_0^\infty \mathrm{dt} \cdot n_\mathrm{th}}. \tag{7.8}$$

Here the probability-density of the after-pulses is folded with the cell recovery behaviour. In contrast to [42] the recovery behaviour is not also folded with the probability-density of the thermal noise because the vast majority of thermal noise events will not take place in the initial cell.
The cell recovery time was measured in [25] by P. Hallen and is taken from there. Unfortunately, a dependency of the recovery time on the over-voltage was observed but only explicitly measured for the 3x3 mm^2, 50 µm cell pitch SiPM type. There, a change of 2.5 ns around the stated mean value of 19.5 ns was observed in an over-voltage range comparable to the range used here. Because of this an additional uncertainty of 2.5 ns is added to the 50 µm cell pitch types with a comparable recovery time and a more conservative estimate of 4.0 ns is added to the 100 µm cell pitch types. A summary of the used recovery times and their uncertainties is listed in table 7.2.
Using these recovery times and equation (7.8) the after-pulse probability is calculated for all types. The results of the 1x1 mm^2 types can be found in figure 7.13 and for the 3x3 mm^2 types in figure 7.14. For a specific type the after-pulse probability rises roughly in quadrature with the over-voltage. This again may be understood from the behaviour of the gain and the trigger probability. Assuming that only a minority of traps are filled in the avalanche, a linear increase in the probability that a trapping occurs for a linear increase in gain can be expected. Together with a rise with the trigger probability, as is indicated by figure 7.11, this could explain the observed behaviour.

For a given cell pitch the probabilities are compatible within their uncertainties, however the larger area SiPMs measured at a lower temperature lie consistently above their counterparts. Again, this may indicate an increase of the after-pulse probability with a decrease in the temperature similar to the possible increase of the

[14]The bulk recovery is neglected here, as the cell recovery accounts for more than 90% of the recharge of the SiPM [25].

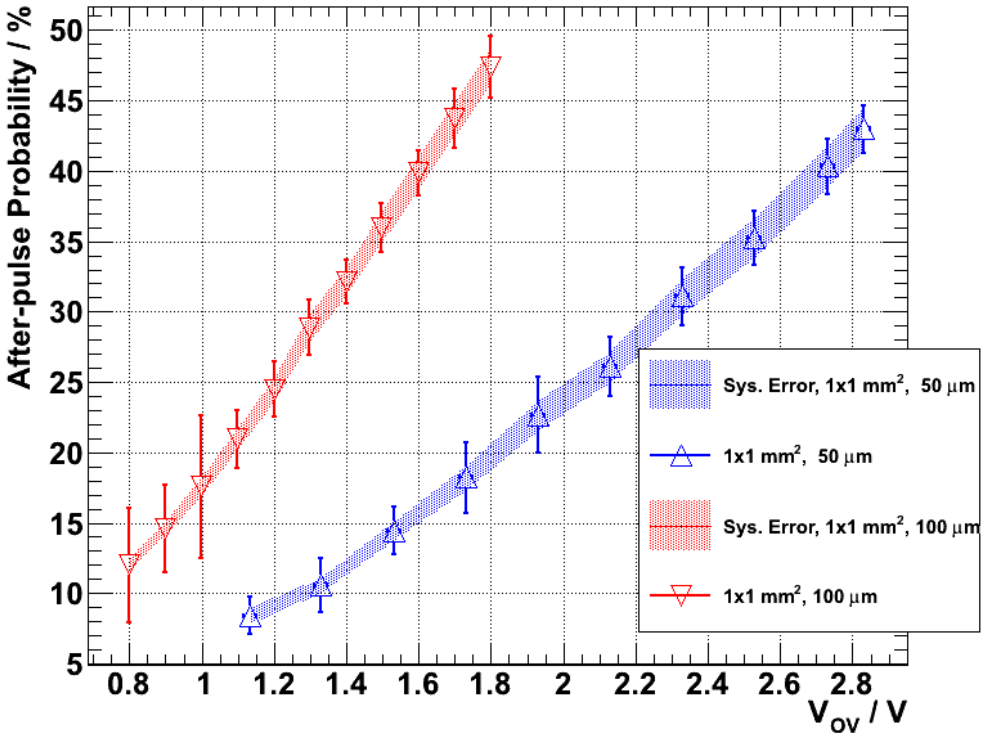

Figure 7.13: After-pulse probability as a function of the over-voltage for the 1x1 mm^2 types. Bands around the data points show the uncertainty resulting from the recovery time. The typical over-voltage lies in the 1.2-1.4 V range for the 100 µm cell pitch type and in the 1.9-2.2 V range for the 50 µm cell pitch type.

trap life time, a definite answer, cannot be given, as the the measurement was only performed at one temperature for a given type.
Finally a smaller after-pulse probability can be seen to be lower for the SiPMs with a smaller cell pitch size, likely the consequence of their smaller gain.

7.3 Discussion and Summary

In this chapter the study of two different kinds of correlated noise in SiPMs, namely optical crosstalk and after-pulsing was presented. Both were found to have a large enough influence that they may not be neglected in analyses as this could severely overestimate the number of fired cells due to incoming light.
Optical crosstalk can cause the instantaneous firing of additional cell(s) with the initial firing cell, whereas after-pulsing can cause delayed firing. The probabilities for both effects were measured as functions of the over-voltage and observed to be stable for a given over-voltage and to be rising with it. In the upper end of the stable over-voltage range of 1.1-1.4 V of the 100 µm cell pitch types the probability of a crosstalk or after-pulse event occurring was in the range of 15%-30% and 20%-33%, respectively. As both effects are smaller in the 50 µm cell pitch types the

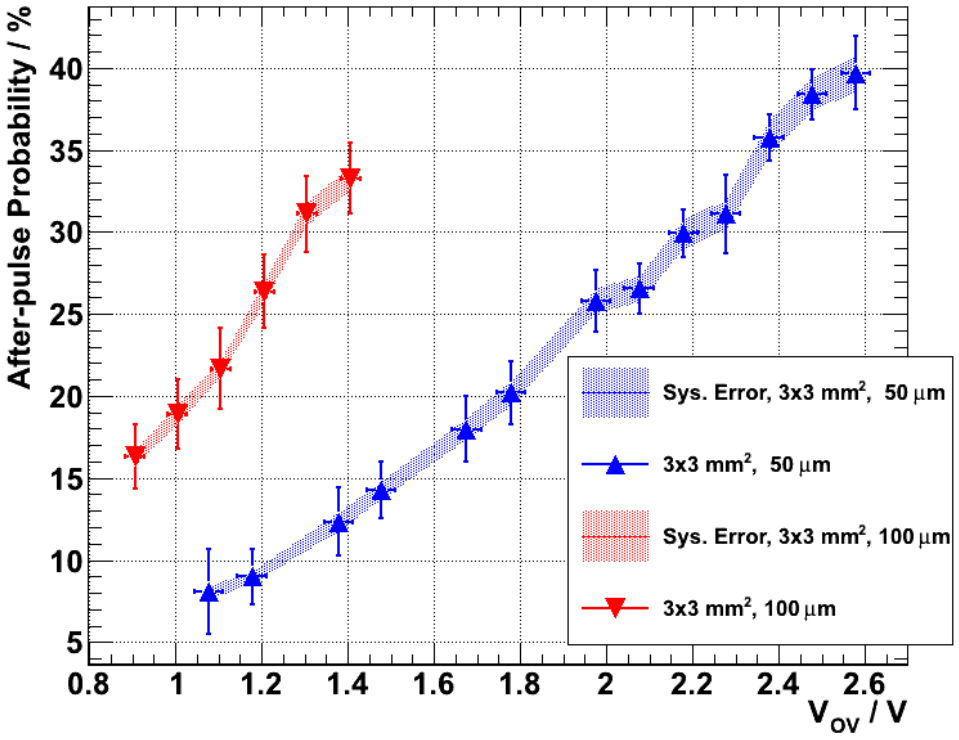

Figure 7.14: After-pulse probability as a function of the over-voltage for the 3x3 mm^2 types. Bands around the data points show the uncertainty resulting from the recovery time. The typical over-voltage lies in the 1.2-1.4 V range for the 100 µm cell pitch type and in the 1.9-2.2 V range for the 50 µm cell pitch type.

over-voltage could be increased further while the SiPMs where still operating in a stable manner, reaching comparable crosstalk and after-pulsing probabilities in the over-voltage range of 1.9-2.4 V.

For the same cell pitch, the crosstalk probability was slightly higher for the SiPMs with the larger area while the after-pulse probability was comparable, although an upwards trend was recognizable for the larger SiPMs. For all measurements the majority of crosstalk events were events with exactly one additional cell firing due to crosstalk per initially fired cell. The relative share of crosstalk events with multiple additional cells firing was observed to increase with the over-voltage.

In addition to determining the after-pulse probability, the method employed here can also be used to measure the pure thermal noise rate of SiPMs, provided that this rate does not exceed the inverse of the longest after-pulsing time constant.

In both the after-pulsing and the crosstalk measurement a cooling down to about 1 °C of the larger, and thus types with a higher thermal noise rate was required to achieve accurate results.

A method of measuring the influence of after-pulsing not requiring a cooling of the SiPM, could be achieved by using a flashed light source and a QDC with two gates.

The first, shorter gate could measure the number of originally fired cells due to the light flash and the second, longer gate the deposited charge after the first SiPM pulse has dissipated. By comparing this and the deposited charge during darkness as well as the number of fired cells, the after-pulsing probability may be calculated.
This method would have the additional advantage of discovering any long lived[15] traps, being masked by thermal noise with the presented method and also directly including the effects of cell recovery.

As both probabilities were measured and found to be stable for the same overvoltage, a correction for these effects could be performed on a statistical basis. Of help in this regard could be a Monte-Carlo (MC) simulation developed in [12], based on the measured parameters in this thesis.

[15] Longer than the inverse thermal noise rate.

8. Photon Detection Efficiency

After the characterisation studies in the previous two chapters were performed with the SiPMs situated in darkness and were concerned with the potential challenges arising from their usage, the goal of this chapter is to explore the strong point of SiPMs, namely their potentially high photon detection efficiency (PDE).
As described in chapter 3 the fluorescence light signal for a ground based fluorescence detector is very weak. Consequently the used light detector of the telescope must possess a high PDE to accurately detect showers over a large area. SiPMs are expected to reach a high PDE [18] which makes them an interesting candidate for the usage in fluorescence telescopes.
The PDE specified by the manufacturer for the 100 µm cell pitch type reaches up to 74% in the 420-450 nm range and lies above 60% for a wavelength range between 370 nm and 510 nm. According to the manufacturer, these values include the effects of crosstalk and after-pulsing, which were measured in the previous chapter. Because of this, the PDE is overestimated [22].
The goal of this chapter is to measure the PDE without these effects in a wavelength range from 375 to 460 nm. This range is chosen because it includes the range of the peak PDE, the upper half of the relevant fluorescence spectrum and light sources with these wavelengths are easily available.

8.1 Theoretical background

In general the PDE is considered to be determined by three factors [18]

$$\mathrm{PDE} = \mathrm{Q.E.} \cdot \varepsilon \cdot \mathrm{P}_{\mathrm{trigger}}. \tag{8.1}$$

Here ε is the geometric efficiency or fill factor, i.e. the ratio of sensitive area to total area. Q.E. is the quantum efficiency, defined as the probability that an incoming photon creates an e-h pair. $\mathrm{P}_{\mathrm{trigger}}$ is the probability, that the created e-h pair triggers an avalanche breakdown.
The geometric efficiency is given by the amount of dead space between the individual cells, required for cell isolation and the quenching resistors for each cell. In the case that the highest possible PDE is desired the geometric efficiency can be maximised by making the cell pitch as large as possible. This however comes with the potential drawback of increasing the thermal noise rate due to the larger, active area and increasing the cell recovery time due to the increase in the cell capacity [18]. The increase of the recovery time and the smaller number of cells consequently reduces the dynamic range in comparison to an SiPM with equal area but larger number of

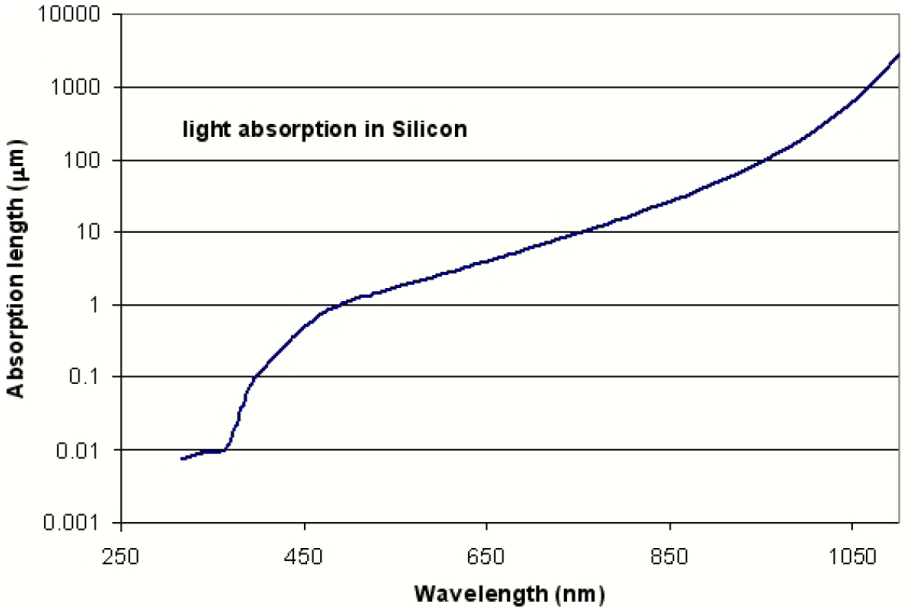

Figure 8.1: Absorption length of photons in silicon as a function of the wavelength. Taken from [18], originally from [46].

cells. Additionally the crosstalk and after-pulsing probabilities are also higher for larger cell sizes (see previous chapter).

The quantum efficiency can be further subdivided into two factors, the transmission through the transparent resin on top of the SiPM into the silicon and the internal Q.E. [45]. The relative efficiency of transmission through the resin as a function of the incidence angle was studied in [24] and found to be following the expectation set by the Fresnel equations with the relative PDE remaining above 90% up to an incident angle of 60 °. The internal Q.E. depends on the structure of the SiPM and the wavelength of the light. UV and blue light will be absorbed within the first few hundred nanometres in the silicon (or even the resin, making a very thin layer necessary) due to the short absorption length for these wavelengths as shown in figure 8.1.

As electrons have a higher probability to trigger an avalanche in silicon (see figures 4.6 and 4.5 on page 24) a p-on-n structure is preferable for the detection of short wavelengths. A potential UV sensitive SiPM cell design is shown in figure 8.2. Here incoming UV light creates e-h pairs almost only in the p layer. Because of the direction of the electrical field, the electrons drift to the high field region between the p and n layer of the silicon. If the electrons do not recombine before reaching the high field region they can trigger an avalanche. The highly doped p++ layer on top is required in this design to distribute the potential uniformly over the cell [18]. This layer needs to be very thin as the probability for a created electron to recombine is very high in the p++ region [45]. For longer wavelengths this design will have a

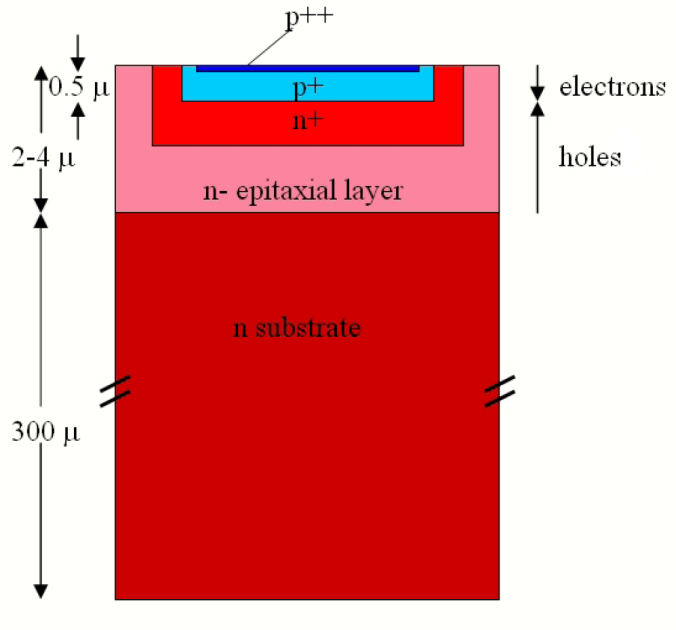

Figure 8.2: Potential UV sensitive SiPM cell structure. In this structure UV and blue light will mostly be absorbed in the p+ layer. From the created e-h pairs the electrons have a high probability of drifting to the high field region between the p+ and n+ layer and triggering an avalanche. Arrows on the right side indicate the drift direction of eletrons and holes. Taken from [18]. (The + and ++ indicate differences in doping concentrations.)

relatively lower detection efficiency, because the absorption will mainly take place in the n region with holes drifting to the high field region and triggering the avalanche.

As described in section 4.3 on page 21, the trigger probability for a given over-voltage is larger for electrons than for holes and rises with the over-voltage. This rise is to be expected to be at first linear, with saturation setting in at higher over-voltages, possibly reaching unity [19].

However, due to the increasing thermal and correlated noise at higher over-voltages of the tested SiPMs, it is uncertain whether the trigger probability will be saturated (see the results later on in section 8.4), even at the end of the usable over-voltage range.

8.2 PDE Measurement

8.2.1 Measurement Principle

The PDE of the SiPM can be measured by comparing the number of photons impinging on the active surface of the SiPM with the number of detected photons. For an ideal SiPM the number of detected photons by the SiPM could be calculated directly from the number of fired cells. For the used SiPMs this number will be

overestimated due to the effects of crosstalk and after-pulsing, discussed in the previous chapter, and thermal noise. However sometimes, provided that the used light source is not too intense, the studied SiPM will detect no light. Because crosstalk and after-pulsing can only occur when at least one cell has fired, the events where no light was detected are not affected by them. These events can then be used to calculate the average number of fired cells due to the detection of light. For this the assumption is made, that the distribution of fired cells due to the light pulses of an ideal SiPM, i.e. without crosstalk and after-pulsing, follows a Poisson distribution. The Poissonian mean can then simply be calculated from the probability that no light is detected and is expected to be the same for an ideal SiPM and an SiPM with correlated noise. A pulsed light source is required for this to allow that no after-pulse events from the previous light pulse contaminate the distribution of fired cells, i.e. classify an event where no photon from the current light pulse was detected as an event where at least one photon was detected, even though this was only an after-pulse from the previous light pulse.
The influence of thermal noise can be corrected by measuring the average number of fired cell two times. Once with the light source emitting light and once in darkness under otherwise identical conditions.

The number of photons hitting the active surface can be calculated by using a calibrated reference sensor which is exposed to the same light flux as the SiPM[1]. The reference sensor used in this measurement is a calibrated PIN diode of larger active area than the SiPM. To be able to compare the light flux on the PIN diode with the light flux on the SiPM, a circular aperture is used. During the main measurement, where the SiPM and the PIN diode are exposed to the same light flux, this aperture is placed directly in front of the SiPM. The radius of the aperture is chosen to be small enough to only expose the active area of the SiPM. After this measurement the aperture can then be placed in front of the reference sensor, which allows to compare the amount of light reaching the reference sensor during the main measurement and with the same exposed active area as the SiPM. This consequently allows to reconstruct the light flux on the SiPM surface.

The general idea for this measurement was taken from [42].

8.2.2 Measurement Setup

A schematic of the measurement setup can be found in figure 8.3. The centre of the measurement setup is an integrating sphere. Basically, an integrating sphere is a hollow, spherical cavity, with the interior covered with highly diffuse material. The purpose of an integrating sphere is to diffuse any entering light and to distribute it equally to all exit ports. As light source a selection of LEDs in a wavelength range of 375-460 nm is used. The LEDs are coupled into the integrating sphere via an optical fibre. The purpose of using the optical fibre, instead of attaching the LED directly to the sphere, is to reduce interference from the electrical pulses to the LED with the PIN diode and SiPM measurement.

[1] This is achieved with an integrating sphere and is described in the next section

The SiPM with the amplifier board[2] and the PIN diode are attached to the two remaining exit ports at the same distance. Both are connected to the sphere with two mounts, custom-made by the mechanical workshop. By default the two mounts expose the total active area of the SiPM and the PIN Diode. In addition the mount of the SiPM allows the placement of a circular aperture directly over the active SiPM area. The aperture was also manufactured at the mechanical workshop and has a diameter of 0.5 mm. An image of the integrating sphere with attached instruments and the SiPM mount and aperture can be seen in figure 8.4. Due to the design of the mount and the aperture, the centre of the aperture is automatically placed over the centre of the active SiPM area. Since the area of the aperture is smaller than the active area of the characterised SiPMs and the mounting allows for exact placement over the SiPM, only the active area of the SiPM is exposed during the measurement by the aperture.
Because of this, the aperture determines the amount of light reaching the SiPM. By placing the aperture in front of the PIN diode and comparing the amount of light reaching the PIN diode with and without the aperture afterwards, a correction factor for the different active areas of SiPM and PIN diode can be calculated. In the analysis, this then allows to reconstruct the light flux on the exposed active area of the SiPM during the main measurement from the light flux on the PIN diode without aperture. Both the PIN diode and the SiPM are not attached directly to the sphere but at the end of two tubes with a length of 1/2" to prevent any light coming directly from the fibre, not yet sufficiently diffused, to hit the active area of the sensors.

The integrating sphere with the attached instruments itself is located within a dark box with the signal cables and the optical fibre are feed outside via a light-tight front panel as shown in figure 8.3. As the current coming from the PIN diode is expected to be very small, the diode is connected to a picoammeter[3]. In such a setup the PIN diode is commonly operated at a small bias voltage [48]. As the calibration of the PIN diode was performed without any additional bias voltage [49], no reverse bias is applied here.

The amplified SiPM signal is measured by a QDC[4], which is accessible via a Wiener VM-USB module [29]. The flashing of the LEDs is performed with a pulse generator[5]. To emit one pulse the generator needs a trigger signal. This is provided over a coincidence module by one of the two programmable NIM outputs of the VM-USB module, both of which provide a NIM pulse of chosen width and frequency [29]. The same output is also used as a gate for the QDC. To ensure that the QDC captures the SiPM response to the light pulse, the length of the signal cable from the SiPM to the QDC is adjusted until the SiPM response lies well within the gate (see figure 8.5). To correct the measurement for the thermal noise of the SiPM, a dark measurement, otherwise under the same conditions but with the LED switched off, is required. For this the second NIM output of the VM-USB module is used. If enabled, a second

[2]Described in section 5.1, page 31. The version with the micro-controller is used.
[3]Keithley Picoammeter 6485, [47]
[4]CAEN V965, described in section 5.1, page 32
[5]HP 8082A

trigger signal is emitted, enabling the transfer of the first trigger signal over the coincidence. If the second output is disabled the signal from the other output still provides a gate for the QDC, but does not cause a flashing of the LED. In this case the gate can be considered to be a random gate for the QDC.
The SiPM amplifier is supplied with its operating and the bias voltage by a single NIM module 'APDPI 2.0', developed at the electronic workshop of III. Phys. Inst. B, RWTH Aachen University which allows access to the USB interface of the board.

In the following all important measurement parts, not already included in section 5.1, pages 31-33, are described in more detail.

LEDs

Four different UV/blue LEDs were used, with wavelengths of 375, 390, 405 and 465 nm specified by the manufacturer with varying tolerances. To measure the actual peak emission wavelengths and spectral widths, all LEDs were characterised with a fibre spectrometer[6]. Of all used LEDs, the respective peak emission wavelength and FWHM was measured and the results can be found in table 8.1.

PIN diode: Hamamatsu S9195

The PIN diode is used as the reference sensor. When photons are absorbed by the diode, a current proportional to the photon flux is generated and this can be used to reconstruct the flux.
Basically a PIN diode is a semiconductor p-n junction (see section 4.2 on page 19), with an intrinsic layer sandwiched between the p- and the n-layer [16]. This arrangement maximizes the quantum efficiency, and typical detection efficiencies lie in the region of 80%, with the sensitive wavelength region depending on the used layout and semiconductor [18]. In contrast to SiPMs or avalanche diodes, PIN diodes have no intrinsic amplification. Because of this a high light flux is required to produce a signal that is measurable in practise with the used setup. Since the light output per pulse is limited in this measurement by the requirements of the SiPM analysis (see later on), a large enough flux can be achieved by a sufficiently high pulse rate of the LED.
In order to use the diode as a reference sensor a calibration is necessary which was performed by the manufacturer. An overview of the quantum efficiencies for the wavelengths of the used LEDs, as given by the calibration sheet and calibration accuracy can be found in table 8.1. The active detection area of the diode is 5x5 mm.

Keithley Picoammeter 6485

As the name suggests the Keithley picoammeter is an ampere-meter, designed to measure small currents down to the pico-ampere level. The picoammeter features eight measurement ranges each with a maximum value from 20 mA down to 2 nA. As the currents occurring in this measurement are usually of the order of 100 pA the 2 nA measurement range is used at all times. In this measurement range the

[6] Ocean Optics, Red Tide USB650UV

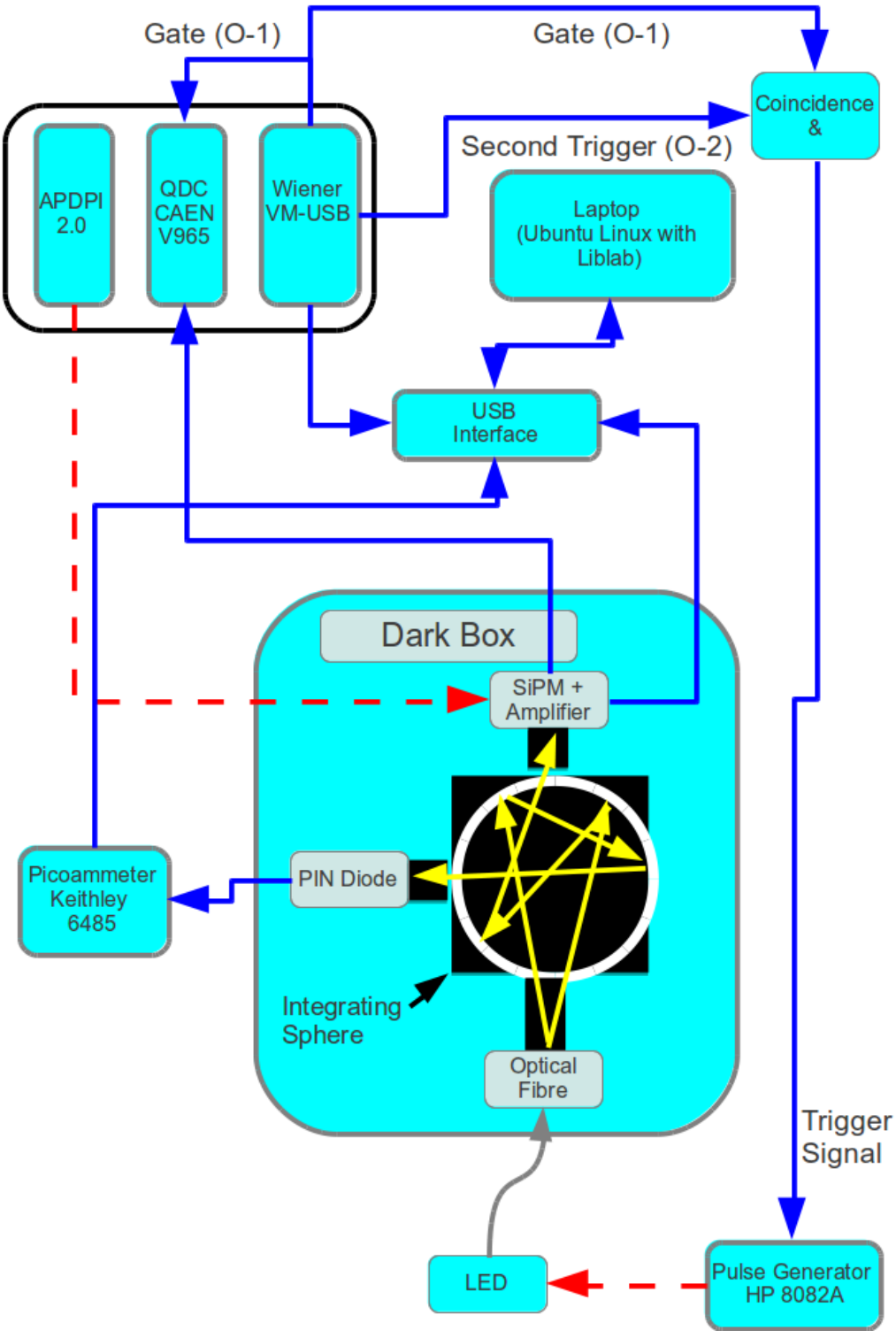

Figure 8.3: PDE measurement schematic. Data and signal cables are marked in blue (solid), power supply cables in red (dashed). The QDC is connected to the internal VMEbus of the crate which is accessible via the VM-USB module. NIM output O-1 of the VM-USB module provides the gate for the QDC. Provided output O-2 emits a second trigger, the signal from O-1 also triggers the pulse generator once per trigger causing the LED to emit one light pulse, otherwise the O-1 signal can be considered a random gate for the QDC. In the actual measurement the port with the optical fibre does not face any of the other ports directly, here it is only shown at this position for reasons of illustration.

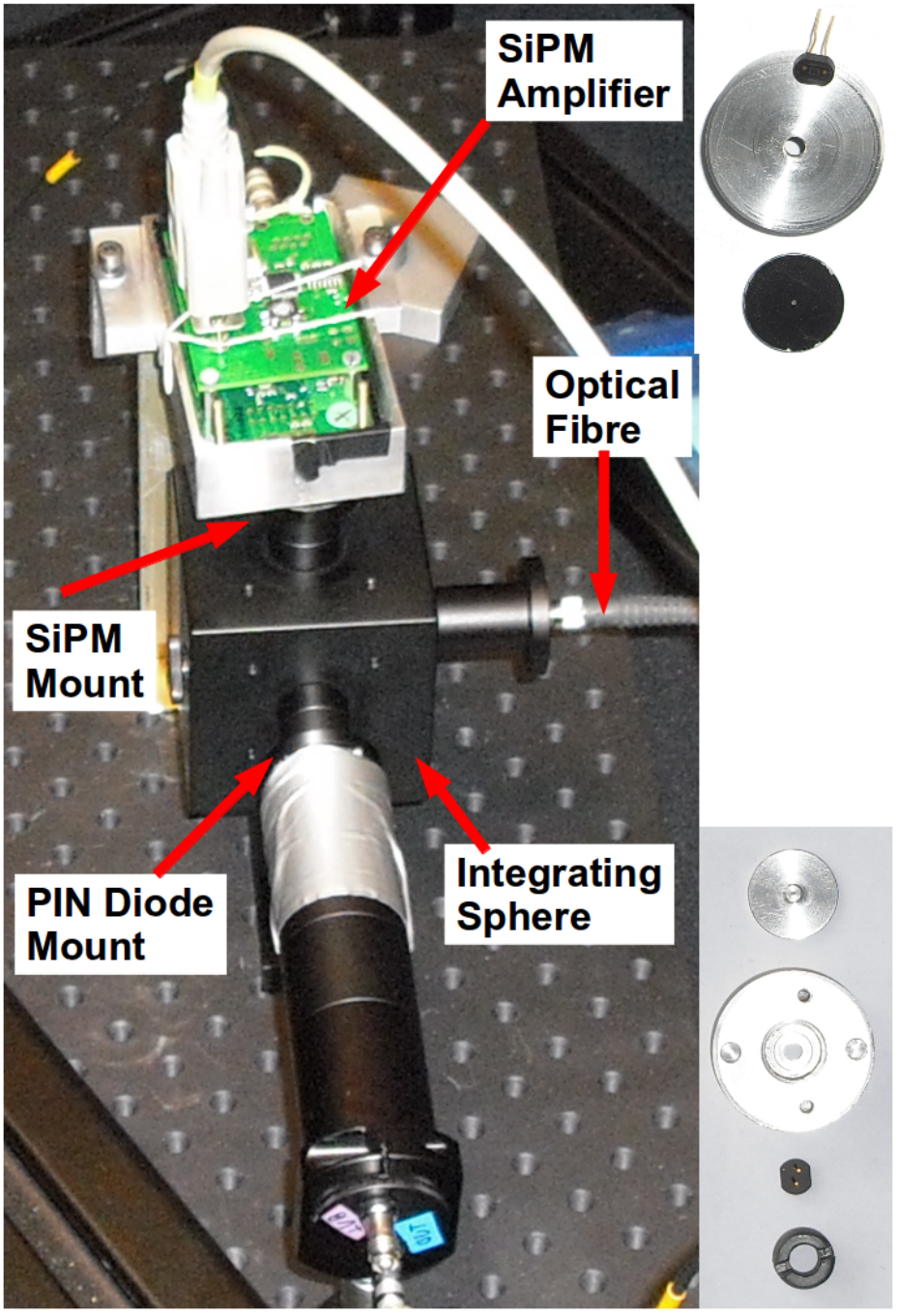

Figure 8.4: Left pane: PDE measurement setup in dark box. Attached to the integrating sphere in the centre are the SiPM and its amplifier board (on the top), the PIN diode and the PIN diode casing (front), and the optical fibre feeding the light from the LED into the sphere (right side). Right pane, Top/Bottom: Front/back side of the SiPM, SiPM mount, aperture and the SiPM retaining ring. The small cylinder on the backside of the aperture is of the same size as the circular opening of the mount, forcing the opening of the aperture to be centred in the middle of the mount. The groove in the backside of the mount always forces the SiPM in the same position, with the active area being centred in the middle of the opening of the mount and aperture.

Table 8.1: Parameters used to calculate the light flux on the SiPMs surface. (Wavelength represents the measured peak LED wavelength, Q.E. the quantum efficiency of the PIN diode (the given uncertainty is due to the change of the Q.E. over the spectral width of the LED), Accuracy the relative accuracy of the calibration of the PIN diode by the manufacturer [49], R is the correction factor for the different exposed areas of PIN diode and SiPM)

LED Type	Wavelength	FWHM	Q.E. / %	Accuracy	R
465 nm	459.2 nm	28.4 nm	88.1 ± 0.5	5 %	(209.4 ± 2.0)
405 nm	401.6 nm	13.6 nm	82.6 ± 1.0	5 %	(215.8 ± 5.0)
390 nm	391.0 nm	11.0 nm	77.9 ± 2.4	10 %	(216.1 ± 3.0)
375 nm	375.7 nm	13.4 nm	69.5 ± 6.0	10 %	(223.3 ± 3.2)

picoammeter has a resolution of 10 fA and an accuracy of ±(0.4% rdg.[7] + 400 fA) [47]. Before the ampere-meter reaches the stated accuracy a warm up time of at least one hour is required, and this is observed at all times. Internally the ampere-meter integrates over the incoming current for a certain amount of time before reporting a new average of the current in the integration time. The integration time can be set in multiples of the power line frequency. To minimize the reading noise the 'slow' measurement mode is selected, which integrates over 5 power line cycles i.e. 100 ms. The device possesses a RS-232 interface over which it can be controlled and the measured data can be read remotely.

8.2.3 Measurement Procedure

Before a measurement of a specific SiPM, the surface is cleaned with Isopropanol and a cloth to ensure maximum light detection efficiency. To be able to compare the light flux on the diode with the flux on the SiPM, first only the PIN diode is attached to the integrating sphere with the SiPM port being closed by the SiPM mount with the aperture. The used LED is coupled to the fibre outside of the dark box. While the LED is still turned off, 100 current measurements are performed with the picoammeter. Afterwards the LED is turned on with a constant voltage instead of the pulsed mode, leading to a large current from the PIN diode. After the light flux from the LED has stabilized 100 current measurements are taken again. While the LED is still emitting light, the diode is quickly removed from the port where it is normally attached and the port is closed with the same diode type in a mount identical in construction. The aperture, normally located in front of the SiPM, is then put over the sensitive area of the PIN diode and the diode is attached to the port where the SiPM will be located during the main measurement. Again 100 current measurements are taken with the LED still emitting light and then again in darkness.

[7] Percentage of reading (measured value).

From this, a correction factor R for the different active areas of SiPM and diode during the main measurement can be calculated by

$$R = \frac{\Delta I_{\text{normal}}}{\Delta I_{\text{aperture}}}. \tag{8.2}$$

Here ΔI_{normal} or $\Delta I_{\text{aperture}}$ is the difference of the mean current from the diode with the LED switched on and the mean current with the LED turned off, when the total active area is exposed or the aperture is in front of the diode respectively. In order to be able to estimate the uncertainty on this manual procedure, this measurement is repeated four times for each LED before, and four times after each main measurement. The standard deviation of the eight measurements for a given wavelength is then used as the uncertainty on R. The measured values of R can be found in table 8.1. As can be seen, there may be a slight dependence of R on the wavelength. For an ideal integrating sphere this should not be the case. However, as the aperture and the PIN diode are not themselves ideal diffuse reflectors this is not unexpected. Because R is calculated with the PIN diode located at the place where the SiPM is normally located, applying the correction in the analysis should also compensate for the case, that the light entering is not distributed completely equal by the sphere.

After this measurement, the LED is turned off, the PIN diode is attached to its normal position, with the total active area exposed and the SiPM is put behind the aperture and attached to the integrating sphere as well.

Now, a reasonable over-voltage range is selected for the measured SiPM as described in section 5.2 on page 33. The SiPM is then biased at the highest over-voltage and the LED is turned on in pulsed mode. For this the trigger output from the VM-USB module is turned on, first with a low frequency. Since the analysis method requires events where no light was detected, a short pulse width of approximately 8 ns[8] is used and the amplitude of the pulse is slowly increased until the number of events where no light was detected and the number of events where at least one SiPM cell fires, are roughly equal. For this the SiPM signal is fed into an oscilloscope, and the oscilloscope is triggered by the trigger signal of the pulse generator. An example of this can be found in figure 8.5. As can be seen there are still baseline events, where no light was detected but there is also a clear correlation between the trigger output and the firing of one or more SiPM cells. Since the LEDs differ in their light output this step is repeated for every LED. The trigger signal shown in figure 8.5 is also used as the gate for the QDC. The width is chosen to be around 100 ns which should guarantee that all light coming from the LED is contained within the gate. An example of a QDC charge spectrum measured this way can be found in figure 8.7.

With this configuration the amount of light emitted per pulse from the LED is fixed. As the PIN diode has no intrinsic amplification and the measurement with the picoammeter averages over the total measurement time, the pulse rate of the

[8]This is only the pulse width of the pulse generator of the LED. The pulse width of the trigger and simultaneously QDC gate is chosen long enough, so that all SiPM signals from the light pulse can be measured. This width is shown in figure 8.5.

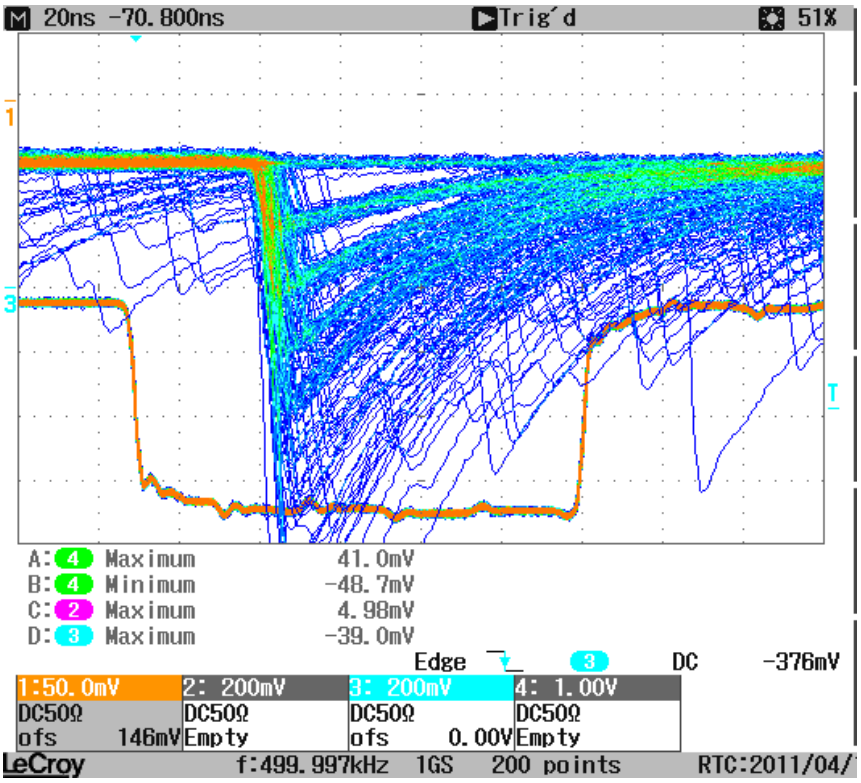

Figure 8.5: Amplified SiPM (1x1 mm^2, 100 µm cell pitch) signal (channel 1) illuminated by flashed LED. Channel 3 shows the gate of the QDC and was used as the trigger for the oscilloscope and the LED. Horizontal axis: time (1 division $\doteq$ 20 ns), vertical axis: voltage (1 division $\doteq$ 50 or 200 mV).

LED determines whether the current from the diode can be measured in a precise way or not.
Ideally the readout frequency of the QDC should not exceed approximately 10 kHz [27], however with this frequency the current from the PIN diode would be far to low for an accurate measurement. Instead a pulse frequency in the range of 200-500 kHz, depending on the LED is chosen. With this the current from the diode is large enough to be measured with a high accuracy and the time between the individual pulses is still large enough, so that no after-pulse contamination from previous pulses is expected[9].

To keep the readout of the QDC within specifications, the readout of the QDC is limited in the measurement program to about 2 kHz. As a result, the QDC measurement captures only a small fraction of the light pulses. As the analysis compares only averages this should not have any influence on the results. To compensate for a possible shift with time of the pulse generator output, the QDC and picoammeter measurement are performed simultaneously.

With all required parameters known the main measurement is started. For this the lowest over-voltage from the measurement range is applied and the NIM output

[9]See the trap lifetimes in the previous chapter on page 65.

from the VM-USB module providing the gate is turned on. Now two measurements, a 'dark' measurement with the LED off and a 'light' measurement with the second trigger enabled and consequently a flashed LED, are performed. In each of these two measurements 30.000 QDC values and 100-110 picoammeter current values are measured simultaneously, with the picoammeter measurement being terminated when the QDC measurement is ended.

The over-voltage is then increased and the measurement repeated until the total over-voltage range has been scanned. As in the previous chapters the measurement is controlled by a self written C++ program, with the information saved in ROOT files [34] and the access to the measurement instruments is provided by the LibLAB library [30].

8.3 Analysis

The PDE of the SiPM at a given wavelength can be calculated from the mean number of fired cells μ due to photons from the light pulse and the average number of photons μ_{ref} per pulse impinging on the SiPM by [42]

$$PDE = \frac{\mu}{\mu_{\text{ref}}}. \tag{8.3}$$

These two parameters are determined in the following two paragraphs.

8.3.1 Picoammeter Analysis - Photons Impinging on the SiPM Surface

An example of a current distribution coming from the illuminated PIN diode is shown in figure 8.6. As can be seen the values coming from the picoammeter follow a Gaussian distribution and consequently the error of the mean is used as the statistical uncertainty for all measured mean currents.
By subtracting the mean current I_{Dark}, measured with the LED turned off, from the mean current I_{Light} with the LED turned on, the average current due to the light from the LED, $\Delta I = I_{\text{Light}} - I_{\text{Dark}}$ can be calculated. Since the used dark box was light-tight and no bias voltage was applied I_{Dark} fluctuates around zero. Nevertheless this correction is applied to correct for a possible offset in the picoammeter. By dividing ΔI by the elementary charge e and the quantum efficiency $Q.E.$ of the PIN diode at the peak emission wavelength of the used LED, the average number of photons per second hitting the active area of the diode is obtained. Further dividing by the frequency of the pulse generator trigger f_{Pulser}, and by the geometrical correction factor R, calculated with equation (8.2), results in the average number of photons impinging on the active SiPM surface per pulse

$$\mu_{\text{ref}} = \frac{\Delta I}{e \cdot Q.E. \cdot f_{\text{pulser}} \cdot R}. \tag{8.4}$$

The two dominating systematic uncertainties of μ_{ref} come from R, which was calculated in the previous section, and the quantum efficiency. Two effects contribute to

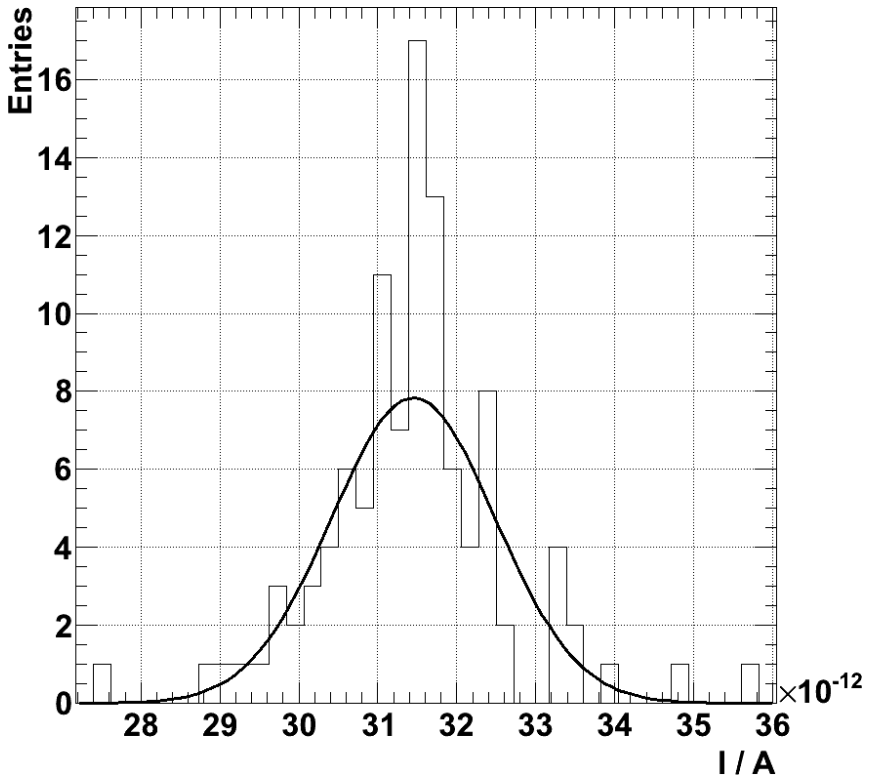

Figure 8.6: Current from the PIN diode, measured with the picoammeter. Current due to flashed LED of approx. 8 ns pulse width, a flashing frequency of 200 kHz, and a peak emission wavelength of 391 nm. The fit function is a Gaussian.

the uncertainty of the quantum efficiency. The first is the calibration accuracy given by the manufacturer. This accuracy is stated to be 5% relative for wavelengths over 400 nm and 10% relative for wavelengths below 400 nm [49]. The second effect is due to the change of the quantum efficiency over the spectral width of the LED. The uncertainty from this is estimated from the change of the quantum efficiency at the peak emission wavelength of the LED[10] to the quantum efficiency at FWHM.
For the analysis both uncertainty contributions are linearly added. The uncertainty from the calibration is the dominating uncertainty, except for the 375 nm LED where both influences contribute roughly equal. A summary of the used quantum efficiencies, the geometrical correction factors and associated uncertainties can be found in table 8.1 for all LED wavelengths.

8.3.2 QDC Analysis - Fired Cells due to Impinging Photons

An example of a deposited charge spectrum from an illuminated SiPM can be found in figure 8.7. Each peak corresponds to a certain number of cells firing while the gate of the QDC is open (see figure 8.5). Because the light level of the LED was set in a way to allow for events where no light is detected to occur, the first of the peaks

[10]Obtained by linear interpolation between the two closest given values by the manufacturer.

in the spectrum is the pedestal. This corresponds to the baseline events visible in the oscilloscope screen-shot in figure 8.5.
For an ideal SiPM without thermal noise, optical crosstalk, and after-pulsing each peak would correspond to a certain number of detected photons in a given pulse. Neglecting thermal noise for the moment, the introduction of crosstalk and after-pulsing distorts the spectrum, as they cause additional cells to fire, when at least one cell has fired from the detection of light. Because both crosstalk and after-pulsing are correlated noise, the pedestal is expected to be not affected since no light has been detected.
Consequently the number of pedestal entries in the distribution of an ideal, and an SiPM with correlated noise should be the same. Under the assumption, that the ideal distribution follows a Poission distribution, the mean number of fired cells[11] μ can be calculated from the probability $P(\mu, 0)$, that no light has been detected (i.e. no cell breakthrough has occurred) by

$$\begin{aligned} P(\mu, k) &= \frac{\mu^k e^{-\mu}}{k!} && (8.5)\\ \Rightarrow P(\mu, 0) &= e^{-\mu} && (8.6)\\ \Rightarrow \mu &= -\ln(P(\mu, 0)) && (8.7)\\ \Rightarrow \mu &= -\ln\left(\frac{N_{\text{ped}}}{N_{\text{tot}}}\right). && (8.8) \end{aligned}$$

Here k is the number of occurrences of events, and $P(\mu, 0)$ is given by the ratio of pedestal events N_{ped} and the total number of measured events N_{tot}. If μ is calculated with this method, it is expected to be identical for an ideal, as well as for the SiPMs at hand.
To determine N_{ped} all events in the charge distribution up to the 0.5 p.e. level are counted as pedestal events (see image 8.7). N_{tot} is the integral over the total distribution. The statistical uncertainty of $P(\mu, 0)$ is given by the binomial error

$$\sigma_{P(\mu,0)} = \frac{1}{N_{\,\text{tot}}} \cdot \sqrt{N_{\text{tot}} \cdot p\,(1-p)}, \tag{8.9}$$

with the estimate of p= $\frac{N_{\text{ped}}}{N_{\text{tot}}}$.
As the pedestal and the first photon peak are not totally separated and start to overlap at higher over-voltages, the systematic uncertainty of the number of pedestal events is estimated by setting the counting threshold to 0.3 p.e. and 0.7 p.e..

μ now represents the average of fired cells due to the detection of incoming photons, without the effects of optical crosstalk and after-pulsing.
In contrast to these effects, thermal noise can also affect the pedestal events. To correct for thermal noise, the Poissonian mean is calculated two times. In one case μ_{light} for the measurements with the LED flashing and in the other case μ_{dark} for the corresponding measurement under the same conditions, but with the LED turned off.

[11] For an ideal, as well as for the SiPMs at hand.

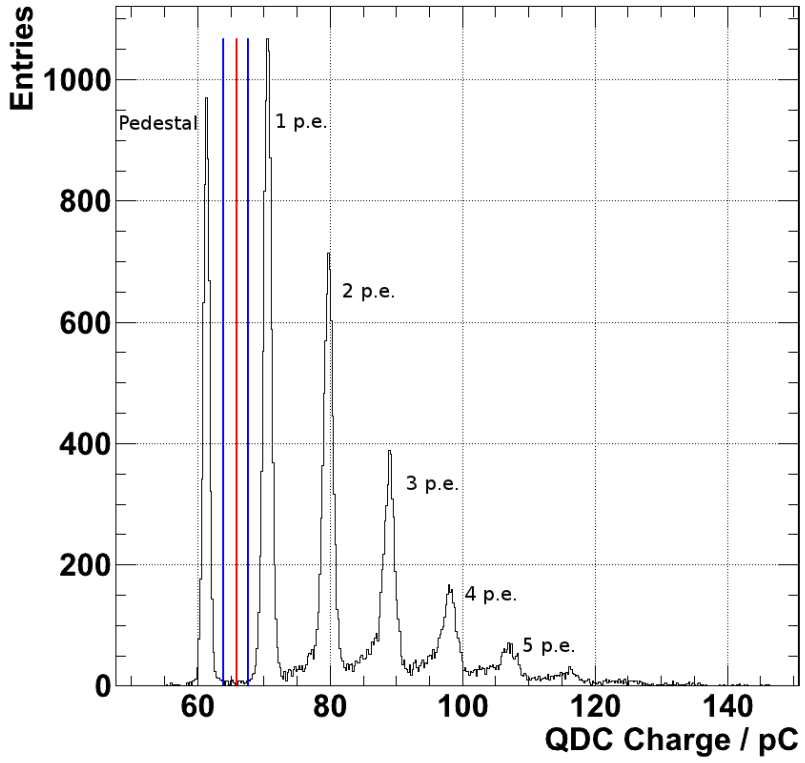

Figure 8.7: QDC spectrum of an illuminated SiPM. The first peak is the pedestal, where no light was detected from the light source. The following peaks correspond to a specific number of fired cells. Up until the red (inner) line, located at 0.5 p.e. the events are counted as pedestal events. The blue (outer) lines, located at 0.3 and 0.7 p.e. are used to estimate the uncertainty of the number of pedestal events. ($1\text{x}1\,\text{mm}^2, 50$ µm cell pitch, $V_{OV}= (1.142 \pm 0.02)$ V)

Finally the average of fired cells, only due to the detection of photon(s) from the LED is given by [42]

$$\mu = \mu_{\text{light}} - \mu_{\text{dark}}. \tag{8.10}$$

8.4 Results - PDE

Using the results from the previous analysis steps, the PDE is calculated with equation (8.3). The results for the 1x1 mm^2, 100 µm cell pitch type at a wavelength of 460 nm is shown in figure 8.8. Like in the crosstalk and after-pulse measurements an increase of the PDE with the over-voltage is observed. This is most likely due to an increase of the trigger probability and maybe additionally due to an increase

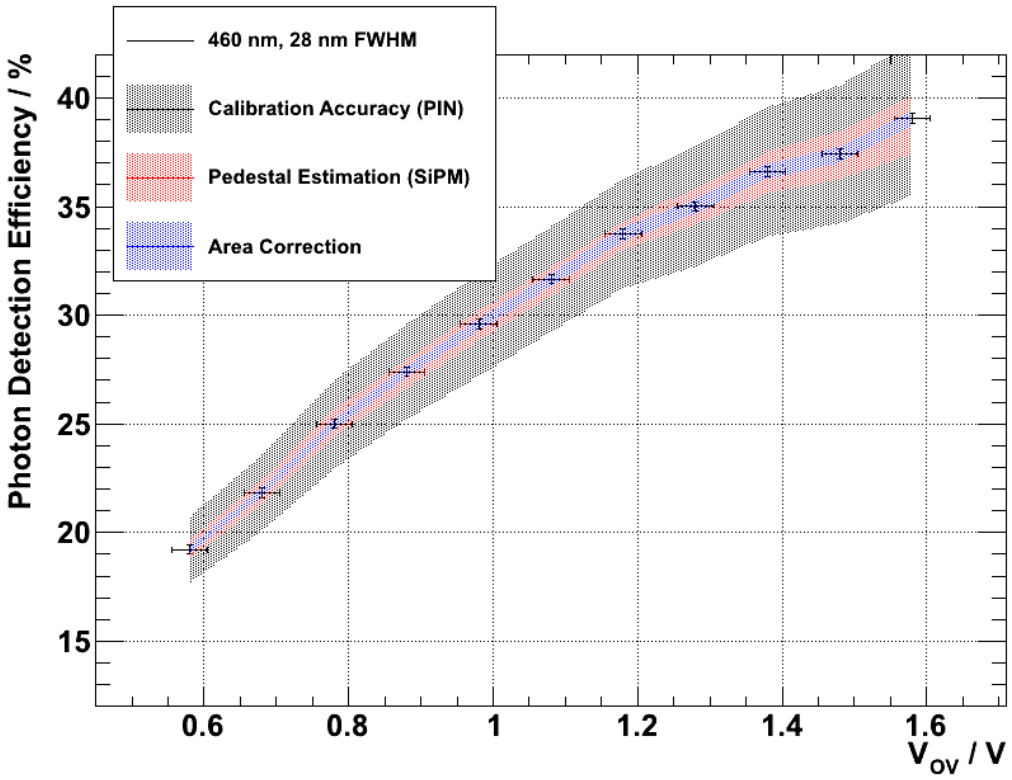

Figure 8.8: Photon detection efficiency at LED peak emission wavelength of 465 nm of the 1x1 mm^2, 100 µm cell pitch type. Bands specify systematic uncertainties due to: 1) The calibration accuracy of the PIN diode and the change of the Q.E. over the LED spectral width (black, outer band), 2) the accuracy with which the pedestal events in the QDC SiPM charge spectra can be identified (red, middle bands), and 3) the measured correction factor for the different active areas of PIN diode and SiPM (blue, inner band). The typical over-voltage lies in the 1.2-1.4 V range for this type.

of the quantum efficiency, caused by an increase of the size of the drift region (see equation (8.1)). At an over-voltage of[12] (1.38 ± 0.02) V the PDE is

$$36.5\% \pm 0.3\% \text{ (stat.)} \pm 3.0\% \text{ (sys.)}.$$

Here, as well as in all other measurements, the systematic uncertainties dominate the measurement. The largest contributor to the systematic uncertainty comes from the calibration accuracy of the PIN diode. As can be seen, the uncertainty due to the estimation of the pedestal entries increases with the over-voltage. This is because the peaks in the charge distribution begin to overlap at higher over-voltages.

A summary of the PDEs for all wavelengths can be found in figure 8.9 for the 50 µm and in figure 8.10 for the 100 µm cell pitch types.The systematic uncertainty bands

[12]Representing the end of the range, where stable operation is possible.

have been excluded from the summary plots for reasons of visibility. The results including the systematic uncertainties, for all characterised SiPMs and wavelengths can be found in the appendix.

The results of the PDE measurement only include the 1x1 mm^2 types. The 3x3 mm^2 types could not be characterised successfully, because the thermal noise rate was too high due to the fact, that the measurement was performed during the summer and in a laboratory without temperature control. The large noise rate, in addition to an issue with the amplifier which caused an unstable baseline for SiPM signals of a high (thermal) rate, resulted in QDC charge spectra which could not be analysed reliably.
This issue may be resolved, by measuring at a lower temperature, the use of a different amplifier or the usage of an FADC[13] instead of a QDC for the SiPM measurement.
Because the fill factor and the pitch size of the corresponding 3x3 mm^2 types is the same [22], as for the 1x1 mm^2 types, the PDE is expected to be the same for these types as well. Apparently there is a difference between the peak PDE values, including crosstalk and after-pulsing, of up to 74%, given by the manufacturer and the results shown here. The exact measurements conditions of the manufacturer are not known, making a comparison difficult. However, as shown in table 4.1 on page 28, the manufacturer states a PDE of 65% for the 100 µm cell pitch, 1x1 mm^2 type, at a wavelength of 440 nm and at the recommended bias-voltage and temperature. From the measurements in chapter 6 this can be translated to an over-voltage between 1.2 V and 1.3 V. There, the measured PDE at the nearest wavelength of 460 nm is between 34%-35%. This corresponds to a difference of a factor 1.9. Under the assumption, that the measurement of the manufacturer includes all crosstalk and after-pulse events and only a relative small number of cells fires initially, an estimate of the overestimation due to these effects is made here: At an over-voltage of 1.2 V the after-pulse probability is 24.5%, and the crosstalk probability is 20% with an average of 1.25 additional cells firing per crosstalk event (see the results from chapter 7).
If a certain number n_0 of cells fire due to the detection of light, an average of $0.25 \cdot n_0$ additional cells will fire due to crosstalk, a total of $1.25 \cdot n_0$. Of these an average of $0.30 \cdot n_0$ cells will fire again, due to after-pulsing. Again additional cells will fire due to crosstalk, and all of the events can have additional after-pulses and so on. This series quickly converges and, on average a total of $1.7 \cdot n_0$ cells fire for a firing of n_0 cells, due to the detection of light. Repeating the same calculations for an over-voltage of 1.3 V gives an overestimation factor of 1.9. As can be seen, including the effects of crosstalk and after-pulsing into the PDE, all measured in this thesis, can account for the difference between the achieved results with the manufacturer specifications under the made assumptions.
As stated, the general measurement setup and idea were taken from [42]. There, the

[13] Since the available FADC could not be triggered reliably this has not been performed.

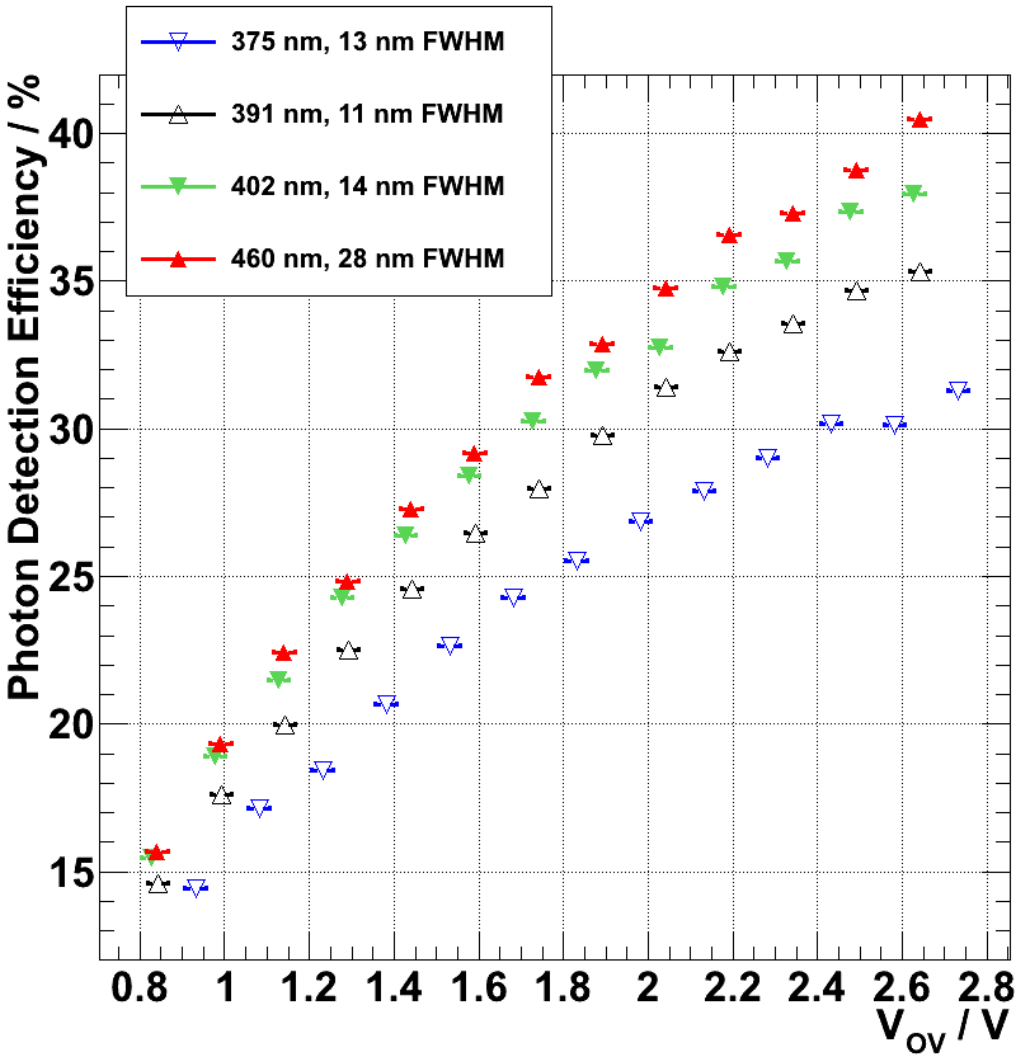

Figure 8.9: Photon detection efficiency of the 1x1 mm^2, 50 µm cell pitch type. The legend specifies the peak emission wavelength of the LEDs and FWHM. The typical over-voltage lies in the 1.9-2.2 V range for the 50 µm cell pitch type.

PDE was also measured for the types studied here. Within the uncertainties, the results from this work and the results in [42] are in good agreement.

8.5 Discussion and Summary

In this chapter the PDE was measured for two SiPMs types, one with a cell pitch of 100 µm and one of 50 µm and at four different wavelengths of 375, 390, 402 and 460 nm. At the end of the stable over-voltage range, with an over-voltage of 1.4 V the PDE was found to be in the range of 28 - 36 % for these wavelengths and the 100 µm

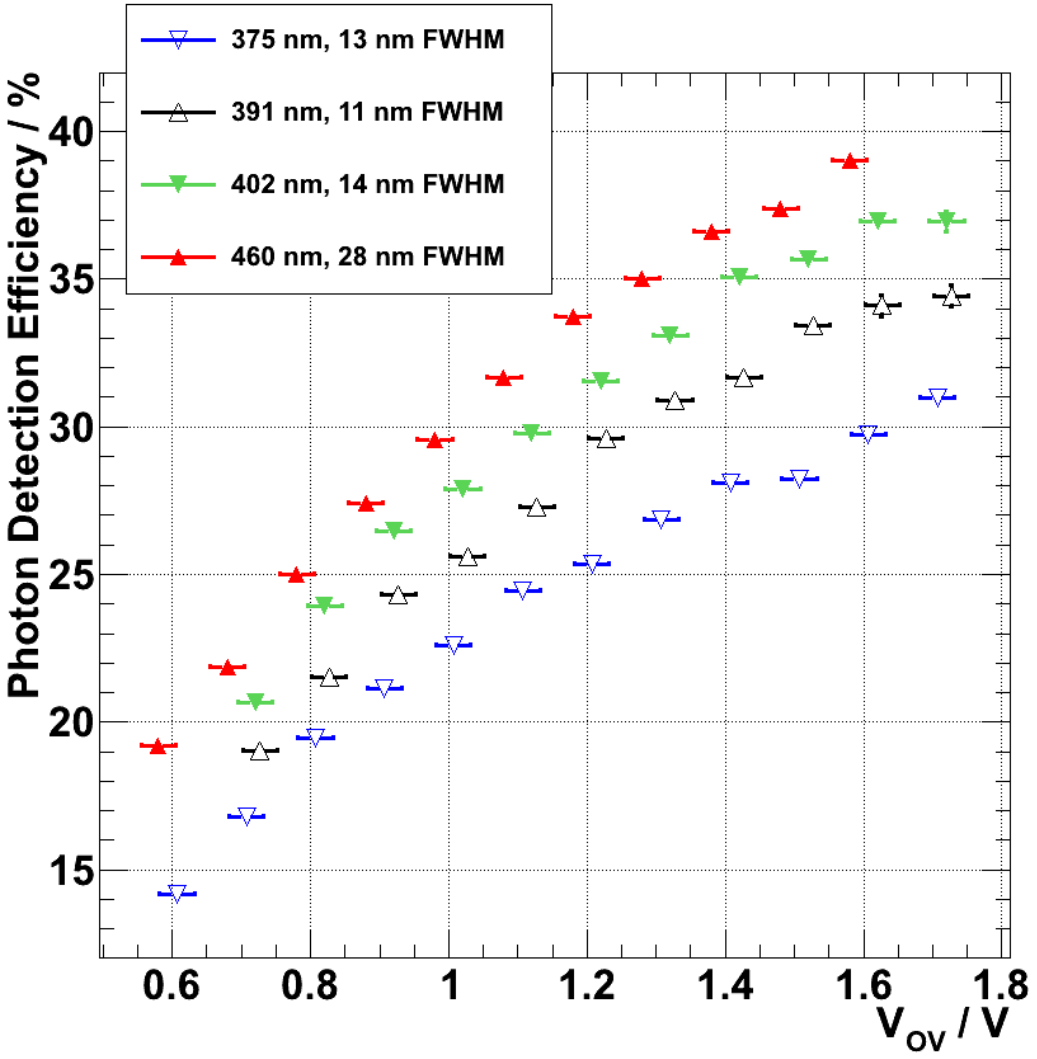

Figure 8.10: Photon detection efficiency of the 1x1 mm^2, 100 µm cell pitch type. The legend specifies the peak emission wavelength of the LEDs and FWHM. The typical over-voltage lies in the 1.2-1.4 V range for the 100 µm cell pitch type.

cell pitch type. For the 50 µm pitch the over-voltage could be further increased[14], and the PDE reached similar values above an over-voltage of 2.1 V.
In both cases the observed peak value is at the largest wavelength in the range and the PDE drops with the wavelength, indicating a peak PDE in the range of 420-460 nm as stated by the manufacturer [22].
The dominating uncertainty contribution of this measurement comes from the calibration accuracy of the used reference sensor of 5% for wavelengths above 400 nm and 10% for wavelengths below 400 nm.

[14] As can be seen from the results of chapter 7, these effects of thermal noise, optical crosstalk and after-pulsing are smaller for the smaller pitch, at the same over-voltage. This allows stable operation at higher over-voltages.

In comparison to e.g. the currently used PMTs of the fluorescence detector of the Pierre Auger Observatory with an average quantum efficiency of about 30% [8] in a similar wavelength range, the tested SiPMs reach comparable and even higher values. This already makes SiPMs candidates of interest for the detection of the weak fluorescence light signal from extensive air showers. It should be noted however that, at least currently, the peak PDE lies relatively far in the blue rather than in the UV and a change in some SiPM design parameters, e.g. a thinner transparent entrance material and optimization of the size of the p and n regions[15], would be preferable. In addition further improvements may be expected, as the manufacturing process matures, and a reduction of thermal noise, crosstalk and after-pulsing allows for the operation at higher over-voltages. As can be seen in figures 8.10 and 8.9 the PDE is still increasing with the over-voltage, i.e. the trigger probability appears not to be saturated, but the noise effects make operation at higher over-voltages currently not advisable or even possible.

[15] See the theoretical introduction to this chapter.

9. Summary and Outlook

The study of ultra-high-energy cosmic rays (UHECRs) is a vivid and also challenging field. Due to their low flux, large ground based observatories are required for their study. One powerful technique to study UHECRs by means of ground based detectors is fluorescence detection of extensive air showers. This technique requires very efficient light detectors. Currently, mainly photomultiplier tubes are used for this purpose. The usage of silicon photomultipliers (SiPMs) may improve this technique.

Extensive characterisations studies of SiPMs were presented in this work. The aim of the studies was to explore potential advantages and challenges of using SiPMs as light detectors in fluorescence telescopes.

The first explored issue was the dependence of the breakdown voltage, and consequently the over-voltage on the temperature. A linear dependence of the breakdown voltage on the temperature was observed with a constant of proportionality of 56 mV/K. As a stable over-voltage is required for many applications a method is needed to keep the over-voltage stable. One way to achieve this is to monitor the temperature and to adjust the bias voltage accordingly. An automatic implementation of this method has been tested and found to keep the over-voltage sufficiently stable over a wide temperature range.

Another challenge of using SiPMs is their correlated noise in the form of optical crosstalk and after-pulsing. Optical crosstalk causes the simultaneous firing of other cell(s) for the firing of an initial cell while after-pulsing causes delayed firing. At the upper end of the usual over-voltage range the probability of a crosstalk or after-pulse event to occur is in the range of 15%-30% and 20%-33%, respectively. In the majority of crosstalk events only one additional cell is fired. Two different after-pulsing time constants were observed, a short one of a few tens of nanoseconds and a longer one of about 100 ns. The crosstalk and after-pulsing probabilities were measured over a wide over-voltage range and were found to be stable and to only depend on the specific over-voltage, theoretically allowing a correction for these effects.

The photon detection efficiency (PDE), *not* including the effects of correlated noise, was measured at four different wavelengths of 375, 390, 402 and 460 nm. The observed peak PDE is 36% at 460 nm and the PDE is generally in the range of 28 - 36 % at the end of the usual over-voltage range. The PDE was observed to be still increasing at higher over-voltages, however the observed limitations due to thermal and correlated noise make operations at higher over-voltages currently impossible. Maturing of the manufacturing process is expected to reduce these effects, allowing operation at higher over-voltages.

The results in this work demonstrate that SiPMs already offer a competitive PDE in comparison to current fluorescence telescopes based on photomultiplier tubes. While they raise challenges in their usage, these challenges can be understood and be controlled. Additionally the manufacturing process is expected to improve, reducing the thermal and correlated noise while the PDE is expected to improve. This, in conjunction with the potential of low cost mass-production makes SiPMs very interesting candidates for the usage in future fluorescence telescopes.

The construction of a prototype fluorescence telescope is currently in progress, based on other efforts and on the results and developed methods in this work. This telescope will use SiPMs as the light sensitive component, providing further insight into this novel concept in fluorescence detection.

References

[1] M. Longair, *High Energy Astrophysics*, Cambridge University Press, 2011.

[2] J. Bluemer, R. Engel, and J. R. Hoerandel, *Cosmic rays from the knee to the highest energies*, Progress in Particle and Nuclear Physics, 63 (2009), pp. 293 – 338. Available online http://www.sciencedirect.com/science/article/pii/S0146641009000362, visited 11.27.11.

[3] W. Hanlon, *Updated cosmic ray spectrum*. Available online http://www.physics.utah.edu/~whanlon/spectrum.html, visited 11.27.11.

[4] C. Wiebusch, *Vorlesung Astroteilchenphysik*, III Phys. Inst B, RWTH Aachen, SS 2010.

[5] B. Keilhauer, *Investigation of Atmospheric Effects on the Development of Extensive Air Showers and their Detection with the Pierre Auger Observatory*, phd thesis, Universitaet Karlsruhe, Karlsruhe, 2003.

[6] K. Nakamura *et al.*, Particle Data Group, *Review of particle physics*, J. Phys., G37 (2010), p. 075021.

[7] F. Arqueros, J. R. Hoerandel, and B. Keilhauer, *Air fluorescence relevant for cosmic-ray detection. summary of the 5th fluorescence workshop, el escorial 2007*, Nuclear Instruments and Methods in Physics Research Section A: Accelerators, Spectrometers, Detectors and Associated Equipment, 597 (2008), pp. 1 – 22. Proceedings of the 5th Fluorescence Workshop.

[8] The Pierre Auger Collaboration, *The fluorescence detector of the pierre auger observatory*, Nuclear Instruments and Methods in Physics Research Section A: Accelerators, Spectrometers, Detectors and Associated Equipment, 620 (2010), pp. 227 – 251.

[9] D. J. Bird *et al.*, *The cosmic-ray energy spectrum observed by the Fly's Eye*, The Astrophysical Journal, 424 (1994), pp. 491–502. Available online http://adsabs.harvard.edu/abs/1994ApJ...424..491B, visited 11.27.11.

[10] A. Obermeier, *The Fluorescence Yield of Air excited by Electrons measured with the AIRFLY Experiment*, diploma thesis, Universitaet Karlsruhe, 2007.

[11] M. Stephan *et al.*, *Future use of silicon photomultipliers for the fluorescence detection of ultra-high-energy cosmic rays*, SPIE, 8155 81551B-1 (2011). Also available as GAP-Note GAP-2012-024.

[12] T. Niggemann, *New Telescope Design with Silicon Photomultipliers for Fluorescence Light Detection of Extensive Air Showers*, master thesis, III. Phys. Inst. A, RWTH Aachen University, to be published (2012).

[13] R. Winston, J. Miñano, W. Welford, and P. Benítez, *Nonimaging optics*, Academic Press, 2005.

[14] T. Bretz, *Status of fact - the first g-apd cherekov telescope*, CTA Consortium Meeting, Rutherford Appleton Laboratory, UK, (2010).

[15] G. Lutz, *Semiconductor Radiation Detectors*, Springer, 1999.

[16] S. M. Sze, *Physics of Semiconductor Devices*, Wiley-Interscience, 2007.

[17] H. Goebel, *Einfuehrung in die Halbleiter-Schaltungselektronik*, Springer, 2008.

[18] D. Renker and E. Lorenz, *Advances in solid state photon detectors*, Journal of Instrumentation, 4 (2009), p. P04004. Available online http://stacks.iop.org/1748-0221/4/i=04/a=P04004, visited 11.27.11.

[19] W. G. Oldham, R. R. Samuelson, and P. Antognetti, *Triggering phenomena in avalanche diodes*, IEEE Transactions on Electron Devices, 19 (1972), pp. 1056–1060. Available online http://ieeexplore.ieee.org/lpdocs/epic03/wrapper.htm?arnumber=1477015, visited 11.27.11.

[20] A. N. Otte, *Observation of VHE Gamma-Rays from the Vicinity of magnetized Neutron Stars and Development of new Photon-Detectors for Future Ground based Gamma-Ray Detectors*, phd thesis, Technische Universitaet Muenchen, Muenchen, 2007.

[21] J. Rennefeld, *Studien zur Eignung von Silizium Photomultipliern fuer den Einsatz im erweiterten CMS Detektor am SLHC*, diploma thesis, III. Phys. Inst. B, RWTH Aachen University, Germany, February 2010.

[22] Hamamatsu, *S10362 series information sheet.* Available online http://sales.hamamatsu.com/de/produkte/solid-state-division/si-photodiode-series/mppc.php, visited 11.27.11.

[23] SensL, *MicroSL product family catalogue.* Available online http://sensl.com/products/silicon-photomultipliers/microsl/microsl-specifications/, visited 11.27.11.

[24] J. Schumacher, *Characterization Studies of Silicon Photomultipliers: Noise and Relative Photon Detection Efficiency*, bachelor thesis, III. Phys. Inst. A, RWTH Aachen University, Feb 2011.

[25] P. Hallen, *Determination of the Recovery Time of Silicon Photomultipliers*, bachelor thesis, III. Phys. Inst. A, RWTH Aachen University, Sep 2011.

[26] Keithley, *Source Meter 2400 data sheet.* Available online http://www.keithley.com/data?asset=9493, visited 11.27.11.

[27] C.A.E.N., *QDC V906 data sheet.*

[28] C.A.E.N, *FADC V1729 data sheet.*

[29] Wiener, *Wiener VM-USB VME controller data sheet.*

[30] D. Terhorst *et al.*, *LibLAB library.* Available online http://liblab.physik.rwth-aachen.de, visited 11.27.11.

[31] T. Hermanns, *Aufbau eines Systems fuer Kuehltests zur Qualitaetsueberwachung von CMS Silizium-Modulen*, diploma thesis, III. Phys. Inst. B, RWTH Aachen University, Germany, January 2004.

[32] F. Beissel, *private communication*, 2011.

[33] Maxim, *DS18B20 data sheet.* Available online http://www.maxim-ic.com/datasheet/index.mvp/id/2812, visited 11.27.11.

[34] R. Brun and F. Rademakers, *Root - an object oriented data analysis framework*, Nuclear Instruments and Methods in Physics Research Section A, 389 (1997), pp. 81–86. Available online http://root.cern.ch/, visited 11.27.11.

[35] C. R. Crowell and S. M. Sze, *Temperature dependence of avalanche multiplication in semiconductors*, Applied Physics Letters, 9 (1966), pp. 242 –244. Available online http://apl.aip.org/resource/1/applab/v9/i6/p242_s1, visited 11.27.11.

[36] M. Petasecca *et al.*, *Thermal and electrical characterization of silicon photomultiplier*, Nuclear Science, IEEE Transactions on, 55 (2008), pp. 1686 – 1690. Available online http://ieeexplore.ieee.org/xpls/abs_all.jsp?arnumber=4545198, visited 11.27.11.

[37] R. Newman, *Visible light from a silicon $p-n$ junction*, Phys. Rev., 100 (1955), pp. 700–703. Available online http://link.aps.org/doi/10.1103/PhysRev.100.700, visited 11.27.11.

[38] A. Lacaita, F. Zappa, S. Bigliardi, and M. Manfredi, *On the bremsstrahlung origin of hot-carrier-induced photons in silicon devices*, Electron Devices, IEEE Transactions on, 40 (1993), pp. 577 –582. Available online http://ieeexplore.ieee.org/stamp/stamp.jsp?tp=&arnumber=199363, visited 11.27.11.

[39] S. Villa, A. L. Lacaita, and A. Pacelli, *Photon emission from hot electrons in silicon*, Phys. Rev. B, 52 (1995), pp. 10993–10999. Available online http://link.aps.org/doi/10.1103/PhysRevB.52.10993.

[40] N. Akil *et al.*, *A multimechanism model for photon generation by silicon junctions in avalanche breakdown*, Electron Devices, IEEE Transactions on, 46 (1999), pp. 1022 –1028. Available online http://ieeexplore.ieee.org/xpls/abs_all.jsp?arnumber=760412, visited 11.27.11.

[41] S. Cova *et al.*, *Evolution and prospects for single-photon avalanche diodes and quenching circuits*, Journal of Modern Optics, 51 (2004), pp. 1267–1288. Available online http://adsabs.harvard.edu/abs/2004JMOp...51.1267C, visited 11.27.11.

[42] P. Eckert *et al.*, *Characterisation studies of silicon photomultipliers*, Nuclear Instruments and Methods in Physics Research Section A: Accelerators, Spectrometers, Detectors and Associated Equipment, 620 (2010), p. 11. Available online http://arxiv.org/abs/1003.6071, visited 11.27.11.

[43] Y. Du and F. Retière, *After-pulsing and cross-talk in multi-pixel photon counters*, Nuclear Instruments and Methods in Physics Research Section A: Accelerators, Spectrometers, Detectors and Associated Equipment, 596 (2008), pp. 396–401.

[44] P. Finocchiaro *et al.*, *Features of silicon photo multipliers: Precision measurements of noise, cross-talk, afterpulsing, detection efficiency*, Nuclear Science, IEEE Transactions on, 56 (2009), pp. 1033 –1041.

[45] Claudio and Piemonte, *A new silicon photomultiplier structure for blue light detection*, Nuclear Instruments and Methods in Physics Research Section A: Accelerators, Spectrometers, Detectors and Associated Equipment, 568 (2006), pp. 224 – 232. Available online http://www.sciencedirect.com/science/article/pii/S016890020601271X, visited 11.27.11.

[46] K. Rajkanan, R. Singh, and J. Shewchun, *Absorption coefficient of silicon for solar cell calculations*, Solid-State Electronics, 22 (1979), pp. 793 – 795.

[47] Keithley, *Keithley Picoammeter 6485 data sheet.* Available online http://www.keithley.com/products/dcac/sensitive/lowcurrent/?mn=6485, visited 11.27.11.

[48] Hamamatsu, *Photodiode Technical Guide.* Available online http://sales.hamamatsu.com/assets/html/ssd/si-photodiode/index.htm, visited 11.27.11.

[49] S. Schmid, Hamamatsu Deutschland, *private communication*, (2011).

Danksagungen - Acknowledgements

An dieser Stelle möchte ich mich bei denen Bedanken, ohne die diese Arbeit nicht oder nur sehr schwer möglich gewesen wäre.

An erster Stelle bedanke ich mich bei Prof. Dr. Thomas Hebbeker für die Gelegenheit an diesem interessanten und abwechslungsreichen Thema arbeiten zu können. Sein sorgsames Feedback war immer hilfreich, um Probleme zu finden und zu lösen, sie aus einem anderen Blickwinkel zu betrachten oder einfach aus einer Sackgasse herauszufinden. Insbesondere danken möchte ich für die Gelegenheit am Auger-Collaboration Meeting teilzunehmen und einen Teil des Experiments mit eigenen Augen sehen und mit eigenen Händen berühren zu können.

Weitergehend gilt Prof. Dr. Martin Erdmann großer Dank dafür, dass er sich bereiterklärt hat der Zweitgutachter für diese Arbeit zu sein.

Ein großer Dank gilt auch Dr. Christine Meurer für die Betreuung während der Arbeit und insbesondere dafür meine Begeisterung für das Thema mit geweckt zu haben.

Außerordentlichen Danke möchte ich meinem Kollegen Maurice Stephan aussprechen. Gerade beim Einstieg in die Messungen war mir sein umfangreiches Wissen in Sachen Hardwarebedienung ausgesprochen hilfreich. Auch hatte er immer für jede Frage ein offenes Ohr und war für jede, stets ertragreiche Diskussion zu haben. Ebenso hat er immer für die nötige Ermutigung gesorgt, wenn es mal nicht so gut lief. Danke Maurice!

Ein goßes Danke auch an meinen Bürokollegen Nils Scharf, für die kompetente Hilfestellung bei Problemen und die interessanten Unterhaltungen, und ebenso an Johannes Schumacher, durch unser Zusammenarbeit am Beginn der Messungen verlief alles viel effizienter und interessanter.

Besonders bedanken möchte ich mich auch bei Dr. Markus Merschmeyer der stets hilfreiche Tipps und Diskussionen parat hatte und sich immer geduldig die Zeit genommen hat diese mit mir zu teilen.

Da die Messungen in dieser Arbeit ohne viele selbst-gefertigte Halterungen, elektronische und mechanische Bauteile nicht möglich gewesen wären gilt mein spezieller Dank allen Mitarbeitern der Elektrischen und Mechanischen Werkstatt und insbesondere Herrn Adamczyk und Herrn Phillips für ihre Entwürfe und hilfreichen Verbesserungsvorschläge sowie Herrn Beißel vom III Phys. Inst. B für das Design und die kontinuierliche Verbesserung des SiPM Verstärkerboards. Ein besonderer

Dank gilt auch allen freiwilligen Mitentwicklern an der Liblab Bibliothek, die das Ansprechen der Laborhardware einem Anfänger erheblich erleichtert hat.

Generell danke möchte ich allen ehemaligen und aktuellen Teilnehmern unserer gemeinsamen Mittwochsmeetings für ihre hilfreichen Einwürfe und Ansatzvorschlägen und generell der gesamten Aachener Auger Gruppe für die angenehme Arbeitsatmosphäre.

Ein großes Danke möchte ich auch meinen Korrekturlesern, Markus Merschmeyer, Christine Meurer, Matthias Plum und Maurice Stephan aussprechen für ihre zahlreichen Verbesserungsvorschläge und Geduld beim Lesen. Danke auch an Stephan Fliescher und Anna Nelles für die Latex-Vorlage mit der diese Arbeit geschrieben wurde.

Zu guter Letzt möchte ich mich bei allen meinen Freunden und Verwandten bedanken, die mir in dieser Zeit den benötigten seelischen Beistand geleistet haben. Dies gilt insbesondere für meine Eltern und meine Freunde aus der Gruppe Marcel und Lukas, danke euch allen und allen die ich hier vielleicht vergessen habe.

A. Appendix

A.1 List of Abbreviations

ADC	Analog to digital converter
APD	Avalanche photodiode
CFD	Constant fraction discriminator
FADC	Flash analog to digital converter
FD	Fluorescence detector (of the Pierre Auger Observatory)
FWHM	Full width at half maximum
GAPD	Geiger-mode avalanche photodiode
PDE	Photon detection efficiency
PMT	Photomultiplier tube
QDC	Charge to digital converter
SD	Surface detector (of the Pierre Auger Observatory)
SiPM	Silicon photomultiplier
UHECRs	Ultra-high-energy cosmic rays

B. Appendix

B.1 Additional Tables

Tabelle B.1: After-pulse analysis fit parameters from section 7.2.3.2.

SiPM Type	Over-Voltage	χ^2/NDOF	C_{TH}	R_{TH} / kHz	C_S	τ_S / ns	C_F	τ_F / ns
1x1 mm^2, 100 µm	0.80 ± 0.01	0.95	6.16 ± 0.05	494 ± 50	6.65 ± 0.63	129.4 ± 16.5	7.61 ± 0.20	43.7 ± 17.1
1x1 mm^2, 100 µm	0.90 ± 0.01	1.10	6.07 ± 0.05	508 ± 45	6.46 ± 0.22	162.0 ± 43.8	7.76 ± 0.10	48.4 ± 6.1
1x1 mm^2, 100 µm	1.00 ± 0.01	0.99	6.26 ± 0.04	648 ± 45	7.18 ± 0.52	112.8 ± 11.4	7.92 ± 0.16	40.3 ± 14.9
1x1 mm^2, 100 µm	1.10 ± 0.01	1.04	6.55 ± 0.02	655 ± 19	7.52 ± 0.05	127.9 ± 17.3	8.49 ± 0.09	42.1 ± 3.0
1x1 mm^2, 100 µm	1.20 ± 0.01	1.08	6.47 ± 0.02	775 ± 21	7.49 ± 0.07	119.2 ± 13.1	8.46 ± 0.07	45.0 ± 3.0
1x1 mm^2, 100 µm	1.30 ± 0.01	1.08	6.44 ± 0.02	799 ± 22	7.60 ± 0.05	125.9 ± 12.3	8.73 ± 0.07	40.8 ± 2.2
1x1 mm^2, 100 µm	1.40 ± 0.01	1.13	6.73 ± 0.02	856 ± 19	7.97 ± 0.05	121.3 ± 8.8	9.09 ± 0.05	43.7 ± 1.8
1x1 mm^2, 100 µm	1.50 ± 0.01	1.20	6.64 ± 0.02	924 ± 21	7.90 ± 0.05	123.1 ± 10.6	9.13 ± 0.04	44.5 ± 1.7
1x1 mm^2, 100 µm	1.60 ± 0.01	1.04	6.65 ± 0.02	1057 ± 20	8.11 ± 0.04	111.7 ± 8.0	9.26 ± 0.04	40.6 ± 1.5
1x1 mm^2, 100 µm	1.70 ± 0.01	1.07	6.00 ± 0.03	995 ± 31	7.37 ± 0.05	129.6 ± 13.1	8.82 ± 0.04	44.7 ± 1.6
1x1 mm^2, 100 µm	1.80 ± 0.01	0.94	6.14 ± 0.02	1103 ± 26	7.89 ± 0.03	110.1 ± 11.3	9.18 ± 0.05	36.0 ± 1.4
3x3 mm^2, 100 µm	0.91 ± 0.02	0.94	7.34 ± 0.01	1347 ± 16	7.11 ± 0.09	150.2 ± 22.9	8.08 ± 0.09	50.0 ± 4.2
3x3 mm^2, 100 µm	1.01 ± 0.02	0.89	7.24 ± 0.01	1513 ± 14	7.45 ± 0.05	124.0 ± 15.4	8.10 ± 0.17	39.3 ± 4.4
3x3 mm^2, 100 µm	1.11 ± 0.02	0.99	7.44 ± 0.01	1730 ± 14	7.67 ± 0.07	117.6 ± 17.3	8.40 ± 0.10	44.1 ± 3.8
3x3 mm^2, 100 µm	1.21 ± 0.02	1.02	7.18 ± 0.02	1830 ± 20	7.36 ± 0.08	133.4 ± 15.9	8.28 ± 0.06	50.1 ± 3.4
3x3 mm^2, 100 µm	1.31 ± 0.02	0.96	7.25 ± 0.02	1978 ± 19	7.75 ± 0.06	123.2 ± 14.0	8.56 ± 0.06	45.4 ± 2.6
3x3 mm^2, 100 µm	1.41 ± 0.02	1.08	7.27 ± 0.01	2194 ± 18	8.00 ± 0.05	106.7 ± 9.8	8.59 ± 0.07	42.6 ± 2.8

SiPM Type	Over-Voltage	χ^2/NDOF	C_{TH}	R_{TH} / kHz	C_S	τ_S / ns	C_F	τ_F / ns
1x1 mm^2, 50 µm	1.13 ± 0.02	1.05	5.03 ± 0.01	454 ± 15	5.53 ± 0.15	76.2 ± 7.0	7.45 ± 0.27	15.5 ± 2.2
1x1 mm^2, 50 µm	1.33 ± 0.02	0.88	5.31 ± 0.02	503 ± 21	5.58 ± 0.27	98.8 ± 17.7	7.46 ± 0.15	22.1 ± 3.2
1x1 mm^2, 50 µm	1.53 ± 0.02	0.99	5.20 ± 0.02	601 ± 24	5.42 ± 0.19	112.3 ± 15.9	7.54 ± 0.09	23.7 ± 2.0
1x1 mm^2, 50 µm	1.73 ± 0.02	0.93	5.05 ± 0.02	698 ± 24	5.61 ± 0.24	94.7 ± 14.3	7.56 ± 0.10	22.4 ± 2.4
1x1 mm^2, 50 µm	1.93 ± 0.02	1.05	4.60 ± 0.02	802 ± 24	5.61 ± 0.18	77.8 ± 7.8	7.44 ± 0.15	18.5 ± 2.1
1x1 mm^2, 50 µm	2.13 ± 0.02	0.99	4.90 ± 0.02	789 ± 25	5.84 ± 0.13	97.9 ± 8.3	7.74 ± 0.08	21.8 ± 1.6
1x1 mm^2, 50 µm	2.33 ± 0.02	1.03	5.17 ± 0.02	928 ± 22	6.31 ± 0.11	86.8 ± 6.0	8.26 ± 0.08	19.6 ± 1.3
1x1 mm^2, 50 µm	2.53 ± 0.02	1.12	5.37 ± 0.02	995 ± 21	6.55 ± 0.10	88.6 ± 5.5	8.59 ± 0.07	19.9 ± 1.1
1x1 mm^2, 50 µm	2.73 ± 0.02	0.99	5.36 ± 0.02	1053 ± 24	6.61 ± 0.10	94.5 ± 6.0	8.67 ± 0.06	21.4 ± 1.1
1x1 mm^2, 50 µm	2.83 ± 0.02	1.00	5.63 ± 0.02	1110 ± 19	7.09 ± 0.08	83.8 ± 3.9	9.16 ± 0.06	18.8 ± 0.8
3x3 mm^2, 50 µm	1.08 ± 0.03	1.03	6.33 ± 0.01	990 ± 14	5.86 ± 0.35	91.1 ± 20.1	7.97 ± 1.09	17.3 ± 8.2
3x3 mm^2, 50 µm	1.18 ± 0.03	1.07	6.89 ± 0.01	1097 ± 11	6.36 ± 0.24	99.9 ± 14.9	7.94 ± 0.23	24.4 ± 4.4
3x3 mm^2, 50 µm	1.38 ± 0.03	0.97	6.57 ± 0.01	1315 ± 12	6.34 ± 0.19	88.2 ± 10.2	8.14 ± 0.27	19.7 ± 3.2
3x3 mm^2, 50 µm	1.48 ± 0.03	1.07	7.12 ± 0.01	1399 ± 10	7.06 ± 0.14	87.1 ± 7.4	8.68 ± 0.18	20.5 ± 2.5
3x3 mm^2, 50 µm	1.68 ± 0.03	1.02	6.72 ± 0.01	1602 ± 14	6.78 ± 0.13	88.1 ± 7.4	8.52 ± 0.17	19.5 ± 2.2
3x3 mm^2, 50 µm	1.78 ± 0.03	1.01	7.23 ± 0.01	1704 ± 14	7.20 ± 0.14	94.6 ± 9.0	9.05 ± 0.10	21.8 ± 1.9
3x3 mm^2, 50 µm	1.98 ± 0.03	0.93	6.69 ± 0.03	1864 ± 25	6.65 ± 0.10	118.1 ± 11.5	8.51 ± 0.06	25.2 ± 1.6
3x3 mm^2, 50 µm	2.08 ± 0.03	1.03	7.52 ± 0.01	2000 ± 17	7.71 ± 0.09	93.8 ± 6.0	9.41 ± 0.06	23.7 ± 1.3
3x3 mm^2, 50 µm	2.18 ± 0.03	1.11	7.23 ± 0.01	2083 ± 15	7.51 ± 0.08	95.8 ± 5.3	9.32 ± 0.05	22.9 ± 1.1
3x3 mm^2, 50 µm	2.28 ± 0.03	0.98	6.63 ± 0.02	2177 ± 26	6.79 ± 0.15	101.7 ± 10.7	8.56 ± 0.05	26.8 ± 1.8
3x3 mm^2, 50 µm	2.38 ± 0.03	0.94	7.08 ± 0.01	2267 ± 17	7.65 ± 0.06	90.9 ± 3.9	9.46 ± 0.06	20.4 ± 0.9
3x3 mm^2, 50 µm	2.48 ± 0.03	1.02	7.06 ± 0.02	2366 ± 22	7.51 ± 0.08	99.4 ± 5.6	9.37 ± 0.04	23.6 ± 1.0
3x3 mm^2, 50 µm	2.58 ± 0.03	0.99	6.50 ± 0.02	2521 ± 27	7.20 ± 0.10	84.8 ± 5.4	9.00 ± 0.09	19.7 ± 1.4

B.2 Additional Plots

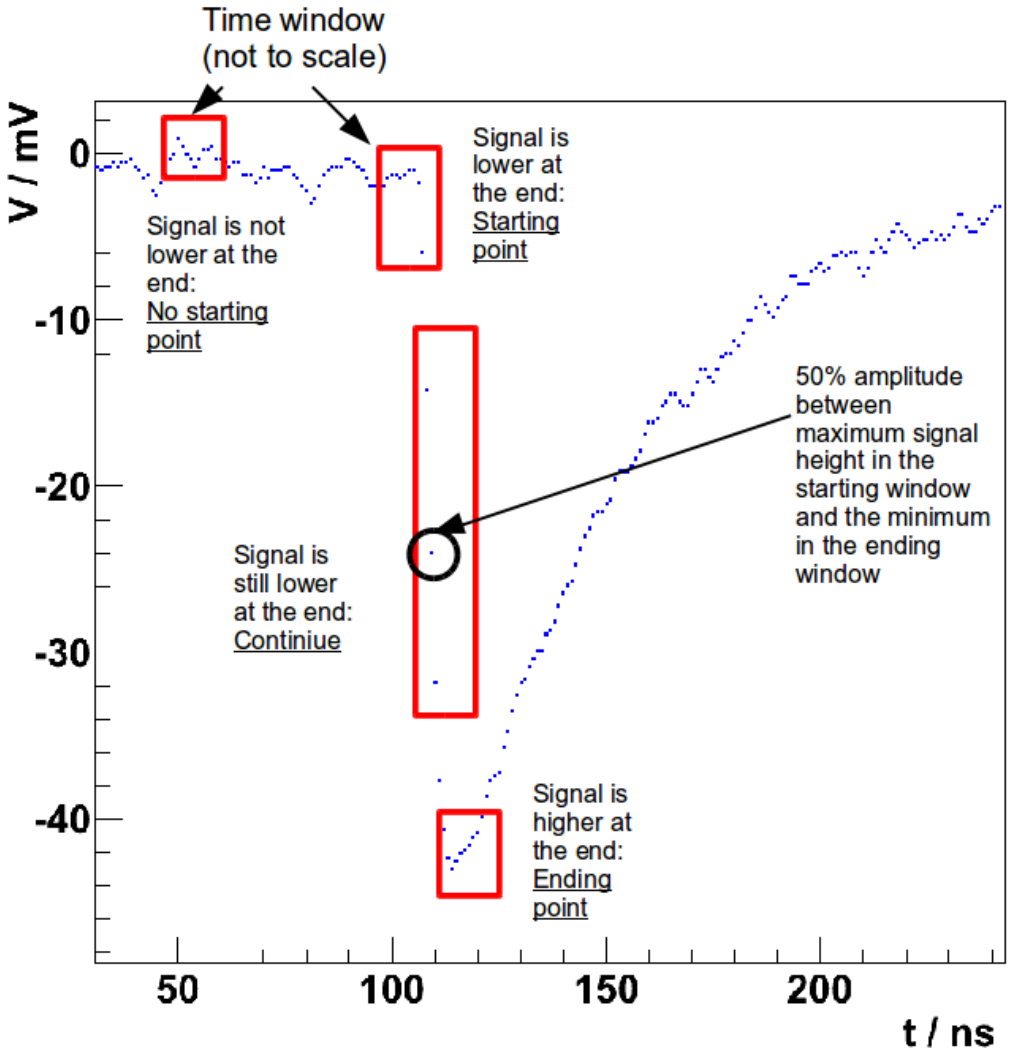

Abbildung B.1: Schematic of FADC trace analysis. Not shown is that this method can also trigger on noise. This is discarded by a threshold later on in the analysis. A description of the algorithm can be found on page 53.

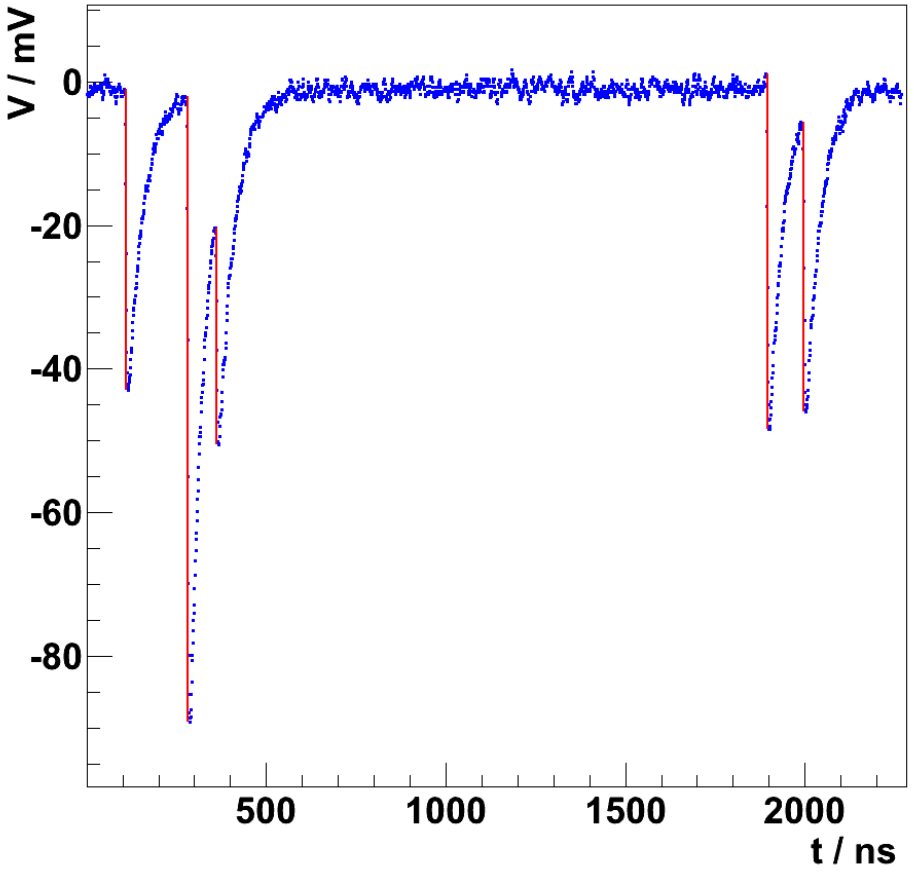

Abbildung B.2: Measured FADC trace with multiple SiPM events. Red (vertical) lines represent the reconstructed peak amplitude and where the identified peak has reached 50% of its height.
($1\text{x}1\,\text{mm}^2, 100$ µm cell pitch, T = (28.2 ± 0.1(stat.) ± 0.5(sys.))° C,
V_{OV}= (1.30 ± 0.02) V)

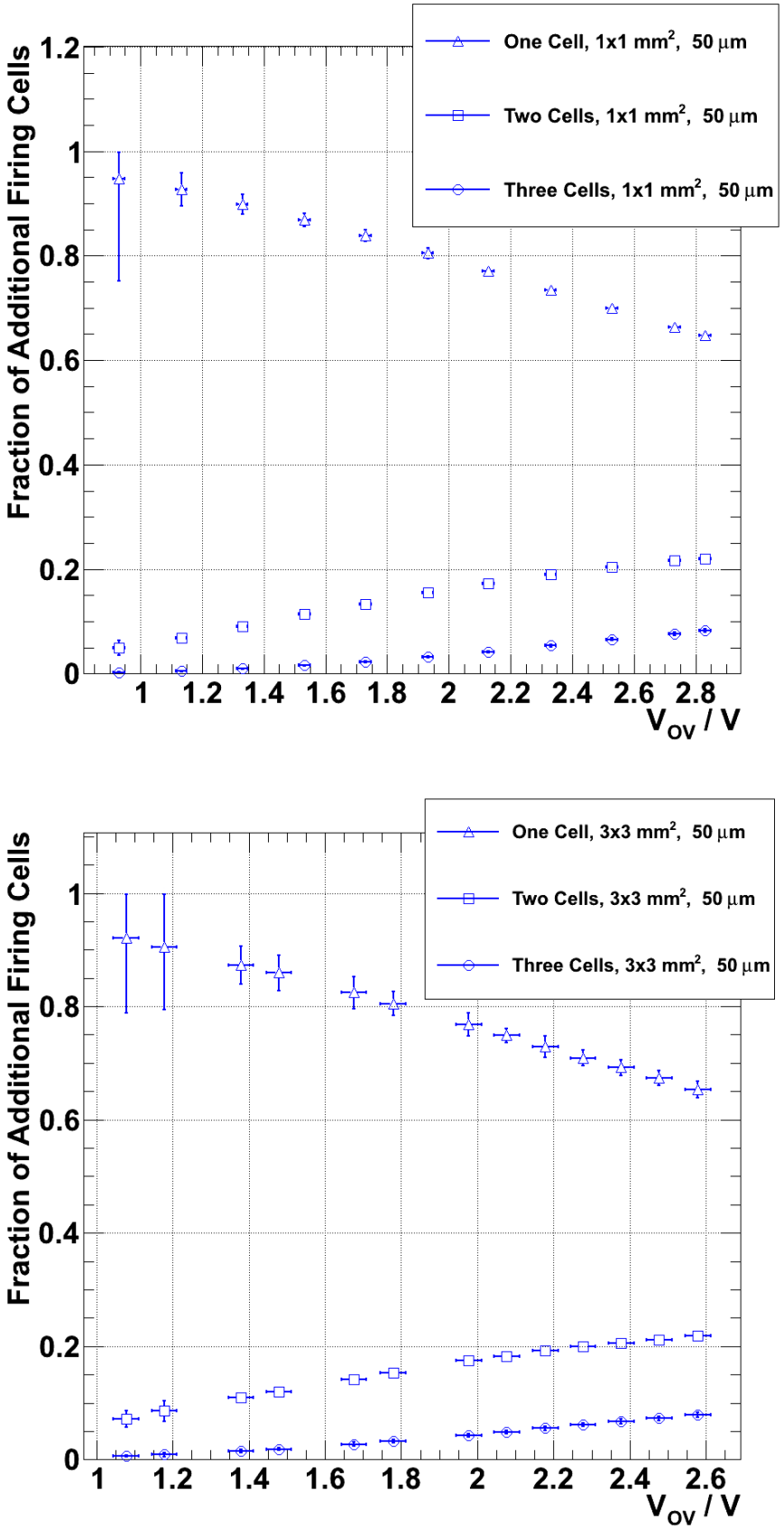

Abbildung B.3: Fraction of crosstalk events where exactly one, two or three additional cells are fired due to optical crosstalk as a function of the over-voltage. ($1\text{x}1\,\text{mm}^2$ and $3\text{x}3\,\text{mm}^2, 50$ µm cell pitch SiPMs)

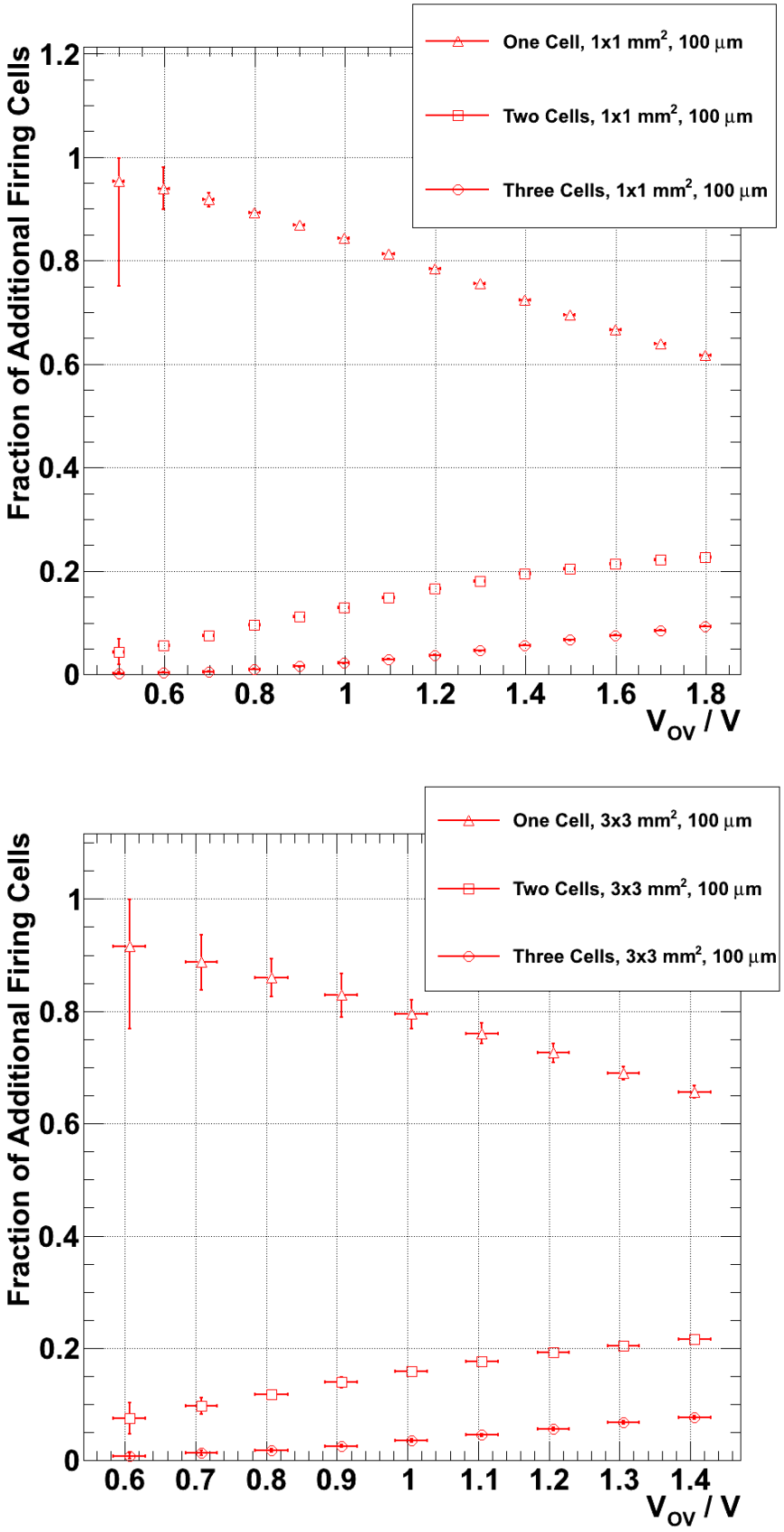

Abbildung B.4: Fraction of crosstalk events where exactly one, two or three additional cells are fired due to optical crosstalk as a function of the over-voltage. ($1\text{x}1\,\text{mm}^2$ and $3\text{x}3\,\text{mm}^2$, 100 µm cell pitch SiPMs)

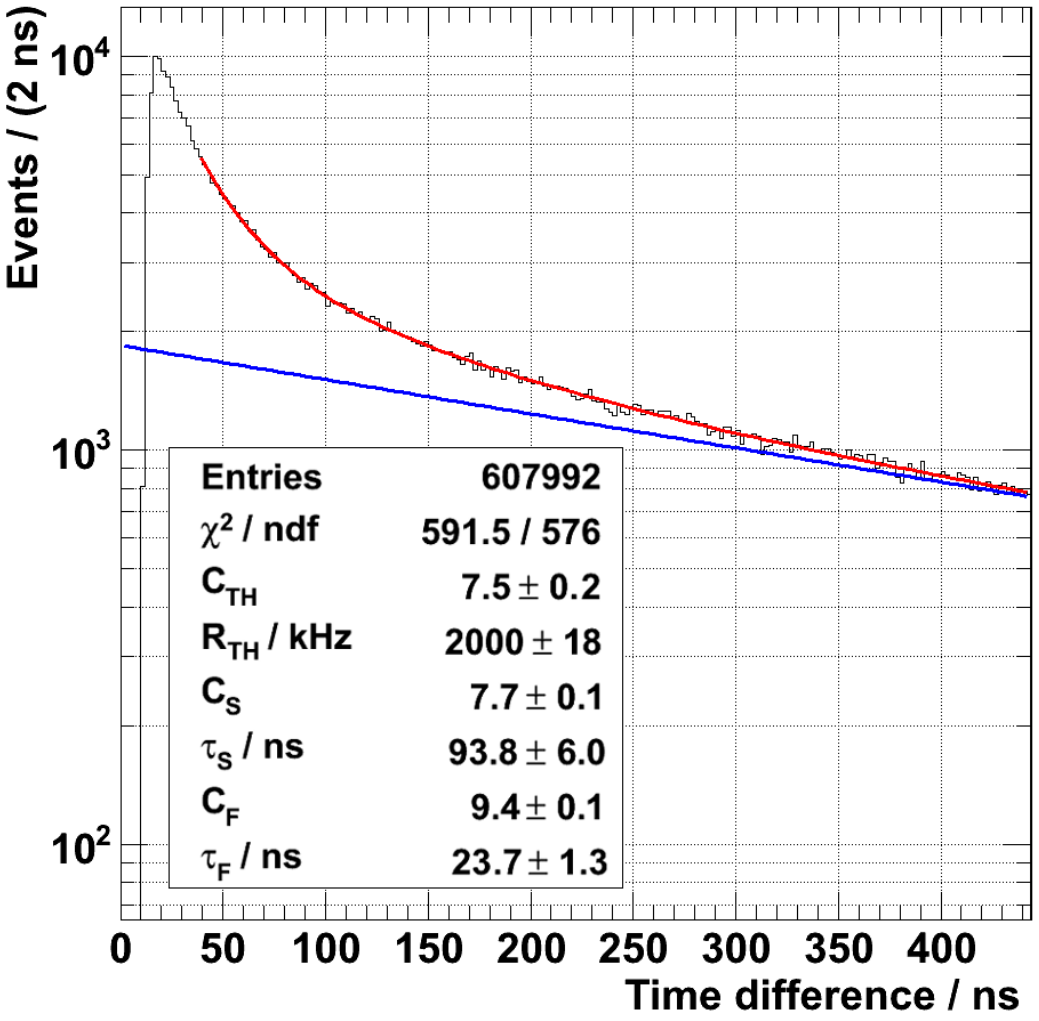

Abbildung B.5: Distribution of the time difference between an initial 1 p.e. start pulse and the next pulse. The blue (straight) line represents the contribution of thermal noise pulses, the red (curved) line is a fit of three exponential functions to the data (see equation (7.4)). This is a zoom in the 0-400 ns region. The complete distribution is shown on page 62.
(3x3 mm^2, 50 µm cell pitch, V_{OV}= (2.10 ± 0.04) V)

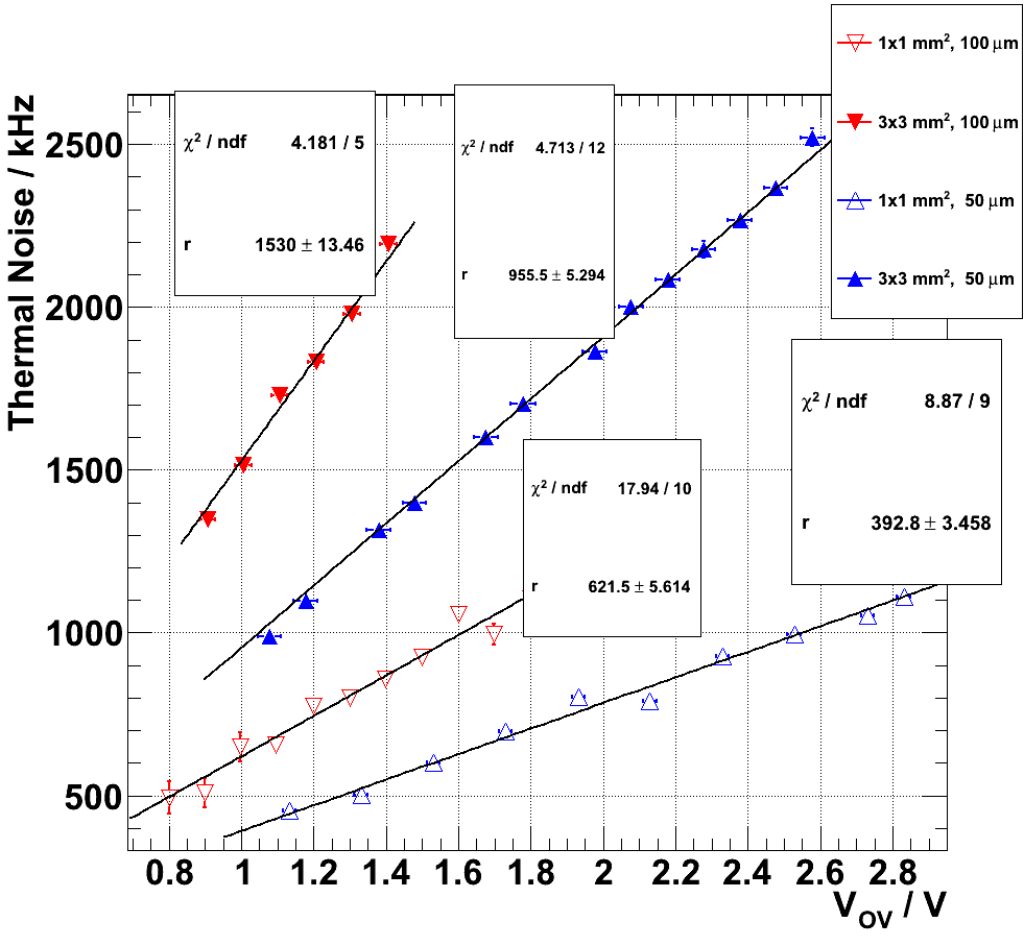

Abbildung B.6: Thermal noise rate as a function of the over-voltage for different SiPM types, fitted with function (7.5).
(Different Temperatures for different types:
T(3x3 mm^2)=(1.0 ± 0.5) °C,T(1x1 mm^2)=(25.5 ± 0.5) °C)

.

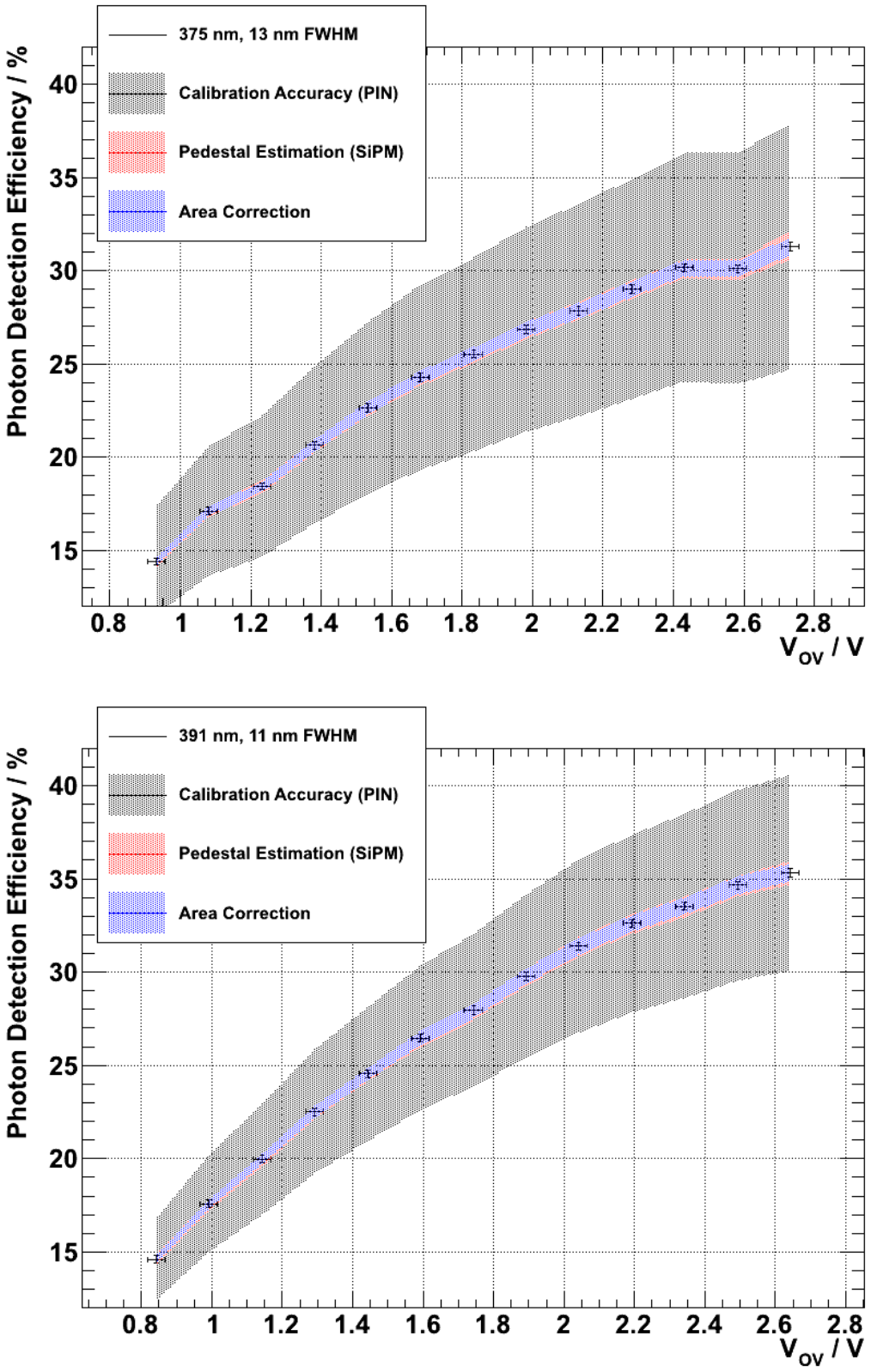

Abbildung B.7: Photon detection efficiency at LED peak emission wavelengths of 375 and 391 nm of the 1x1 mm^2, 50 µm cell pitch type. Bands specify systematic uncertainty due to: The calibration accuracy of the PIN diode and the change of the Q.E. over the LED spectral width (black, outer band), the accuracy with which the pedestal events in the QDC SiPM charge spectra can be identified (red, middle bands), measured correction factor for the different active areas of PIN diode and SiPM (blue, inner band).

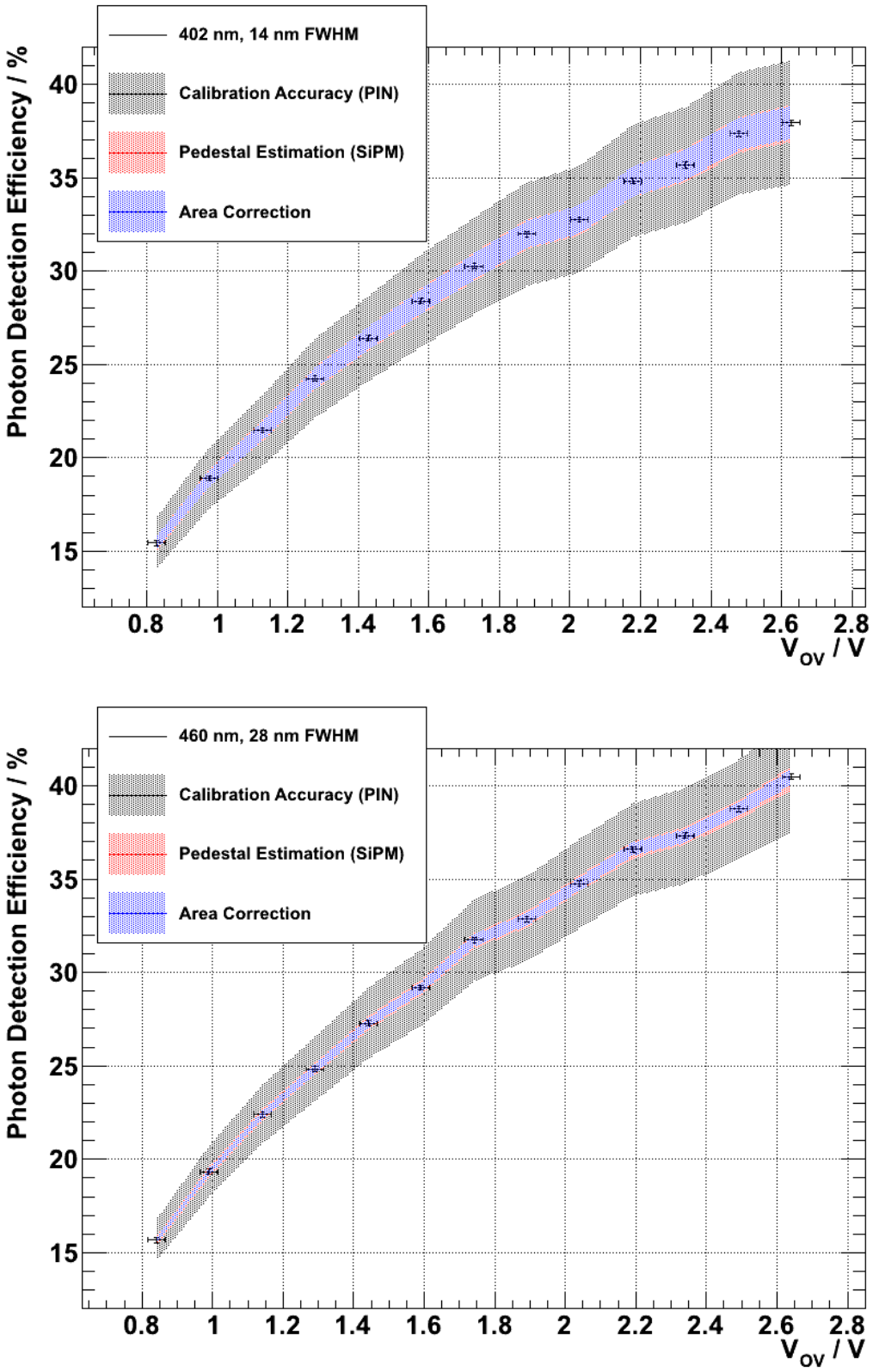

Abbildung B.8: Photon detection efficiency at LED peak wavelengths of 402 and 460 nm of the 1x1 mm^2, 50 µm cell pitch type.

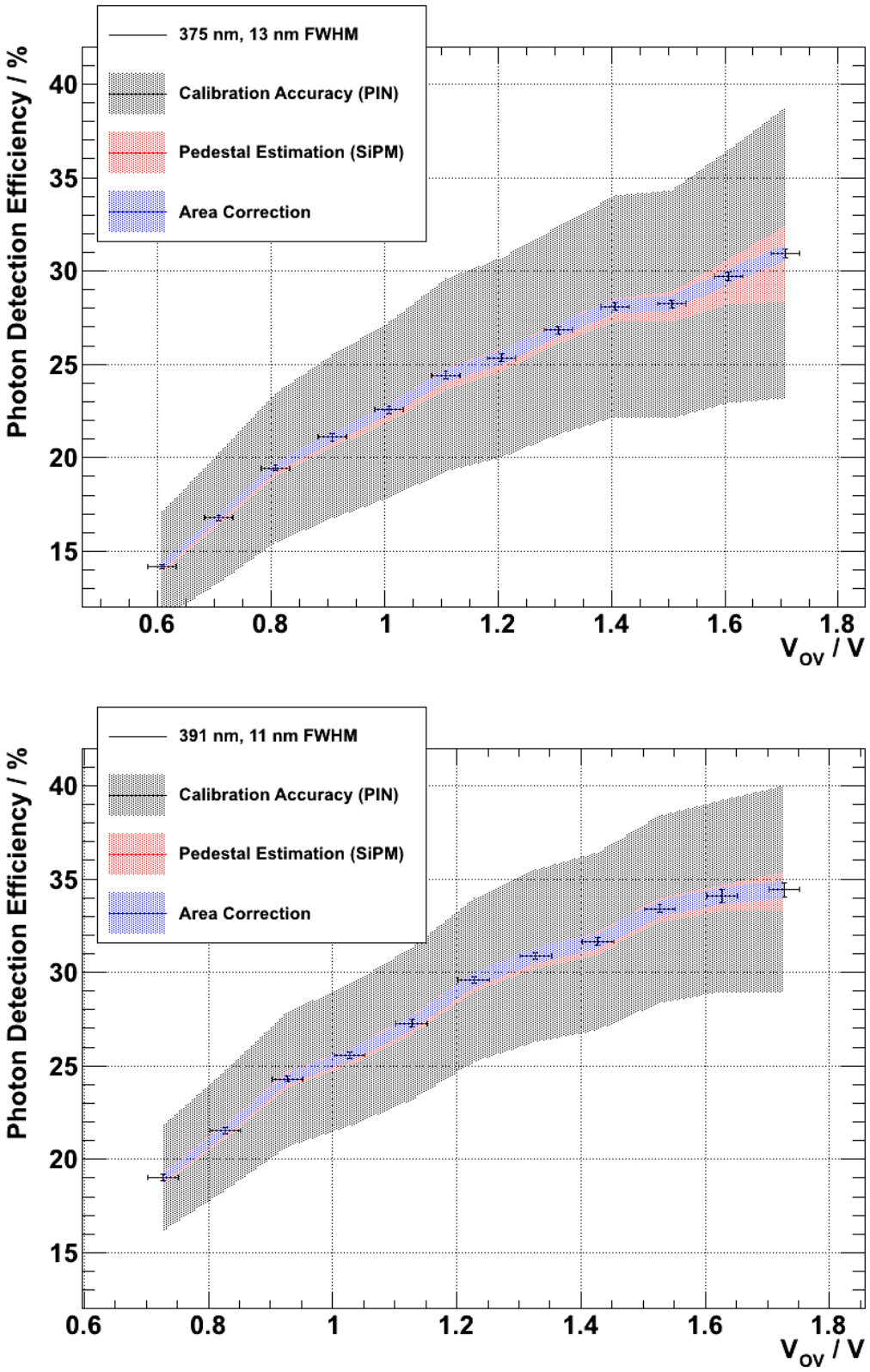

Abbildung B.9: Photon detection efficiency at LED peak wavelengths of 375 and 391 nm of the 1x1 mm^2, 100 µm cell pitch type.

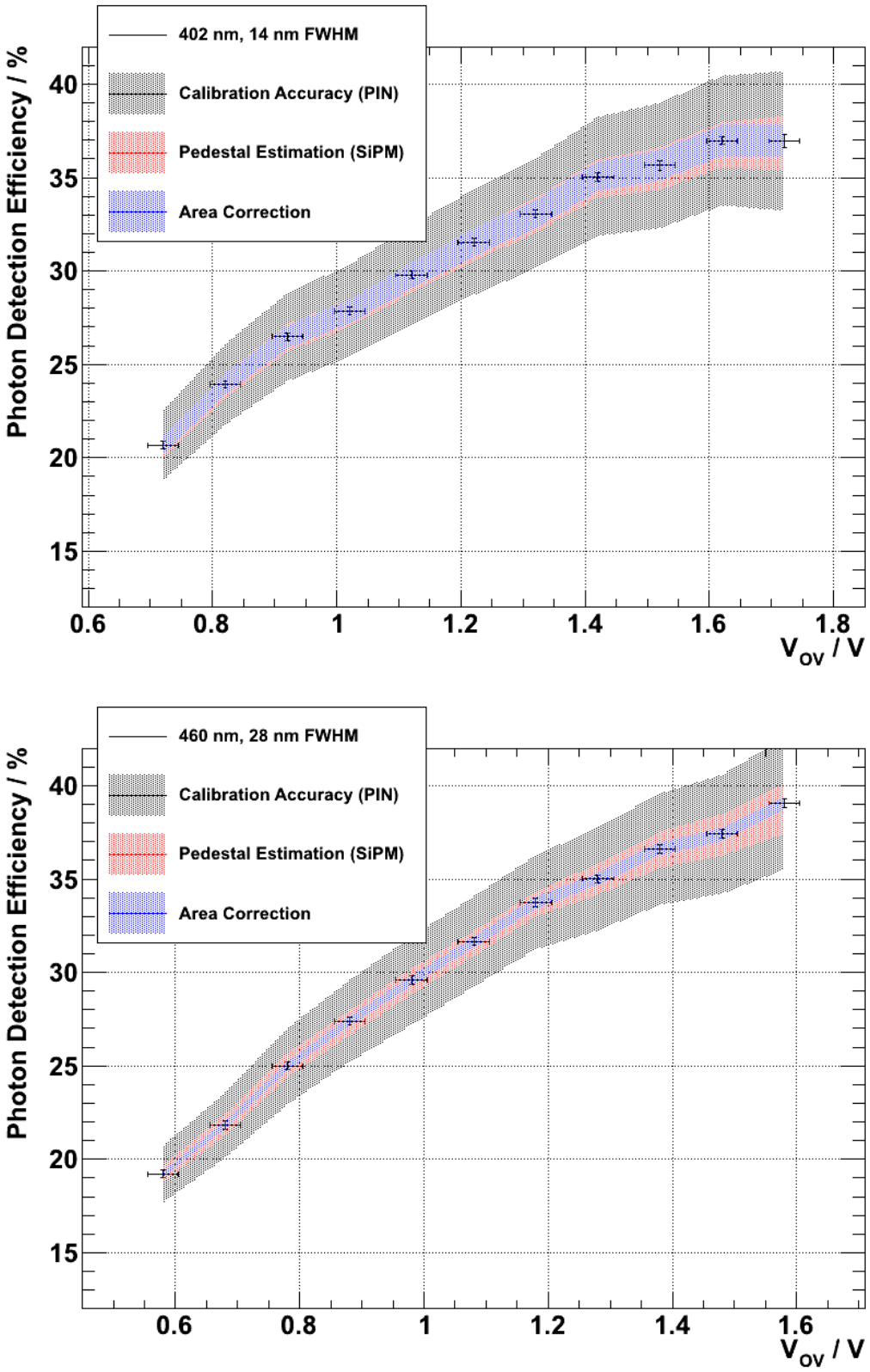

Abbildung B.10: Photon detection efficiency at LED peak wavelengths of 402 and 460 nm of the 1x1 mm^2, 100 µm cell pitch type.

Erklärung

Hiermit versichere ich, dass ich diese Arbeit einschließlich beigefügter Zeichnungen, Darstellungen und Tabellen selbstständig angefertigt und keine anderen als die angegebenen Hilfsmittel und Quellen verwendet habe. Alle Stellen, die dem Wortlaut oder dem Sinn nach anderen Werken entnommen sind, habe ich in jedem einzelnen Fall unter genauer Angabe der Quelle deutlich als Entlehnung kenntlich gemacht.

Aachen, den 3. April 2012

Markus Lauscher